Freya Sofia Andersen

Freeze casting of piezoelectric BCZT for biomedical applications

Master's thesis in Chemical Engineering and Biotechnology
Supervisor: Julia Glaum
December 2019

Master's thesis

NTNU
Norwegian University of
Science and Technology

Freya Sofia Andersen

Freeze casting of piezoelectric BCZT for biomedical applications

Master's thesis in Chemical Engineering and Biotechnology
Supervisor: Julia Glaum
December 2019

Norwegian University of Science and Technology
Faculty of Natural Sciences
Department of Materials Science and Engineering

NTNU
Norwegian University of
Science and Technology

Preface

This thesis is submitted to the Norwegian University of Science and Technology in the course TMT4900 Materials Chemistry and Energy Technology, Master's Thesis, as a finalization of the Master's degree program Chemical Engineering and Biotechnology. The work has been supervised by associate professor Julia Glaum and researcher Magnus Rotan.

The viscosity measurements were conducted by Senior Engineer Jens Norrman and PhD candidate Anuvansh Sharma performed the zeta potential measurements, both at the Department of Chemical Engineering at NTNU. All other work presented in this study was carried out by the author, at the Department of Materials Science and Engineering, NTNU.

<div align="center">
Trondheim, 2019-12-16
Freya Sofia Andersen
</div>

Acknowledgments

I would like to take the time to give recognition to the people who have guided and supported me throughout my work. Firstly, special thanks goes to my main supervisor Julia Glaum. Not only have you set aside time for our weekly meetings, but your door has also always been open. I am grateful for the patience you have shown, as my questions are not always well formulated, especially in the times when I have been most confused. Your comprehensive knowledge in the field has been invaluable. Secondly, I would like to thank my co-supervisor Magnus Rotan. Your guidance in the experimental work has been very helpful. Thank you for taking the time to give me advice, whenever I have sent you messages, e-mails or come knocking on the door to your office.

Thanks also goes to the other professors, post docs and PhDs in the Functional Materials and Materials Chemistry Research group for your knowledge and helpful feedback. I am particularly grateful to the PhD candidates who have assured me that I am not the only one who struggles with my work. I would like to express thanks to the technical staff and engineers at the Department of Material Science and Engineering for training and assistance with the experimental equipment. Thank you to Jens Norrman for conducting the viscosity analysis and Anuvansh Sharma for performing the zeta potential measurements. Thanks also goes to Anuvansh Sharma for his input on stabilization of suspensions.

Finally, I would like to thank my partner for his immense support. Thank you for listening to me talk endlessly about freeze casting for the past whole year.

iv

Abstract

The use of piezoelectric ceramics as bone replacement materials presents an opportunity to promote healing of damaged bone by electrical stimulation to bone cells *in vivo*. In this way, patient recuperation could be improved and the likelihood of revision surgeries reduced. In recent years, freeze casting has emerged as a potential processing method for the preparation of such implant materials, as it can produce porous network structures that resemble the structure of bone.

In this study, porous ferroelectric calcium and zirconium doped barium titanate (BCZT) samples were processed by the freeze casting method. A freeze casting slurry consisting of primarily BCZT powder and water was unidirectionally frozen by cooling with liquid nitrogen. Rejection of the powder particles by the solidification front resulted in segregation of the ceramic and the ice in the frozen structure. The solidified ice crystals were removed by sublimation, leaving behind aligned, interconnected and lamellar pores, which remained in the structure after sintering.

The addition of a binder to the slurry was necessary to achieve a stable green body after sublimation of the ice. A dispersant was also required to ensure that sedimentation of the powder particles did not occur during slurry preparation and freezing. The freeze casting process produced porous structures with up to 45% porosity, and a maximum pore width of 50 μm. The particle size of the BCZT powder exhibited a large influence on the formation of the lamellar structure. From this study, it appears that a particle size of 100 nm is required to avoid encapsulation of the particles by the ice during freezing.

The piezoelectric coefficient of the lamellar porous samples reached up to 77% of the dense reference value, demonstrating that the freeze cast structures could be successfully poled.

The work conducted in this thesis demonstrates the feasability of freeze casting as a method to producing porous BCZT for biomedical applications.

Sammendrag

Bruken av piezoelektriske keramer som beinimplantat gir muligheten til å forsterke heling av skadet bein gjennom elektrisk stimulering *in vivo*. På denne måten kan rekonvalesenstiden og sannsynligheten for revisjonsutskiftninger senkes. I de siste årene har frysestøping kommet frem som en mulig prosseseringsmetode til dannelsen av slike implantater, da det kan produsere porøse nettverksstrukturer som er lik strukturen til bein.

I denne masteroppgaven har porøst ferroelectrisk kalsium og zirkonium dopet barium titanat (BCZT) blitt fremstilt ved frysestøping. En slikker til frysestøping, bestående primært av BCZT pulver og vann, ble fryst ved å kjøle ned med flytende nitrogen. Avstøting av pulverpartiklene fra isen førte til segregering av keramen og isen i den fryste strukturen. De faste iskrystallene ble fjernet ved sublimasjon, slik at det gjensto en struktur med rettede, koblede og lamellære porer, som gjensto i strukturen etter sintring.

Tillegg av et bindemiddel i slikkeren var nødvendig for å oppnå en mekanisk stabil grønnkropp etter sublimering av isen. Det var også behov for å tilsette et dispergeringsmiddel, for å sikre at pulverpartiklene ikke sedimenterte i løpet av fryseprosessen. Frysetøping produserte porøse strukturer med en porøsitet på opp til 45%, og en maksimum porebredde på 50 μm. Partikkelstørrelsen på BCZT pulveret påvirket i stor grad dannelsen av den lamellære strukturen. I følget dette arbeidet kreves en partikkelstørrelse på 100 nm for å unngå at partiklene blir fanget av isen.

Den piezoelektriske koeffisienten til de porøse prøvene nådde opptil 77% av verdien til den tette referanseverdien, noe som viser at den frysestøpede strukturen kunne poles.

Arbeidet gjennomført i denne masteroppgaven viser at frysestøping kan være en mulig metode til å produsere BCZT til biomedisinske applikasjoner.

viii

Contents

Chapter 1

Background

1.1 Motivation

Bone replacement with artificially synthesized materials is a routine procedure in modern-day medical practice. Although bone naturally has the ability to regenerate itself, engineered bone repair may be necessary in cases of for example complicated fractures, hip- and knee replacements and rebuilding of bone after tumor surgery [1]. The function of the implanted material is not only to replace the diseased- or damaged tissue, but also to act as a scaffold for the reconstruction and healing of the bone, alleviating pain and restoring function to the part. Deterioration of bone tissue and the probability of fracture increases with age, as a result of a loss of bone density and thereby bone strength. Due to increased life expectancy, which now lies in the range of 80+ years, the elderly population is growing, and people can in a sense outlive their own tissue [2]. The need for bone replacement materials is therefore continuously increasing and there also becomes a higher demand for the longevity of the implants.

Existing implant designs predominantly rely on metals such as titanium alloys and stainless steel or ceramics like alumina and zirconia, materials, which function positively in many respects. Metallic biomaterials have and continue to be used extensively due to their relatively high strength and fracture toughness, properties which make them a reliable choice for load bearing applications. Bioceramics, on the other hand, generally exhibit better biocompatib- ility [3]. One common limitation among these biomaterials, however, is the formation of a non-adherent fibrous capsule at the bone-implant interface, which ultimately leads to loosening and clinical failure of the implant. This occurs as part of the tissue's natural immune repose to foreign materials, and is a result of poor bonding and relative motion between the bone tissue and implant [1,4,5]. Aseptic loosening is the most frequent cause of revision surgeries, interventions that both increase stress and danger to the patient, and are also time-consuming and expensive to preform [4]. Current research consequently focuses on developing materials that form a more stable fixation to bone tissue, which in

turn makes the implant better suited to withstand the variable, multiaxial mechanical loads present *in vivo*. In addition, modern-day biomaterials aim to enhance the body's natural repair cycles, by mimicking or stimulating processes that are key to bone formation, and thereby promote faster healing and improved patient recuperation.

The idea of using piezoelectric ceramics as bone replacement materials was sparked by the discovery that bone itself is electrically active [6]. Upon mechanical loading, electrical potentials arise from the piezoelectricity of collagen and the pressure induced flow of charged fluids in the bone matrix. Such stress induced potentials regulate the activity of the osteoblas- ts, or bone-growing cells, and determine the correlation between mechanical loading and bone adaptation. This has lead to several promising studies, where such effects have attempted to be emulated by external electrical stimulation, showing a positive impact on cell growth and differentiation. A piezoelectric material has, by virtue of its intrinsic functional properties, the ability to generate electricity when mechanically deformed. Increased electri- cal stimulation could thereby be generated *in vivo*, upon loading of the piezoelectric implant, promoting faster tissue growth.

Barium titanate (BT)-based piezoelectrics are some of the most researched alternatives for active bone replacement materials. BT is a ferroelectric ceramic displaying a piezoelectric coefficient of approximately 190 pC/N [7]. As this is much higher than the piezoelectricity of bone, which is about 0.7 pC/N [8], BT demonstrates the potential to offer increased electrical stimulation to bone cells *in vivo* through the piezoelectric effect. Indeed, a study conducted by *Feng et al.* showed that the addition of BT in hydroxyapatite (HA) samples implanted in the femora of dogs, promoted bone growth and repair more than pure HA [9]. Of increasing interest is the BT ceramic doped with Ca^{2+} and Zr^{4+}, commonly referred to as BCZT, as it has been shown to display exceptionally high piezoelectric coefficients of up to 620 pC/N [10]. A recent study conducted by *Poon et al.* demonstrated that BCZT gave enhanced cell viability and proliferation compared to a polystyrene control group, when tested *in vitro* with human osteoblast and endothelial cells [11]. In addition, the BCZT samples displayed low cytotoxicity, advocating for the biocompatibilty of the ceramic, which describes the ability of the material to function as intended and without toxic or injurous effects [12]. Increased cell proliferation with BCZT is also supported in other works, such as the study from *Scarisoreanu et al.* on BCZT thin films [13]. *Pisitpipathsin et al* also reported that the inclusion of BCZT in bioglass increased the formation of bone-like apatite on the surface of the composite, when soaked in simulated body fluid [14]. The high piezoelectric response and biocompatibility of BCZT reveals its potential to function as a cell stimulating implant.

Alongside material selection, implant design parameters are critical in determining the success of a bone grafting. The introduction of large and interconnected pores into the biomaterial allows ingrowth of bone tissue, termed biological fixation, and forges a more stable bone-impl- ant interface for loading. Pores larger than 100-150 μm are required for vascularization of and thereby viable tissue [1]. However, micro- and nano sized surface

features can also aid in creating a more stable fixation [15]. Although a high porosity is beneficial to the integration of the implant, the presence of pores also degrades both the mechanical and piezoelectric properties of the material. The optimal level of porosity is therefore a trade-off between multiple parameters. There are several existing approaches to preparing macroporous (pore size > 50 nm) ceramics, the three primary methods being the replica-, sacrificial template- and direct foaming techniques, where pores are formed through the replication of a cellular structure, the incorporation of air into a suspension and the inclusion of a sacrificial phase that is burnt out, respectively [16]. All of the named methods have merits and drawbacks, some of the shortcomings being a low strength of the porous structure and the lack of an ability to control the pore size, interconnectivity and arrangement [17]. The novel freeze casting, or ice templating, method has the potential to relieve some of these issues, and has in recent years received a great deal of attention in the field of biomaterials [8, 18, 19], due to its versatility and the formation of highly directional porosity. Freeze casting consists of freezing a colloidal suspension of ceramic powder, sublimating the frozen solvent and finally densifying the ceramic matrix through sintering. The resulting porous structure is thus a replica of the solidified phase and can be made aligned with unidirectional freezing. Water is one of the most commonly used freezing liquids. Due to the anisotropic growth of ice, the resulting pore morphology is lamellar and therefore beneficially open and interconnected. Aligned and lamellar pores are also advantageous with regards to the piezoelectric properties, due to improved poling of the ceramic matrix, as compared to structures with isotropic or unoriented pores [20]. Freeze casting thus appears to be a promising method for the preparation of piezoelectric ceramics for bone replacement.

1.2 Aim of the work

There are currently not many reported studies on freeze casting of BCZT [21]. This thesis therefore aimed to investigate the viability of water-based freeze casting as a method to producing porous BCZT appropriate for biomedical applications. The main objectives of the work were to develop a suitable slurry for freeze casting, investigate the change of the pore size with freezing rate and determine the effect of the resulting lamellar structure on the piezoelectric properties of the material.

The first step to achieving a successful freeze cast structure is the formation of a suitable slurry. In particular, the suspension must be well-dispersed and remain stable throughout the whole freezing step to avoid potential agglomeration and sedimentation. A slurry consisting primarily of solid state synthesized BCZT powder and deionized water was proces- sed. Continuous optimization of the BCZT-slurry composition, with regards to solid load and the quantity of additives, and mixing routine was conducted until an appropriate freeze cast structure with aligned and lamellar pores was achieved. A sedimentation test and measurements of zeta potential were performed to check for the stability of the suspensions.

As the viscosity of the slurry largely influences the formation of the lamellar structure during freezing, the viscosity of the slurries were also recorded. Unidirectional freeze casting of the slurries was conducted in a homemade freezing setup with liquid nitrogen as the cooling agent. The imposed freezing rate is one of the most common ways of altering the size of the lamellar pores. Several cooling rates were therefore tested and their effect on the final structure was examined with a SEM. Finally, as the introduction of pores into a ferroelectric is known to reduce the piezoelectric properties of the material [20], the piezoelectric properties of the freeze cast samples, specifically polarization, strain and the piezoelectric coefficient, were measured and compared to dense reference samples.

Chapter 2

Introduction

2.1 Piezoelectricity

Piezoelectricity is a property of certain dielectrics, for which there is a coupling between mechanical stress and polarization. Unlike normal dielectrics, a piezoelectric solid can develop a surface charge upon the application of a mechanical stress, even without the presence of an external electric field [22]. This is termed the direct piezoelectric effect. The reverse process, or converse piezoelectric effect, is also possible, where the application of a voltage results in mechanical deformation of the crystal. The two processes are illustrated in Figure 2.1.1, which demonstrates that the mechanical force applied in the direct effect can be both compressive and tensile. Likewise, the resulting strain in the converse effect can cause both elongation and contraction of the piezoelectric crystal [23].
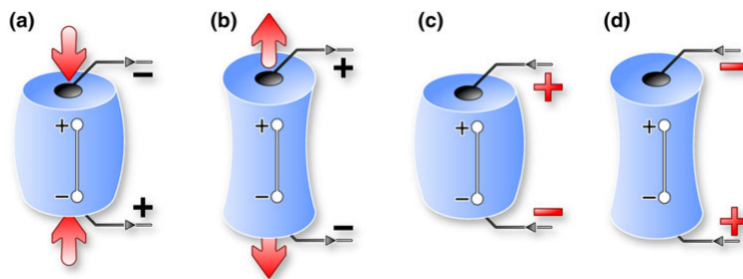
Figure 2.1.1: An illustration of the direct piezoelectric effect, where the application of a compressive (a) or tensile (b) force leads to the formation of a surface charge, and the converse piezoelectric effect, where the application of an electric field equal (c) or opposite (d) to the materials polarity yields a change in shape [24].

The piezoelectric effect is quantified by a value known as the piezoelectric coefficient, d, which measures the relationship between the electric displacement D generated per unit stress σ in the direct effect and the level of strain S induced per unit voltage E applied in the converse effect, as shown in Equation 2.1 [23]. The degree of polarization that develops in the solid

is dependent on both the magnitude and direction of the applied stress. The piezoelectric coefficient is therefore a third rank tensor, but is, however, usually given in the simplified notation d_{ij}, where "i" and "j" denote the direction of the generated electric displacement or applied electric field and applied stress or generated strain, respectively [23]. The longitudinal coefficient, d_{33}, is a commonly reported value and is defined as the piezoelectric constant when the induced strain and applied field are in the same direction, and parallel to the poling field (the process of poling is described in Section 2.1.1).

$$d = \frac{D}{\sigma} = \frac{S}{E} \tag{2.1}$$

The polarization that forms in a piezoelectric material is due to the generation of dipoles in the crystal unit cells, as the solid is subjected to an external stress [22]. Dipoles arise as the mechanical force induces the movement of positive and negative ions, so that their centres of gravity no longer coincide. It thereby becomes clear that piezoelectricity is only possible for crystals with a non-centrosymmetric point group, as otherwise the shift of ions would be symmetric and no dipoles would form. Piezoelectricity can therefore only be observed in materials from 20 of the 32 crystallographic point groups. The total polarization is the sum of all the dipoles in the material, and considering symmetry the effect should not be observed in a polycrystalline solid. This is due to the fact that all the grains are randomly oriented to each other, and will consequently polarize in different directions, yielding zero net polarization and no observed effect. Nevertheless, for certain materials, namely ferroelectrics, this can be overcome through the process of poling, which is further described in Section 2.1.1.

2.1.1   Pyro- and ferroelectricity

Pyroelectrics are a subset of piezoelectrics, which display a net polarization without the presence of neither an external electric field nor a mechanical stress [22]. The polarization of a pyroelectric solid is therefore said to be spontaneous, and its magnitude shows a reversible change upon heating and cooling. To exhibit this behavior, the material must, as in a piezoelectric, belong to a non-centrosymmetric point group. In addition, the elementary dipoles must lie on a unique polar axis, which is a direction showing no symmetry relation to any other direction in the crystal unit cell. There are 10 crystal classes that fulfill this requirement and can therefore demonstrate the pyroelectric effect. In general, pyroelectric behaviour is a result of the movement of atoms from a symmetric to a non-symmetric position in the crystal unit cell, thus creating internal dipoles and a spontaneous polarization. In some pyroelectrics, the spontaneous polarization can switch direction by the application of an electric field. Such materials are known as ferroelectrics. At high enough temperatures, the position of the atoms becomes statistical, as their thermal motion will promote reorientation. There is, therefore, a temperature, namely the Curie temperature or Curie point T_C, at which the ferroelectric state breaks down and the material becomes paraelectric.

Upon cooling from the Curie temperature, the dipoles that form in a ferroelectric solid will separate into several domains, which are defined as homogeneous regions within which the polarization directions are the same [22]. Between domains the dipoles are oriented differently and the boundary separating them is termed a domain wall. Domains form as a way to reduce the electric and elastic energy of the system, as the material transitions to the low-symmetry ferroelectric phase [23]. As-prepared ferroelectrics do not display a macroscopic polarization, due to the random orientations of grains, domains and dipoles, as shown in the insert at point O in Figure 2.1.2, leading to an overall cancellation of the effect [22]. An observable polarization can however be achieved through the process of poling, where the application of an electric field, point A in Figure 2.1.2, induces polarization switching and growth of the domains with a favourable orientation [25]. The domains will continue to switch until the overall polarization is best aligned with the applied field, considering grain orientations, at which point the material has reached the saturation polarization (P_S), point B in Figure 2.1.2. Upon removing the field, although some domains will begin to switch back, the ferroelectric will not return to its original state, but a remnant polarization (P_R) will be retained in the solid, illustrated at point D in Figure 2.1.2. If the external electric field is switched, point F in Figure 2.1.2, the dipoles will realign in the opposite direction and again reach saturation at point G in Figure 2.1.2. The overall polarization can be reduced to zero by setting the external field to a value known as the coercive field (E_C) of the ferroelectric. The P_S, P_R and E_C are specific to each material system and form a characteristic hysteresis loop, as shown in Figure 2.1.2. Poling makes is possible for the ferroelectric to exhibit an overall piezoelectric effect, and hence, ferroelectrics are most often used for piezoelectric applications. The development of ferroelectrics has made it possible to exploit both the direct and converse piezoelectric effect for a range of industrial applications, such as sensors, transducers and actuators.
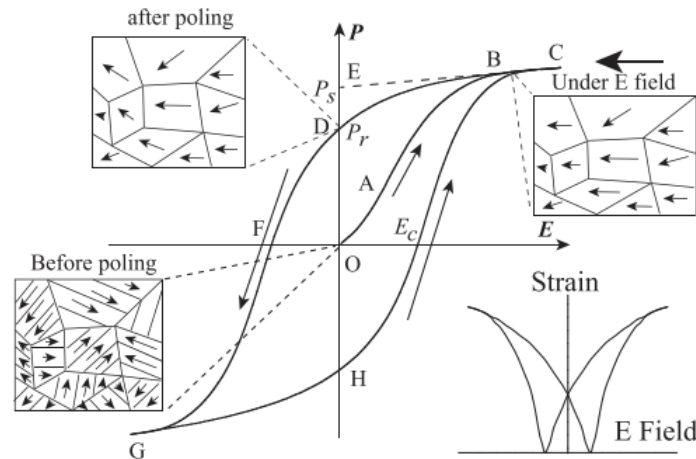
Figure 2.1.2: Classic ferroelectric hysteresis loop, showing the effect of domain switching on the polarization and strain of a ferroelectric solid, and marked with the corresponding saturation polarization (P_S), remnant polarization (P_R) and coercive field (E_C). The arrows indicate whether the applied electric field strength is increasing in the positive or negative direction. The inserts illustrate the orientation of the domains in the grains at each stage [26].

2.1.2   Porous ferroelectrics

The presence of pores in ferroelectrics is usually regarded as a material defect, due to the fact that it diminishes both the piezoelectric and of course mechanical properties of the material. However, as previously stated, large and interconnected pores are an essential feature in scaffold design, as they aid the formation of a stable fixation between the host tissue and implant [1]. Nevertheless, pores both increase the chances of dielectric breakdown and affect the poling ability of the ferroelectric matrix, thereby decreasing the piezoelectric properties of the material. It is important to understand the mechanisms by which this occurs, so that the porosity can be tailored in a way that a balance is struck between pore content and piezoelectric properties.

Dielectric breakdown occurs when a current flows through an insulator, thereby eliminating its dielectric properties [27]. Because air-filled pores have a lower dielectric breakdown strength than a ferroelectric, porous ferroelectrics are more susceptible to dielectric breakdown, as compared to a dense solid [28, 29]. The dielectric breakdown strength expectedly decreases with increasing porosity and pore size [30]. The shape of the pores is also a deciding factor, as irregular shaped pores are more detrimental to the breakdown strength than spherical pores. This is due to the fact that irregular pores enhance the electric field at the ferroelectric matrix adjacent to the pore surface that is parallel to the applied field. Furthermore, due to the low permittivity of air, charge will accumulate in the pores upon application of an electric field and result in a locally enhanced field [28,31]. This unfavourably increases the probability for partial discharge, meaning a localized dielectric breakdown, within the voids. As pointed out in Section 2.1, the piezoelectric properties of a ferroelectric material are uncovered through the process of poling, which requires the application of a high electric field. This is problematic, as an enhanced electric field within the pores could result in partial discharge, even at relatively low applied fields. It has been suggested that the electronic state of the internal pore surfaces may alter the apparent permittivty of the pores, and, thereby, also the probability of partial discharge [28]. The properties of the pore surface are likely to vary from material to material, and could explain why some materials are easier to pole in the porous state than others, as demonstrated for BCZT by *Yap et al.* [28]. The process of poling is nevertheless more difficult for porous ferroelectrics.

Previous studies show that the piezoelectric properties, specifically the saturation polarization, remnant polarization and piezoelectric coefficient, of porous ferroelectrics are poorer than for their dense counterparts [20, 21, 28, 32, 33]. This is primarily due to a smaller amount of active material available to polarize [28]. The piezoelectric properties clearly decrease with increasing porosity, however the reduction in the piezoelectric properties can not simply be accounted to the volume fraction of pores present, such as by Equation 2.2 for the remnant polarization,

$$P_R = P_R^0(1 - v_p) \tag{2.2}$$

where P_R is the remnant polarization of the porous material, P_R^0 is the remnant polarization of the dense material and v_p is the volume fraction of pores present. The large discrepancy between the low-permittivity pores and high-permittivity ferroelectric forces the electric field to primarily move around the pores, and results in an inhomogeneous electric field distribution in the surrounding matrix. By comparison, the electric field distribution is relatively homogeneous in a dense bulk ferroelectric [21]. As alluded to above, high-field and low-field regions arise at the ferroelectric-pore boundaries, which are parallel and perpendicular, respectively, to the applied field. A reduced local field could lead to incomplete poling of the given volumes of the material, which would in turn yield a reduced piezoelectric response. Statistical studies conducted by *Khachaturyan et al.* suggest that the electric field distribution across a porous ceramic is relatively independent of pore size and pore size distribution [34]. This depolarization factor is, however, dependant on the shape and orientation of the pores. The electric field distribution in and around an elliptical pore is shown in Figure 2.1.3a. The size of the low- and high- intensity areas decrease and increase, respectively, with increasing angle between the pore and the applied electric field [21]. Therefore, the larger the angle (up to 90°), the larger the volume of unpoled ferroelectric, as modelled for barium titanate (BaTiO$_3$) in Figure 2.1.3b. Because irregular shaped pores can be oriented perpendicular to the applied field, porous ferroelectrics with irregular pores tend to have worse piezoelectric properties than those with spherical pores, which is supported by many experimental results [28, 32, 35]. The effect of pore orientation on the electric field distribution also explains why a porous freeze cast structure should achieve relatively good piezoelectric properties, and is described in Section 2.2.3.

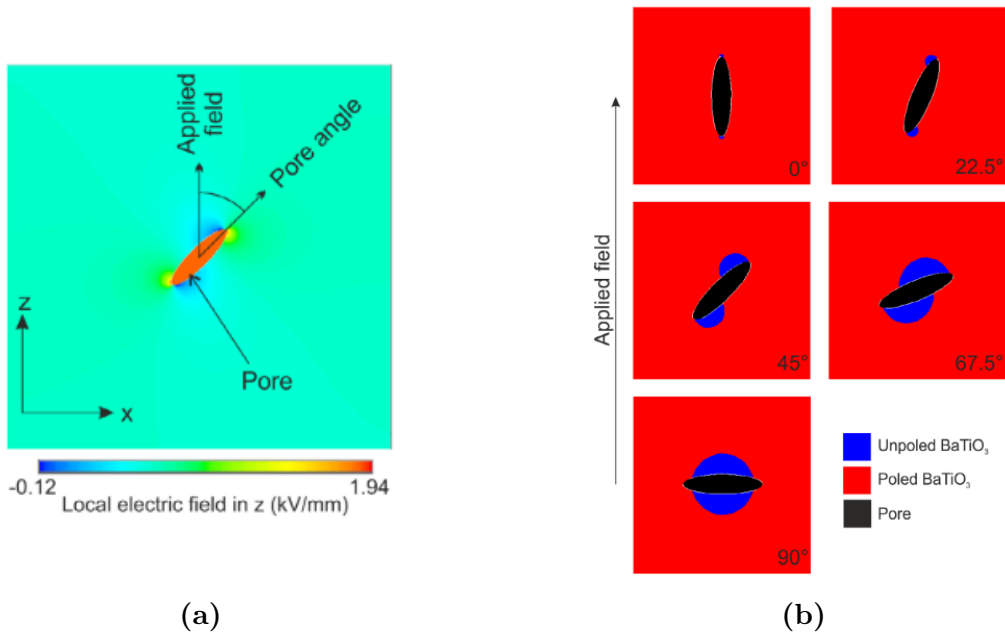(a)   (b)

Figure 2.1.3: Figure (a) is a model of the electric field distribution in and around an elliptical pore in a ceramic matrix. The color bar indicates the magnitude of the local field, with the applied field in the z-direction [20]. Figure (b) illustrates how the amount of unpoled regions varies depending on the angle, with respect to the applied field, of the pore [20].

Although there is a general agreement that the introduction of pores into a ferroelectric solid degrades the piezoelectric properties, both experimental and modelling studies show mixed results with regard to the effect on the coercive field. *Lukacs et al.* reported an increase in the coercive field with increasing porosity for $BaTiO_3$ [36]. This was attributed to the fact that the effective electric field on the ferroelectric is lower, and that the applied field must therefore be higher to induce ferroelectric switching. On the other hand, *Zhang et al.* saw a decrease in the coercive field of BCZT and claim it is a result of reduced internal stress around the pores, which gives easier ferroelectric switching [33]. Some have even reported no change in the coercive field with increasing porosity, such as in the study for lead zirconate titanate conducted by *Zhang et al.*, where it was assumed this was due to the accumulation of space charge at the pore surface [35]. An experimental study of porous BCZT conducted by *Zhang et al.* shows an initial decrease in the coercive field at porosities below 30%, followed by an increase above 30% [21]. Here it is discussed that at low porosities, the presence of pores facilitates ferroelectric switching and thereby yields a lower coercive field, whereas at higher porosities the effect of the inhomogeneous electric field becomes more dominant and results in an increase in the coercive field. However, as pointed out by *Schultheiß et al.* one should take care in comparing these results as full polarization would have to be assumed [37]. For porous samples, domain switching occurs at a broader and broader electric field distribution with increasing porosity and dielectric breakdown is likely to occur before the entire ferroelectric matrix is polarized.

2.2   Freeze casting

Freeze casting, also commonly termed ice-templating, is a promising processing route for the fabrication of porous ceramic scaffolds for bone replacement. The method has in general grown considerably in interest over the past 20 years, as evidenced by the rapid increase in publications on the topic, displayed in Figure 2.2.1.

The technique consists of freezing a liquid ceramic particle suspension, sublimating the solidified solvent and finally sintering to consolidate the ceramic walls. During freezing, the suspended particles are rejected by the moving solidification front and consequently concentrated between the growing crystals. As this is a physical process, freeze casting is relatively independent of chemical interactions and hence a variety of materials can be ice-templated, achieving similar morphologies [38, 39]. This contributes to the tremendous versatility of the method, with studies conducted for ceramics, polymers, metals and carbon based materials [20, 40–42]. After sublimation, the powder arrangement achieved during freezing is maintained in the green body and the porous structure is thereby close to a direct replica of the solidified phase. Several types of architectures are possible to fabricate with the freeze casting process, such as cellular-, lamellar- and dendritic porous structures [43], illustrated in Figure 2.2.2, and even dense ceramics with complex shapes, where the formation and growth of large crystals is minimized [44,45]. The resulting pore morphology is

dependent on the nature of the freezing process, specifically whether the growth of the solvent crystals is unidirectional or randomly oriented, as in anisotropic- and isotropic freezing, respectively. The unique porous structures achievable by way of freeze casting makes it possible to fabricate materials with properties that could not be realized by their dense counterparts, such as high specific strength, high surface area, high permeability and good thermal resistance [46]. Ice-templating thereby demonstrates the potential to function as a processing method for materials suitable for a range of applications, from membranes and filtration devices to batteries and piezoelectric energy harvesters. The focus of this review will be on the anisotropic freezing method, and particularly the lamellar structure, as this is the most researched and applicable to bioceramics.
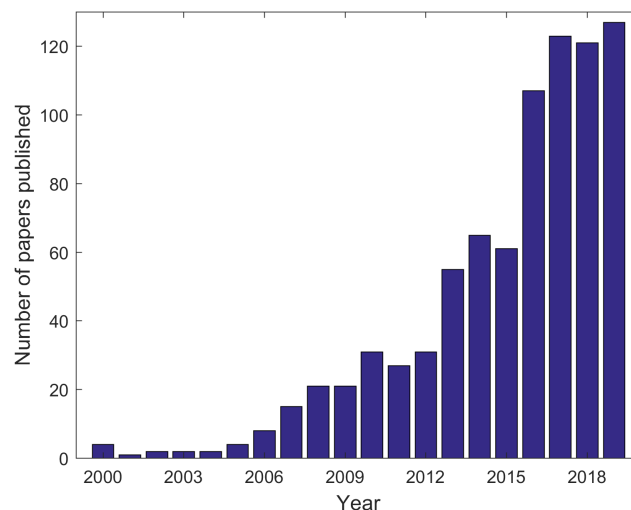

Figure 2.2.1: The number of papers on freeze casting published per year in peer-reviewed journals, from 2000-2019. The number of publications found is based on a search for the terms "Freeze casting" and "Ice templating", the most commonly used phrases to describe this processing method, in the title, abstract or keywords of peer-reviewed articles, using the Scopus database.

The porosity, in terms of pore -volume fraction, -size, -shape and -orientation, can also be tailored according to what solvent is utilized, the properties of the slurry and the applied freezing conditions. The most commonly used freezing vehicles are water and the organic liquids camphene and tert-butyl alcohol, although other solvents like naphtalene, dioxane and terpene have also been tested [47]. Important slurry properties include the particle size of the ceramic powder, solid loading, pH, viscosity and potential additives like surfactants and binders. Freezing conditions such as the freezing rate and design of the mold, which contains the slurry, will also affect the final porous architecture. The versatility and adaptability of the structure is one of the greatest benefits of freeze casting. Nevertheless, it also adds significant complexity to the process, as it becomes difficult to uncover the relationship between the applied processing conditions and resulting structure, with the many governing and interconnected parameters.
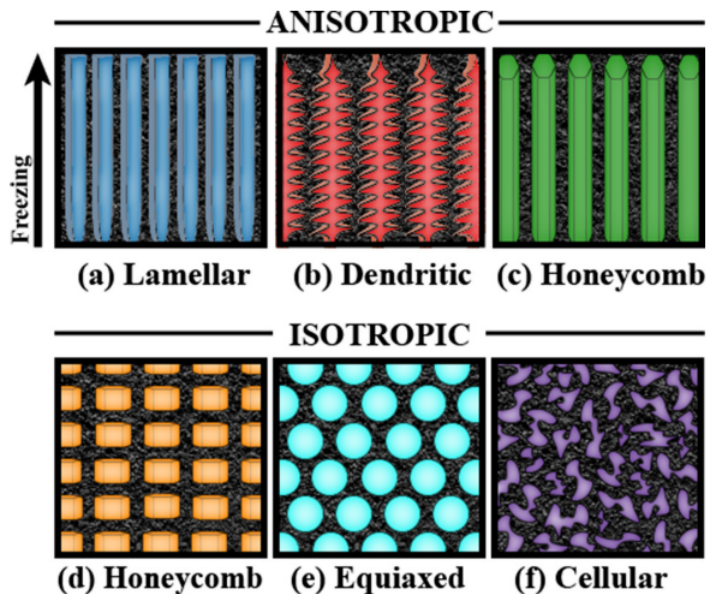
Figure 2.2.2: Schematic representation of common porous structures achieved through anisotropic- and isotropic freeze casting [43].

2.2.1   Freeze casting procedure

The freeze casting process can be divided into four essential steps: the preparation of a slurry, freezing of the slurry, sublimation of the solidified phase and sintering of the porous compact. A schematic of the process is given in Figure 2.2.3 and indicates the processing conditions and state of the solvent at each step. The procedure will here be described for a slurry consisting of ceramic powders in water, however, other freezing liquids will also be highlighted.

2.2.1.1   Slurry formation

The preparation of a slurry for freeze casting is very similar to the mixing of suspensions for conventional slip casting. First, a ceramic powder, i.e. the solid load, is combined with water, i.e. the freezing agent. Ball milling is a very common mixing procedure, although stirring with a magnetic bar is also used [8, 48]. The applied mixing ratio depends on the required final porosity, as the amount of water directly relates to the resulting pore volume. Most commonly, solid loads are around 10-40 vol% [39]. The choice of solvent is usually dictated by the type of pore morphology that is desired, as every solvent will solidify with a unique crystal structure and thereby yield different pore architectures (see Section 2.2.2). Nevertheless, it is important to note that the ceramic particles must have a low solubility in the solidified crystals in order to be expelled from the freezing front. Other general considerations are the viscosity, solidification temperature, price and environmental friendliness of the liquid solvent. It is also beneficial that the freezing agent has a high vapor pressure in the solid state,

so that sublimation can be conducted at a reasonable temperature and pressure. Finally, the solvent should experience minimal volume change during solidification, as this could lead to residual stresses in the frozen structure [49]. The chosen freezing vehicle will determine at what temperature the slurry formation, solidification and sublimation will take place. For example, a water-based slurry can be mixed at room temperature, but must be cooled to below 0 °C for freezing, while slurries containing camphene must be prepared at elevated temperatures around 60 °C, but can be solidified at room temperature.
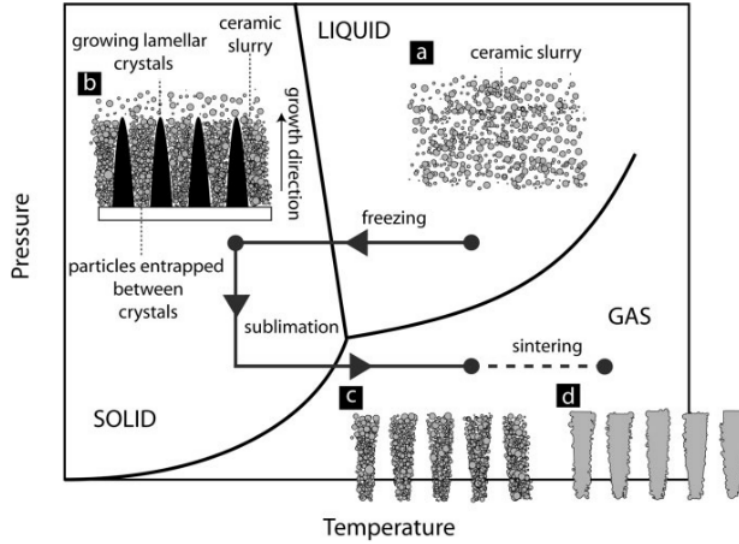

Figure 2.2.3: Schematic of the freeze casting procedure, showing the four processing stages of (a) slurry formation, (b) freezing, (c) sublimation and (d) sintering. The state of the solvent and the structure at each step is also displayed [39].

It is vital to the success of the freeze casting that the slurry remains well dispersed and stable throughout the whole freezing stage. Otherwise, complications of agglomeration and sedimentation, meaning settling of the powder particles, are likely to occur, resulting in inhomogeneities of density, porosity and microstructure throughout the final sample. As long as the density of the ceramic powder is larger than that of the solvent, sedimentation will occur to a certain extent. The rate of sedimentation is, however, dependent on several factors, such as the interaction between the ceramic particles and the properties of the solvent. The rate of sedimentation of a single particle can be calculated according to Equation 2.3,

$$v_p = \frac{2}{9}\frac{(\rho_p - \rho_l)gr^2}{\eta} \tag{2.3}$$

where v_p is the sedimentation rate of the ceramic particle, ρ_p is the density of the ceramic, ρ_l is the density of the liquid solvent, g is the gravitational acceleration and η is the dynamic viscosity of the solvent. Equation 2.3 is constructed from the balance of the gravitational, frictional and buoyancy forces felt by the particle when immersed in the solvent [49].

In general, the stability of a suspension is dependent on the repulsive forces between the ceramic particles being larger than the attractive forces, thereby preventing their close approach and interaction. *Lewis* describes the total potential energy, V_{total}, between two particles by equation 2.4,

$$V_{total} = V_{vdW} + V_{elect} + V_{steric} + V_{structural} \tag{2.4}$$

where V_{vdW} is the attraction potential from weak van der Waals interactions, its magnitude depending on the nature of the dispersed particles, V_{elect} represents the potential from electrostatic repulsion between like-charged particles, V_{steric} is a repulsive potential due to steric interactions between adsorbed polymeric species and $V_{structural}$ is the potential energy resulting from effects of non-adsorbed species, which can either be repulsive or attractive [50].

There are several approaches to creating a well dispersed suspension, the primary modes being electrostatic- and steric stabilization, which manipulate V_{elect} and V_{steric}, respectively. The electrostatic repulsion between particles in suspension originates from the formation of surface charges, as the solids are dispersed in a polar solvent or electrolyte solution [51]. The surface charge of oxides are typically determined by the interaction with the protons and hydroxide ions in water. The magnitude of this surface charge determines the degree of electrostatic repulsion and is dependent on the pH of the solution and the electrolyte concentration [50]. The pH corresponding to a zero-charged surface is termed the point of zero charge. Above the point of zero charge, the oxide particle is negatively charged, while below it is positively charged. By tailoring the aforementioned parameters, the repulsion can be made large enough to overcome the attractive forces and thereby keep the particles well-dispersed. This method is termed electrostatic stabilization, and is illustrated in Figure 2.2.5a. As the surface potential can not typically be measured, the electrokinetic potential or zeta potential is broadly used to describe the stability of suspensions. Due to electrostatic interactions, the charged particles in suspension will associate and bind to counter-ions (opposite charge to surface), co-ions (same sign of charge as surface) and polar solvent molecules, forming a characteristic electric double layer structure, as modelled in Figure 2.2.4 [52]. The zeta potential is defined as the potential at the shear- or slipping plane, which marks the interface between the mobile solvent and stagnant layer associated with the particle, when under the influence of an electric field [53]. The zeta potential is thereby closely related to the surface potential and a good indicator of the stability of a suspension. The higher the absolute value of the zeta potential, the more stable the suspension, but generally a zeta potential of about ±30 mV signifies a good dipsersion [54].

In some cases, electrostatic stabilization by adjustment of the pH is not sufficient to obtain a stable dispersion. Steric stabilization is another widely used method, where the adsorption of a polymeric species on the surface of the dispersed particles leads to steric interactions and, thereby, increased repulsion between the particles, as shown in Figure 2.2.5b [50]. The repulsive force is a result of interpenetration or compression of the polymer layers, as the particles approach one another, which leads to an increase in the Gibbs free energy of the
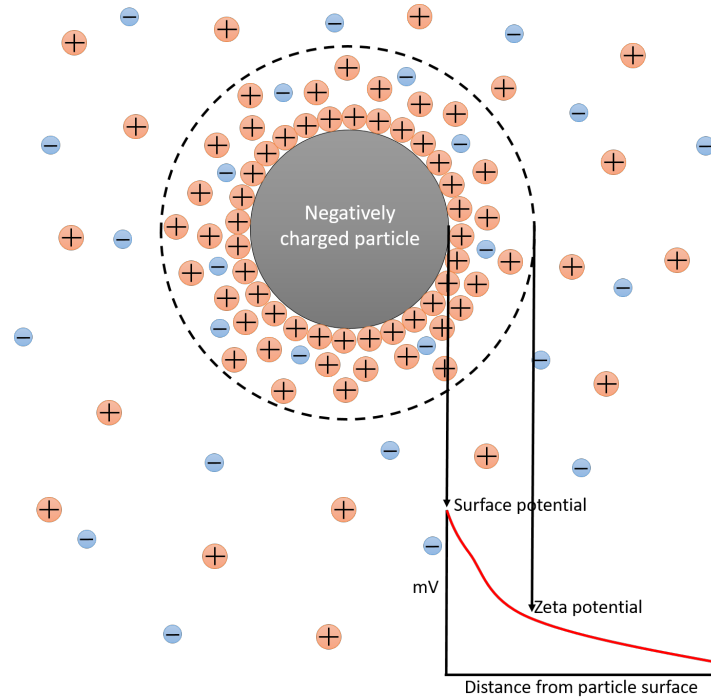
Figure 2.2.4: Model of the electric double layer structure around a particle in suspension, marked with the position of the surface charge and zeta potential.

system [51]. The level of repulsion depends on the thickness, density and conformation of the adsorbed layer, which in turn varies according to the number of active surface cites on the dispersed particle, the nature of the polymer and the concentration of both species in the suspension [50]. In practice, stabilization is often maintained by a combination of the two outlined methods, referred to as electrosteric stabilization. This is can be achieved by the use of a polyelectrolyte surfactant, which is characterized by the presence of ionizable groups that modify the surface charge of the dispersed particle. Ammonium polymethacrylate, for example, is an ammonium salt of polymethacrylic acid, which, when dissolved in water, contains negatively charge acetate groups that can bind to the positive surface sites of the ceramic particles [55]. Stabilization is both achieved by the negative charge of the functional group and the presence of the polymer chain, and thus electrosteric in nature. The adsorption of the polyelectrolyte is dependent on the pH and ionic strength of the solution and the charge of the dispersed particle. For instance, adsorption is promoted when the polyelectrolyte and particle carry opposite charges. Several different dispersants have been employed in freeze casting studies, such as ammonium polymethacrylate (mentioned above), ammonium polyacrylate and carboxylic acid [56].

In addition to a surfactant, it is usually necessary to add a binder to the slurry, to increase the strength and ease of handling of the porous green body after sublimation of the solidified solvent [39]. Otherwise, the structure will often collapse during the drying stage, as the packing density in the frozen structure is below that achieved with other conventional ceramic processing routes [56]. The mechanism, by which the binder bridges the ceramic particles
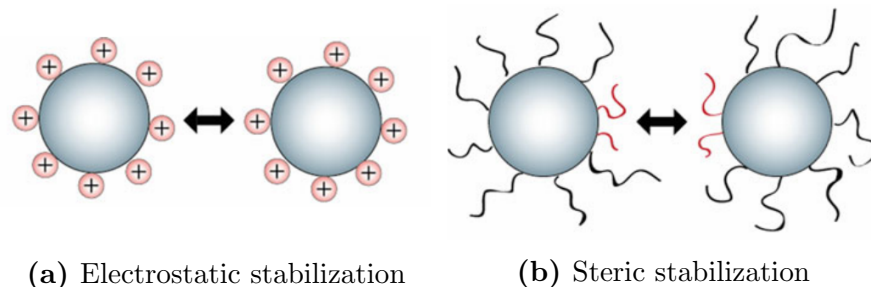
(a) Electrostatic stabilization   **(b)** Steric stabilization

Figure 2.2.5: Illustration of the two primary stabilization methods [57].

together, depends on what type of binder is employed. Polyvinyl alcohol (PVA) is the most commonly used binder in samples for freeze casting, but others such as polyethylene glycol and polyvinyl butyral have also been employed [56]. PVA is an adhesive polymeric binder, which bridges particles together through the formation of hydrogen bonds between the hydroxyl side group of its repeating structural unit and the surface of the particle [58]. PVA works well for most oxide particles in water. Regardless of which binder, and surfactant, is utilized, it is important to note that additives can have a significant effect on the final pore morphology, as will be discussed further in Section 2.2.2.

Viscosity is another decisive slurry parameter, as it has a substantial effect on the final freeze cast microstructure, specifically the long range order of the pores and the formation of defects, and also the sedimentation rate of the slurry. The viscosity is determined by both the particle size and shape of the ceramic powder, the solid load, the interactions between the particles and the pH of the slurry [59, 60]. The stability of a dispersion is often evaluated by measuring the viscosity, which should be at its minimum when the most optimal dispersion is reached [59]. Due to the many parameters that affect the viscosity, and thereby microstructure of the ice-templated structure, trial and error must be carried out to establish what slurry composition gives the best outcome, in each material system.

During mixing of the slurry, air bubbles can form and be incorporated into the suspension [56]. A degasification step under partial vacuum is therefore needed, as otherwise the bubbles could result in spherical pores in the sintered structure. In some cases, the formation of bubbles can be manipulated to create several levels of porosity and a foam-like architecture [59]. For freeze casting of bioceramics for bone replacement, spherical pores are not desired, as they are detrimental to the mechanical and piezoelectric properties of the structure.

2.2.1.2   Freezing

Once a stable slurry has been prepared, the suspension is poured into a mold, most commonly made from rigid and non-sticky polytetraflouroethylene (PTFE) [56]. There are many different types of setups for freezing of the slurry, and the chosen method depends on the

desired porosity and to what degree the process should be controlled. When water is used as the freezing vehicle, solidification must clearly take place below 0 °C. The most simple and cheapest way of achieving this is by placing the slurry in a conventional kitchen freezer, where temperatures are typically below -25 °C. Although it can be aided by the use of a thermally insulating mold, directional solidification is relatively difficult in this case and the structure tends to be more isotropic [43, 56]. In the application of bone replacement materials, the possible anisotropic structure is one of the primary benefits of the freeze casting method, and directional freezing is thus favorable. A typical setup for directional freezing is shown in Figure 2.2.6 [61], where the suspension is cooled from below. Here the insulating mold is fitted with a thermally conductive base, often made of copper. The mold is placed with the base onto a copper rod or cold finger, which is cooled in a liquid nitrogen bath. Liquid nitrogen works well in the sense that it can provide low temperatures. However, it also readily evaporates, making it difficult to maintain a consistent amount and thereby proper control of the cooling rate [56]. This can be partially mitigated by covering the bath with a polystyrene lid. Cooling of the bottom plate leads to nucleation of ice crystals, and the temperature gradient in the slurry promotes their directional growth [43]. The temperature, and thus cooling rate, is controlled by a ring heater, thermocouple and temperature controller [56], and is most often between 1-10 °C/min [38]. Other freezing setups, for example cooling simultaneously from above and below or imposing a radial temperature gradient, are also possible, but will not be presented here.
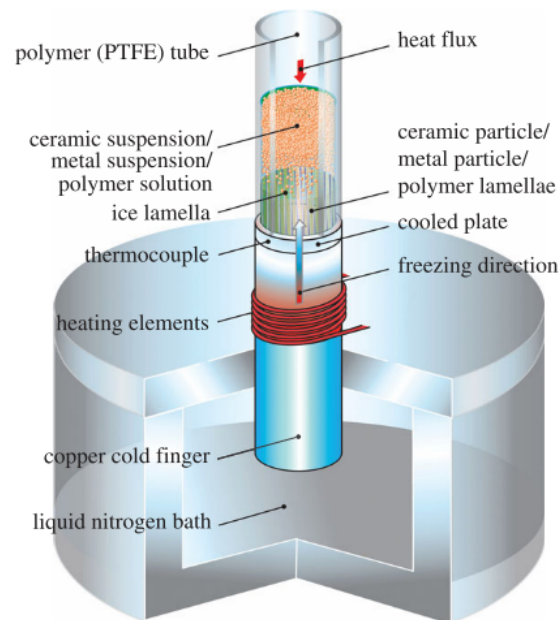

Figure 2.2.6: Illustration of a typical one-sided cooling setup for freeze casting, where the slurry is cooled from below with liquid nitrogen [61].

Freezing of the slurry is the core stage of the freeze casting process and is critical, as it determines the characteristics of the final porosity. The formation of the lamellar porous structure is dependent on the fulfillment of two requirements. Firstly, the ceramic particles

must be repelled by the moving solidification front and consequently piled up between the growing crystals, as shown in Figure 2.2.3 [39]. Thermodynamically, this means that the engulfment of a ceramic particle by the ice would be associated with an increase in the free energy of the system, $\Delta\sigma$, indicated in Equation 2.5,

$$\Delta\sigma = \sigma_{sp} - (\sigma_{lp} + \sigma_{sl}) > 0 \tag{2.5}$$

where σ_{sp}, σ_{lp} and σ_{sl} are the interfacial energies of the solid-particle, liquid-particle and solid-liquid interfaces, respectively [39]. In addition, rejection of the particles by the solidification front is dependent on the presence of a thin liquid film between the particle and the solid, to maintain transport of water molecules to the growing crystals. The higher the solidification front velocity, the smaller the thickness of the film. There, therefore, exists a critical velocity, at which the flow of molecules is hindered and encapsulation of the particle occurs. The critical velocity is derived from the balance of attractive and repulsive forces experienced by the particle and given in Equation 2.6,

$$\nu_c = \frac{\Delta\sigma d}{3\eta R}\left(\frac{a_0}{d}\right)^n \tag{2.6}$$

where a_0 is the distance between molecules in the liquid film, d is the thickness of the layer, η is the dynamic viscosity of the solvent, R is the radius of the ceramic particle and n is an empirical correction factor [62]. Engulfment of the ceramic particles is clearly detrimental to the desired lamellar porous structure as there would be no distinction between regions of ice and ceramic after freezing.

The second condition for the formation of lamellar porosity is that the ice front must have a non-planar morphology, as the nature of the solidification front determines the overall structure of the ice and thereby the porous architecture [39]. Rejection of the ceramic particles by a planar ice front would simply result in an accumulation of particles at one side of the sample, whereas rejection from a lamellar front leads to accumulation of ceramic particles between the ice crystals, and consequently a lamellar structure. It has, however, generally been believed that at the onset of solidification, the ice-front indeed is planar, and must therefore transition to a lamellar or dendritic morphology at some point during the freezing. The transformation has been considered to occur through two possible mechanisms. The first is based on a constitutional supercooling at the interface, namely the Mullins-Serkerka instability. The second is based on the effect of the dispersed particles, which locally alter the thermal gradient. However, more recent *in situ* x-ray studies show that the initial freezing interface is not planar, and that the onset of the aligned lamellar structure is controlled by other mechanisms [63].

2.2.1.3 Sublimation

After the slurry is fully frozen, the time for which will vary greatly depending on the applied cooling rate and the amount of slurry, the sample is extracted from the mold. The ice is thereafter removed by sublimation, meaning it is directly converted to the gas state as indicated in Figure 2.2.3. For sublimation to occur, the temperature and pressure must be below that of the triple point of water, which lies at 0.01 °C and 0.00605 atm [64]. Otherwise, the ice would melt and the phase distribution achieved during freezing would be compromised. This is due to the fact that the inter-particle forces are usually not strong enough to hold the ceramic layer together, and there is a significant volume decrease with melting [57]. The sample is favorably not dried in the mold used for freeze casting, as this would increase the chances of defect formation, due to inhomogeneous drying. In addition, the sample can be quite fragile after sublimation and would be difficult to successfully remove from the mold. The conditions required for sublimation will depend on which solvent is employed. If for example camphene is utilized, sublimation can be conducted at room temperature and atmospheric pressure. After complete removal of the ice, air-filled pores remain in its place and are thereby a direct replica of the solidified phase.

2.2.1.4 Sintering

The final step in the freeze casting technique is to conventionally sinter the porous green body, with a sintering routine that is suitable for the applied ceramic. Sintering is a thermal treatment which causes the ceramic particles in the powder compact to bond together and thereby form an overall stronger and more solid structure [65]. This occurs through several atomic mass transport mechanisms such as various modes of diffusion. During sintering, two main events occur: densification and grain growth. For a freeze cast microstructure, this should result in the removal of the microporosity that is present in the ceramic layers, while the templated macropores, and their shape, are retained [39].

Although the macropores should remain in the structure after sintering, significant shrinkage will nevertheless occur, and the final porosity will be lower than the corresponding vol% of solvent utilized in the slurry. *Deville* states that for ceramics, sintering typically reduces the porosity by about 10-25% [57]. Shrinkage also appears to be anisotropic, due to the anisotropy of the microstructure [66]. It is unclear how the solid loading of the slurry will affect the level of shrinkage, as both decreased and increased shrinkage with increasing solid load have been reported [67,68]. It is worth noting that the characteristics of the ceramic powder, such as particle size distribution, particle shape and packing in the green body, and the sintering conditions of time, temperature and atmosphere will clearly have an effect on the level of densification achieved [65]. Once sintering is complete, the goal is that a dense ceramic matrix, with controlled macroporosity should be achieved.

2.2.2   Characteristics of the final structure and the influence of processing parameters

One of the principal benefits of the freeze casting method is the versatility of pore morphologies that can be fabricated, through tailoring of the processing conditions. The porous structure can, thereby, be adjusted to fit the specific requirements of for instance porosity, pore size and pore shape, for a range of applications. In the matter of ceramics as bone replacement materials, large and interconnected pores of above 100-150 μm in size are required [1]. Further, the porosity must be large enough to allow for sufficient bone ingrowth, but nevertheless not so high that the mechanical properties become too depleted. It is essential to understand how the processing parameters affect the final structure, so that the freeze casting process can be optimized with respect to each specific application and material system. The general characteristics of a freeze casted structure, and several methods of altering it are described below.

The nature of the solvent is the most important parameter governing the morphology of the pores achieved by freeze casting, as the pore structure is close to a direct replica of the solidified phase. Both the crystal structure and growth kinetics of the freezing vehicle will determine the porous architecture [20]. Water, which is the most commonly used solvent, solidifies into ice with a hexagonal crystal structure, displayed in Figure 2.2.7a. The growth of ice is highly anisotropic, being around 100 times lower perpendicular (c-axis) to the basal plane as compared parallel (a-axis) to the basal plane [39], as illustrated in Figure 2.2.7b. This results in preferential growth of crystals with their basal plane aligned parallel to the imposed temperature gradient, resulting in the formation of 2D-sheets and the characteristic lamellar structure found with one-sided unidirectional freezing, shown for barium titanate in Figure 2.2.7c. Ice grows with a dendritic morphology and limited growth perpendicular to the basal plane therefore causes the formation of surface dendrites on the ice lamella. This will translate to a surface roughness on the ceramic walls in the final material. The size of the dentrites can vary depending on among else the properties of the suspension and the freezing conditions. As the presence of such a surface roughness in bone replacement materials could be beneficial to cellular response, this should also be optimized [19]. Although many different solvents can be utilized for freeze casting, water remains a popular choice due to its low cost, environmental benefit and convenience of use [18]. Moreover, for piezoelectric ceramics implants, the lamellar structure proves to be beneficial to the piezoelectric and mechanical properties, as explained in Section 2.2.3. Camphene and tertbutyl-alcohol, the two other most commonly used solvents, would yield dendritic and prismatic solidified crystals, respectively, such as those shown in Figure 2.2.2, however these structures will not be discussed further.

Many freeze casting studies, including works by *Deville et al.* [19,62], report that the ceramic structure does not immediately adopt the lamellar morphology. In fact, three distinct zones with different structures can usually be distinguished, as illustrated in Figure 2.2.8 [19]. A dense ceramic layer is found in the zone that is frozen first (closest to the copper plate).
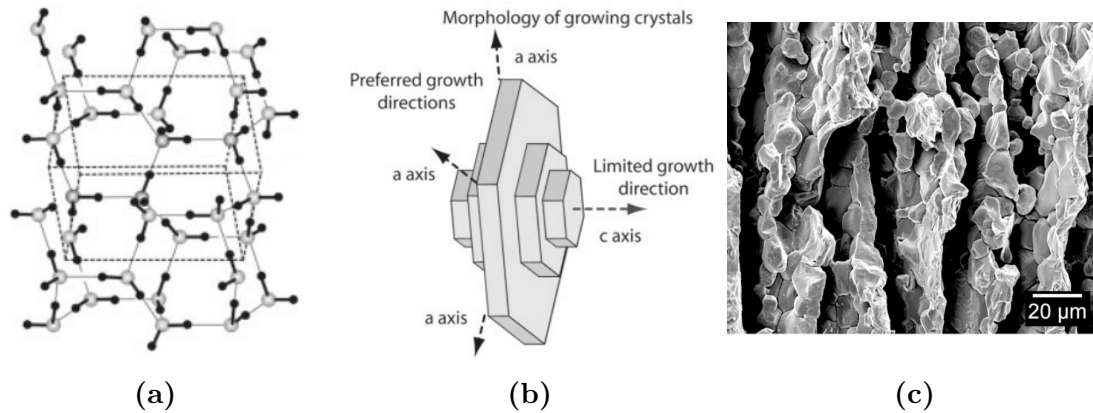
Figure 2.2.7: The hexagonal crystal structure (a) and anisotropic growth of ice (b) [39], yielding a lamellar freeze casted structure (c) after sublimation and sintering [20].

The structure then transitions to a cellular regime, consisting of pores with no particular alignment, before finally forming the steady state unidirectional lamellar architecture in the third zone. The dense bottom layer is a result of encapsulation of the ceramic particles from the initially fast-growing ice. The growth rate of the ice crystals is relatively high at first, as the suspension tends to be supercooled once the ice nuclei reach their critical size [49]. The subsequent release of latent heat upon formation of the ice locally increases the temperature and therefore reduces the freezing front velocity until a steady state condition is reached. Once the growth rate of the ice falls below a critical velocity, the particles will be rejected by the solidification front and porosity can be formed. As briefly described in Section 2.2.1.2, several theories exist on how the transition to the lamellar morphology occurs, and thus far there does not appear to be a full understanding on the topic. Nevertheless, zone 2 marks the region where the ice crystals with the preferred orientation, that continue to grow in zone 3, are selected. *Deville et al.* propose that the size of the transition layer (dense and cellular zone) increases with increasing particle size [69]. However regardless of its size, the transition layer should for most application purposes be cut off after sintering, as it does not display the desired microstructure. Figure 2.2.8 also shows that the lamellar structure is usually arranged in domains, where the lamella are locally parallel to each other. These so called orientation domains are constructed as the ice will nucleate and grow simultaneously at several locations at the onset of freezing [49].

The solid loading, meaning the concentration of ceramic powder in the initial slurry, is the most important parameter controlling the total porosity in a freeze casted structure [57]. It directly determines the amount of solvent available for freezing and, thereby, templating of pores. However, as stated in Section 2.2.1.4, the final porosity after sumblimation and sintering will always be lower than the volume fraction of solvent employed in the slurry, due to shrinkage. As long as all other parameters, such as the freezing rate, remain constant, the porosity should be inversely proportional to the solid load. In principle, a whole range of porosities from 0-99% can be achieved through freeze casting, though certain limitations due exist in the case of macroporous ceramics [38]. If the solid load is very low, the strength
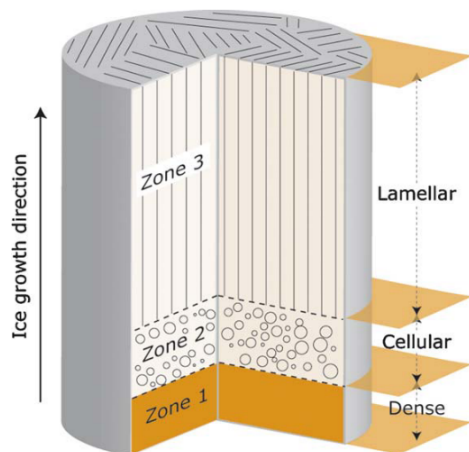
Figure 2.2.8: Illustration of the structural gradient present in freeze casted samples, resulting from the reduction in the freezing front velocity and development of the lamellar structure with time. The presence of orientation domains is also visible at the top of the structure [19].

of the green body could be insufficient, even with the use of a binder, and further processing could be problematic. On the other hand, if the solid load is to high, around 55-60 vol%, the ice front will no longer be able to repel the ceramic particles and thus no macroporosity will be formed. Moreover, a larger solid fraction yields a higher viscosity slurry, which favours the encapsulation of the ceramic particles by two main factors. First of all, a higher viscosity means the critical velocity for encapsulation of the particles by the freezing front will be lowered, according to Equation 2.6. Furthermore, the higher the viscosity, the more difficult it becomes to redistribute the particles during freezing due to an increased drag force acting on the particles [57]. *Zhang et al.* for instance demonstrated that the increase in viscosity for a solid loading of 40 vol% hydroxyapatite in water (with additives) resulted in closing of the lamellar pores [70]. The particle size of the solid load is also an important parameter, and must be small enough that the features of the ice crystals can be properly replicated [39].

One of the most common ways of modifying the porous freeze cast structure, specifically the size of the pores, is by changing the cooling rate of the bottom plate during freezing. The higher the cooling rate the smaller the resulting pore width and likewise, the lower the cooling rate the larger the pore width, making the two inversely proportional [19]. The reason for this relationship is that the degree of supercooling ahead of the solidification front becomes larger with increasing cooling rate, and thereby results in faster ice crystal growth. More rapid crystal growth in the direction of the temperature gradient both produces a smaller ice-tip radius and limits growth perpendicular to the freezing direction, which together contribute to forming thinner ice lamella and, therefore, thinner pores [46]. This has been demonstrated in several freeze casting studies for among else hydroxyapatite, alumina and a barium titanate/hydroxyapatite composite [8,19,62]. It is important to note that the freezing rate should not be too high or too low, as this could result in respectively the encapsulation of the particles by the ice or the growth of lateral crystals and thereby formation of cracks in the final structure [71]. Figure 2.2.9 demonstrates these principles, and in addition shows

how the particle size of the ceramic powder also appears to have an effect on the nature of the solidification front and the resulting structure, according to *in situ* X-ray radiography studies conducted by *Deville et al.* [71]. The green area indicates the region where a lamellar porous structure can be fabricated. It should be pointed out that the stability diagram will likely depend on the formulation of the suspension, for example by the presence of additives.
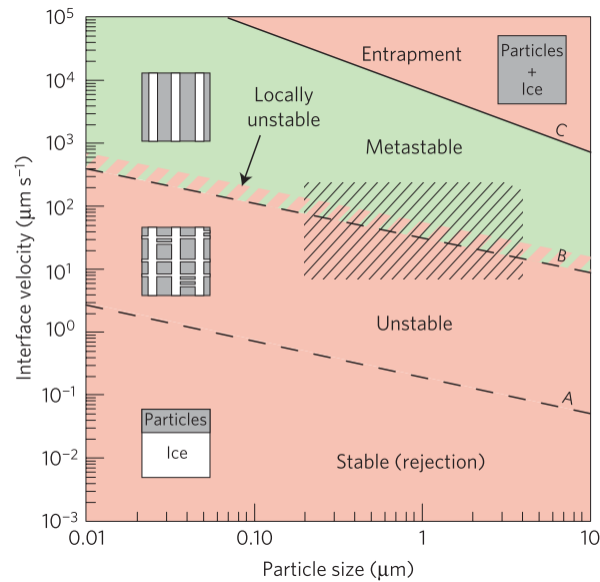

Figure 2.2.9: Diagram showing the dependency of the freeze cast structure on the interface velocity, which is directly related to the freezing rate, and particle size. The green area represents the region where a lamellar porous structure can be processed [71].

The addition of additives into the freeze casting slurry is usually a necessary step to ensuring successful processing of the structure. The most common are binders and dispersants, which provide respectively a stronger green body and more stable suspension, as described in Section 2.2.1.1. In some cases, additives can also be included to modify the pore structure by altering the freezing kinetics, crystal structure of the solidified phase or particle redistribution process [43]. For instance, increasing amounts of PVA in an aqueous alumina slurry has been shown to gradually transition the porous structure from lamellar to dendritic [72]. The effect of additives on the freeze cast structure are commonly associated with changes in the viscosity of the suspension, by the mechanisms mentioned above. *Zhang et al.* for example attributed smaller lamellar pore widths to larger additions of PVA to a water-based hydroxyapatite slurry, due to increasingly higher viscosities [70]. An interesting observation is that although a dispersant is usually required to achieve a well dispersed slurry, avoiding complications of agglomeration and sedimentation, studies indicate that the most stable dispersion does not always give the best outcome [59]. In fact, an optimal dispersion has been associated with the formation of ice crystals perpendicular to the freezing direction, which would serve as defects in the final structure.

2.2.3   Properties of the aligned lamellar structure

Freeze casting has gained considerable interest as a method of fabricating ceramics for bone replacement applications not only because it offers great control of the final structure, but also due to the beneficial properties that the lamellar structure provides. The advantage of the lamellar structure lies first and foremost in the inherent characteristics of the architecture, which in fact resembles biological structures such as bone [18]. The open and interconnected porosity in an ideal freeze casted structure has the potential to facilitate ingrowth of cells, vascularization and diffusion of nutrients into the implant, forming a strong fixation to the bone tissue. A study conducted by *Fu et al.* indicated that freeze casted hydroxyapatite was able to support proliferation, differentiation, mineraliztion and function of osteogenic (bone-growing) cells, demonstrating the promising ability of such structures to function as scaffolds for bone repair [73].

In addition to the inherent properties of the pore morphology, much attention has been given to the piezoelectric properties and poling-ability of the lamellar arrangement. As previously outlined, piezoelectric ceramics have the ability to deliver electrical cues that could stimulate bone growth, thereby demonstrating the potential to provide functionality to bone replacement implants [6]. It is therefore essential to consider how the piezoelectric properties are affected by the presence of pores, specifically in the lamellar system. In Section 2.1.2 it was proposed that the piezoelectric properties of a freeze cast structure with lamellar pores should be superior to its counterparts containing for example spherical pores. This is due to the fact that elliptical pores aligned parallel to the poling field produce a more homogeneous electric field distribution in the material than for instance spherical pores or elliptical pores tilted with respect to the poling axis [21]. The field distribution is more homogeneous as there is a smaller amount of ceramic matrix exposed to a low local electric field. A higher mean electric field results in more complete poling of the matrix, which directly relates to the improved piezoelectric response. An inhomogeneous electric field however signifies that poling will take place over a broader range of electric fields, which will be revealed in a tilting of the polarization loop.

Roscow et al. also demonstrate through finite element analysis that the amount of poled ceramic increases with increasing aspect ratio of the elliptical pores aligned to the field [20]. This is because the volume of ceramic at pore edges that are parallel to the applied field, which experience a higher local electric field, increases [21]. If the aspect ratio of the pores was increased significantly, it would reach the condition of the lamellar structure, where pores span the whole length of the sample. These concepts have been confirmed in both modelling and experimental studies, such as that reported by *Zhang et al.* and *Roscow et al.*, where the lamellar structure proved to have, respectively, a higher P_R and d_{33} than a uniform porous structure [20, 21]. In an ideal lamellar structure, where the porous channels run from the bottom to the top of the sample, the piezoelectric coefficient should be independent of porosity. This is because the lamellar structure should allow for the development of a homogeneous electric field and therefore yield complete poling of the whole ceramic [20].

However, in most practical cases, defects such as pores in the ceramic layers or ceramic bridges between the pores, will be present. Both types of defects result in a reduction of the d_{33}, but *Roscow et al.* reported that ceramic bridges were more detrminetal to the piezoelectric coefficient and suggested this may be due to strain restriction in the poled ceramic layers from the unpoled bridges.

It is worth mentioning that the mechanical properties of the lamellar structure is also of great interest, and the compressive strength is indeed the most measured property of ice-templated materials [74]. Mechanical properties are important to consider in the fabrication of bone replacement materials, as the implant will be exposed to mechanical loads *in vivo*. The implant must be capable of withstanding these loads, however, the mechanical properties can not be so high that the surrounding bone is not loaded properly, as this would result in a weakening of the bone over time [1]. The porosity must therefore be tailored, so that the mechanical properties of the material closely match that of the bone it is intended to replace. Ceramics are inherently brittle, and their strength only decreases by the inclusion of porosity. *Scotti & Dunand* report from a review of existing experimental data that the compressive strength to density ratio of porous ceramics appears to be better for anisotropic structures compared to isotropic structures at relative densities above 0.18 [43]. Nevertheless, a great amount of scattering is present and could be indicative to the presence of defects or differences in processing. To get a full understanding into the possibility of freeze casting as a method to producing bone replacement materials, mechanical properties and their dependency on porosity and pore size would have to be taken into consideration.

2.3   Barium titanate-based ferroelectric

Barium titanate doped with Ca^{2+} and Zr^{4+} cations at the A- and B-site, respectively, denoted by $(Ba_{100-x}Ca_x)(Ti_{100-y}Zr_y)O_3$, but hereafter written in the simpler notation BC_xZ_yT, has emerged as one of the most studied lead-free piezoelectric compositions. The Ba-based ferroelectric gained considerable attention upon the discovery of remarkably high piezoelectric coefficients of up to 620 pC/N with the addition of 15 mol% calcium and 10 mol% zirconium, by *Liu & Ren* [10]. Such a high piezoelectric response is comparable to that of the benchmark lead zirconate titanate (PZT) system, which despite containing large amounts of toxic lead, has been the most widely employed ferroelectric due to its superior properties. This promising result sparked a vast amount of research into a broader BC_xZ_yT composition range, where it has been attempted to uncover the origin of the exceptional piezoelectric properties.

It is well known that the piezoelectric properties of a system are closely related to its structural phase diagram, and a large effort has therefore gone into fully establishing the phase diagram of BC_xZ_yT. Particular attention is given to the presence of morphotropic phase boundaries (MPB), which designate a composition-driven phase transition between two ferroelectric phases [75]. Enhanced piezoelectric properties are generally found in the

MPB-region, as the coexistence of two phases permits more potential domain orientations and therefore greater ease of polarization rotation [76]. The phase diagram of BC_xZ_yT is known to consist of a high-temperature paraelectric cubic phase and ferroelectric rhombohedral and tetragonal phase regions, as originally set up by *Liu & Ren*. However since then, it has quickly become clear that the nature of the phase diagram is more complex. *Keeble et al.* resolved through high-resolution synchrotron x-ray diffraction and dielectric permittivity measurements the presence of an orthorhombic phase between the rhombohedral and tetragonal phases, suggesting the partial phase diagram shown in Figure 2.3.1 [77]. On the other hand, results from *Ehmke et al.* show a region of phase-coexistence between the ferroelectric phases, consisting of both the tetragonal and rhombohedral phases [78]. There, therefore, does not appear to be complete agreement on what occurs in this region.
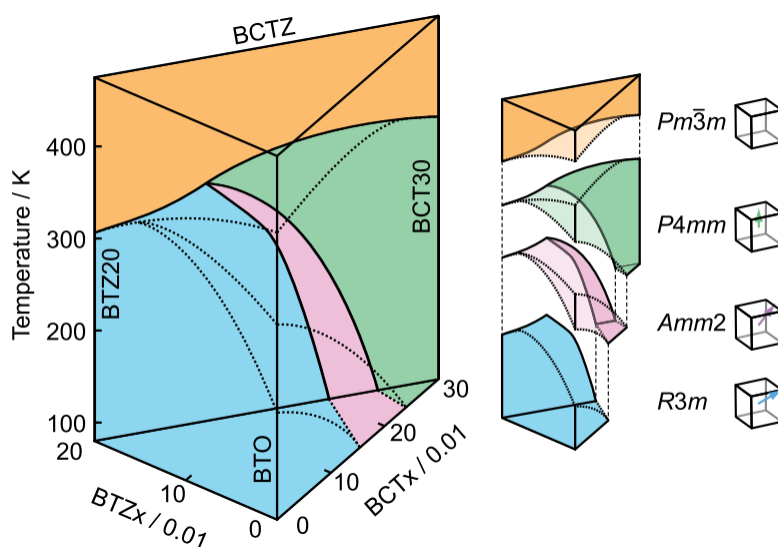

Figure 2.3.1: The 3D phase diagram of BCZT proposed by *Keeble et al.*, displaying the presence of cubic ($Pm\bar{3}m$), tetragonal ($P4mm$), orthorhombic ($Amm2$) and rhombohedral ($R3m$) phase regions [77].

The corresponding piezoelectric properties of various compositions of BC_xZ_yT have likewise been studied extensively. Much attention has been given to the presence of the MPB-region, which as stated above is known to display superior properties. *Tian et al.* suggest that the orthorhombic phase could function as a structural bridge between the tetragonal and rhombohedral regions, thus allowing for more possible polarization states [79]. In addition, piezoelectric properties increase as the composition approaches the point where the four phases meet, named the phase convergence region by *Keeble et al.*. *Zhou et al.* state that the high piezoelectric performance in this region may be explained by the fact that the energy required for the orthorhombic phase to transition to either rhombohedral or tetragonal phases would be reduced, as compared to further away from the phase convergence region, which would facilitate domain switching even further [80]. Other mechanisms such as domain miniaturization, ferroelastic texturing and the contribution from domain wall motion have also been explored and could contribute greatly to the high piezoelectric response [75]. The

d_{33} of BC_xZ_yT can vary vastly depending on the amount of Ca^{2+} and Zr^{4+} doping, with values ranging from $\approx$150-650 pC/N [79]. Large variations within the same composition have also been reported in different studies, possibly due to differences in processing conditions, microstructure, measuring techniques and poling conditions [75].

Chapter 3

Experimental

The BCZT powder was made through a solid state synthesis route from oxide and carbonate precursor powders. Ammonium polymethacrylate (Darvan C-N) and polyvinyl alcohol (PVA) were used as additives in the slurry made for freeze casting, and their molecular structures are given in Figure 3.0.1. All the materials used for sample preparation are listed in Table 3.0.1. The equipment utilized for sample synthesis and characterization is given in Table 3.0.2.

**Table 3.0.1:** Materials used for sample preparation.

Material	Chemical formula	Supplier	Purity [%]
Barium Carbonate	$BaCO_3$	Sigma-Aldrich	99.98
Titanium(IV) oxide, rutile	TiO_2	Sigma-Aldrich	99.99
Calcium Carbonate	$CaCO_3$	Merck KGaA	99.5
Zirconium dioxide	ZrO_2	Alfa Aesar	99.978
Ethanol	C_2H_6O	VWR International AS	96
Darvan C-N	$(C_3H_4COO^-)_n(NH_4^+)_n$	R.T. Vanderbilt Company Inc.	25[1]
Polyvinyl alcohol	$(CH_2CHOH)_n$	Sigma-Aldrich	99+[2]

[1] wt% active solids in aqueous solution
[2] Percent hydrolyzed
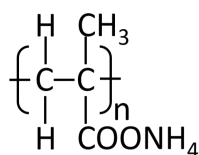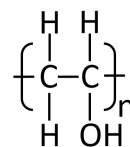
**(a)** Ammonium polymethacrylate   **(b)** Polyvinyl alcohol

Figure 3.0.1: Molecular structure of the additives used in the freeze casting slurries.

Table 3.0.2: Apparatus used for sample synthesis and characterization.

Apparatus	Model	Application
Drying cabinet	Termaks	Drying of precursor powders and samples
Long roll jar mill	U.S. Stoneware	Mixing and milling of powders
Rotary evaporator	Buchi Rotavapor R-210	Evaporation of solvent from wet powder
Hydraulic C-frame press	Compac hydraulic	Pressing of pellets for calcining and sintering
Furnace	Super kanthal	Calcination, PVA burn-out, sintering, thermal etching
Diffractometer	Bruker D8 A25 DaVinci	Analysis of purity and phase composition
Ultrasonic probe	Branson 450 digital sonifier	Mixing of slurries, breaking of agglomerates
Laser diffraction particle size analyzer	Horiba LA-960 Partica	Particle size measurements of calcined powders
Carbon coater	Cressington 208	Carbon coating before SEM analysis
Scanning electron microscope (SEM)	Zeiss Supra 55 VP field emission SEM	Examination of microstructure
Gas pycnometer	Micromeritics AccuPyc II 1340	Density measurements of calcined powders
Zeta potential analyzer	Malvern Panalytical Zetasizer Nano ZS	Measurement of zeta potential
Rheometer	Anton Paar Physica MCR 301	Viscosity measurements of slurries
Hot plate and magnetic stirrer	VWR	Dissolution of PVA in water, mixing of slurries
Freeze casting setup	In-house	Freeze casting of slurries
Freeze-dryer	Labconco FreeZone	Sublimation of ice from freeze casted samples
Grinder	Struers LaboPol-21	Grinding samples
Ultrasonic bath	VWR USC-TH	Sample cleaning
Diamond wheel saw	South Bay Technology Model 650	Cutting of samples
Archimedes setup	In-house	Porosity measurements
Gold sputter	Edwards S150B	Application of Au electrodes to samples
Piezoelectric measurement system	aixACCT TF Analyser 2000 E	Poling and piezoelectric measurements

3.1 Powder preparation

A fine ceramic powder of BCZT was prepared through a conventional solid state synthesis route by combining the precursor powders of $BaCO_3$, TiO_2, $CaCO_3$ and ZrO_2. Prior to mixing, the raw materials were dried overnight at 100°C to evaporate any water present. The powders were weighed to stoichiometric amounts, according to Equation 3.1, to yield a composition of BCZT with 10 mol% calcium and 10 mol % zirconium. This composition was chosen as it lies close enough to the morphotropic phase boundary region, see Figure 2.3.1, that it should give a relatively good piezoelectric response. At the same time, the composition will better retain its piezoelectric properties with mechanical loading, such as would be present *in vivo*, as polarization switching is more difficult than at the MPB.

$$0.9BaCO_3 + 0.1CaCO_3 + 0.9TiO_2 + 0.1ZrO_2 \rightarrow (Ba_{0.9}Ca_{0.1})(Ti_{0.9}Zr_{0.1})O_3 + CO_2 \quad (3.1)$$
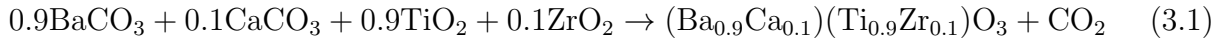
The precursors were thereafter mixed together by ball milling on a long roll jar mill (U.S. stoneware), with yttrium stabilized zirconia milling balls ($\varnothing$=5 mm) in 96% pure ethanol, for 24 hours and at a rotational speed of 205 rpm. A 250 mL plastic bottle was used to contain the materials during the milling and was first filled with approximately 50% milling balls, then topped with powder and finally covered with ethanol until 2/3 full. Subsequent to the milling, the solvent was evaporated using a rotary evaporator (Buchi Rotavapor R-210), and the dry powder was thereafter ground with an agate mortar and pestle and sieved through a mesh size of 250 μm. The powder was uniaxially pressed (Compac hydraulic C-frame press) at a pressure of 4 MPa into 25 mm diameter pellets. Each pellet consisted of on average 2.98±0.05 g of powder and had a height of 3.7±0.2 mm. The pellets were placed in a zirconia crucible, atop a layer of sacrificial powder, and also topped with sacrificial powder. The pressed powder was thereafter calcined (Super kanthal) in air at 1300 °C for 2 h, with a heating and cooling rate of 350 °C/h and 400 °C /h, respectively. A lid was placed over the crucible with a small opening, to facilitate inflow of oxygen and outflow of gases produced during calcination. The pellets were thereafter crushed and screened to 250 μm, and the calcined powder was milled, ground and sieved as previously described.

3.2 Powder characterization

3.2.1 Phase purity

The phase composition of the calcined powder was investigated by X-ray diffraction (Bruker D8 A25 DaVinci), with CuK_α radiation. Data was collected at a 2θ angular range of 20-90 °, and the time per step was 0.67 s. The results were analyzed with DIFFRAC.EVA V5.1.

3.2.2   Density

The density of the calcined powder was measured using a gas pycnometer (Micromeritics AccuPyc II 1340), with helium as the displacement gas. The powder was first dried overnight in a drying oven (Termaks) at 120 °C, and thereafter placed in a dessicator to cool to room temperature. The dried powder was transferred to the sample cup and its mass was recorded, before being put in a 100 cm^3 volume pycnometer unit fitted with a 10 cm^3 insert. The system was purged 10 times prior to the analysis. Thereafter, the density of the sample was measured until 5 consecutive cycles were within 0.05% of each other, or up to 10 times. The powder density was used to determine the mass of powder required to achieve the desired vol% solid load in the slurries for freeze casting, and the resulting values are given in Table ?? in Appendix C.

3.2.3   Particle size

The particle size distribution of the calcined powder was measured using a laser scattering particle size analyzer (Horiba LA-960 Partica). Measurements were conducted for a suspension of calcined powder in ethanol, which had been sonicated with an ultrasonic probe (Branson 450 digital sonifier)) for 30 s at 30% to break any potential agglomerates. First, a blank measurement was conducted with pure ethanol, which functioned as the solvent, to account for any background noise. The refractive index of ethanol was set to 1.360 for the analysis. The sonicated powder suspension was thereafter slowly added into the sample bath, until the transmission level for blue and red light reached 75-90%. A real refractive index of 2.40, that of barium titanate, and an imaginary refractive index of 0, as the powder was white, were applied during the measurement. A total of 3-5 measurements were conducted for each sample, to ensure the data was reproducible, and each measurement consisted of 10000 light scattering data calculations. The data was transformed to and analyzed as a number distribution, as this gave a better indication of the median particle size when compared to SEM images of the powders. The SEM analysis of the calcined BCZT was conducted using a LVFESEM (Zeis Supra 55 VP). The sonicated powder and ethanol suspension was dropped onto a conductive carbon tab attached to a SEM pin stud. The ethanol was then left to evaporate at room temperature. The powders were, finally, coated with carbon (Cressington 208) prior to analysis.

The aim of the particle size analysis was to ensure that a unimodal particle size distribution had been achieved during powder preparation and that the particle size did not change much from batch to batch. This is due to the fact that the particle size of the solid load for freeze casting will affect the formation of the final structure, and it was not intended to investigate this parameter. BCZT batch 3 did not have the same size distribution or mean size as the two previous batches, and was therefore milled for an additional 12 hours, in the same way as described in Section 3.1. Although the particle size was still not the same after the second milling step, it was considered adequate, and the powder was not milled further.

3.3 Slurry formation

The slurries for freeze casting were prepared by combining the calcined BCZT powder with deionized water, Darvan C-N and PVA, which functioned as the solid load, freezing vehicle, dispersant and binder, respectively. The amount of each component and the method of mixing them changed from sample to sample, as the slurry composition and preparation method were optimized. A full list of the slurry compositions and mixing methods and times for the freeze cast structures is given in Table 3.3.1. The solid load was first set to 25 vol%, which lies within the range commonly applied to produce macroporous structures [57], but was reduced down to 15 vol% from freeze casting #3, as a lower solid load should give a higher porosity. The initial amount of dispersant added in the first few slurries was determined from the sedimentation test described in Section 3.4.1. The quantity was subsequently increased in freeze castings #4 and #5, based on the resulting structures from freezing of the slurries. The amount of PVA added to every slurry following freeze casting #1 was based on the PVA test presented in Section 3.4.2.

Table 3.3.1: Slurry composition and mixing optimization scheme. Freeze casting #5 shows the optimized composition and mixing routine achieved in this study.

Freeze casting #	Slurry composition				Mixing method and time
	BCZT [vol%]	Deionized water [vol%]	Darvan C-N [wt%][1]	PVA [wt%][1]	
1	25	75	1.5	-	Ultrasonic finger, 2 min
2	15	85	1.5	1	Ultrasonic finger, 10 min
3	20	80	1.5	1	Ultrasonic finger, 10 min
4	15	85	3	1	Magnetic stirrer, 2 hrs
5	15	85	5	1	Magnetic stirrer, 3 hrs

[1] Given as wt% of BCZT powder

The first 3 slurries were made by mixing all components together with an ultrasonic probe (Branson 450 digital sonifier). To start, the PVA was dispersed in the BCZT powder by grinding in acetone with a pestle and mortar, until full evaporation of the acetone. The powder mixture was thereafter added to water and Darvan C-N before sonicating for up to 10 minutes at 70 %. The sonication process was not sufficient to achieve a homogeneous suspension and the slurries were subsequently hand-mixed until visibly blended. In addition, because PVA does not dissolve well in acetone, it was thus presumably not properly incorporated into the final slurry. To improve mixing of the remaining slurries, the setup was therefore changed and a magnetic stirrer (VWR) was favourably utilized. Firstly, the PVA was dissolved in one part of the deionized water by mixing with a magnetic stirrer at elevated temperatures (below 100 °C to minimize evaporation of water). This ensured full dissolution of the PVA. The mixture was thereafter cooled before incorporating the Darvan C-N for

approximately 5 minutes. Finally, the BCZT powder and remaining water were added, and the whole slurry was stirred for up to 3 hours. This was the optimized slurry preparation route achieved. During mixing, the slurry was covered with parafilm to reduce evaporation of the solvent.

3.4   Slurry optimization

3.4.1   Sedimentation test

Before any slurries were prepared, a test was conducted to see how stable the calcined BCZT powder was in water. It was determined that the powder should remain well dispersed, and not significantly sediment, for at least 4 hours, as this was determined to be a sufficient amount of time to complete a full freeze casting cycle. Otherwise, sedimentation of the slurry during freezing would result in unfavorable variations of density, porosity and microstructure throughout the resulting sample. A suspension of 0.5 wt% BCZT powder in deionized water was prepared by mixing with an ultrasonic probe (Branson 450 digital sonifier) for 2 min at 30 %. The mixture was transferred to a 10 mL graduated cylinder and covered with parafilm to avoid evaporation of water during the test. The suspension was monitored incrementally and the degree of particle sedimentation was determined by measuring the location of the interface between the supernatant and suspension over time. As the mixture of BCZT powder and water significantly sedimented within 1 min, a form of stabilization was required. The same test was therefore conducted for a slurry consisting of 0.5 wt% BCZT powder and 1.5 wt% Darvan C-N (based on the BCZT content), in deionized water. The amount of dispersant used for the initial test was chosen according to the work of *Jean & Wang*, which showed that it was sufficient to achieve stabilization of aqueous barium titanate suspensions [55]. As Darvan C-N is a water-based solution with 25 wt% active solids, the amount of ammonium polymethacrylate in the suspension was approximately 0.38 wt%. The suspension was periodically checked until a total of 4 hours had passed. The sedimentation test was only carried out for powder Batch 1.

3.4.2   The use of an organic binder

The resulting green body from freeze casting #1 was overly fragile, and it was thereby clear that a binder should be to added to the slurry composition. The effect of an organic binder on the stability and mechanical strength of a freeze dried green body was therefore tested with barium titanate powder, in order to spare the use of the calcined BCZT. It was assumed that the two material systems should be comparable in this case. The barium titanate powder used in the experiment was prepared in the way described by Fedje [81]. Two slurries consisting of 25 vol% barium titanate powder and 1.5 wt% Darvan C-N (based on the amount of powder) in deionized water were made by mixing with an ultrasonic probe

(Branson 450 digital sonifier), as described in Section 3.3. One of the slurries also contained 1 wt% PVA, which was mixed together with the powder in acetone, following the method given in Section 3.3, prior to sonication. The amount of binder was chosen based on similar studies [8,20]. Both slurries were degassed, freeze cast (with a cooling rate of 5 °C/min) and freeze dried as outlined in Section 3.5.1. The freeze dried samples were thereafter examined by eye and carefully handled to check for mechanical stability and how easily they might break.

3.4.3 Zeta potential

In order to gain more insight into the stabilization mechanism of the ammonium polymethacrylate dispersant in the BCZT slurries, zeta potential measurements were conducted. Mixtures containing 0.1 mg of powder in 3 mL deionized water were prepared by mixing with an ultrasonic probe (Branson 450 digital sonifier) for 30 sec at 30 %. Four different compositions were made, containing 0, 1.5, 3 and 5 wt% of Darvan C-N, meaning 0, 0.38, 0.75 and 1.25 wt% of ammonium polymethacrylate. Zeta potential analysis (Malvern Panalytical Zetasizer Nano ZS) of the mixtures was thereafter performed.

3.4.4 Viscosity

As the viscosity of the slurry is a parameter that greatly influences the formation of the freeze cast structure, the viscosity of two different slurry compositions was measured with a rheometer (Anton Paar Physica MCR 301) in rotational mode. The two slurries had the compositions of freeze casting #2 and #5 given in Table 3.3.1. Both slurries were prepared using the same optimized routine of mixing with a magnetic stirrer for a total of 3 hours, as detailed in Section 3.3. The viscosity test was run with a plate on plate (5 cm diameter) measuring geometry and the gap between the plates was set to 170 μm. Measurements were conducted at 25 °C. The shear rate was first ramped down from 1000-0.001 1/s and then ramped up from 0.001-1000 1/s, both varied logarithmically. A total of 120 viscosity measurements were taken for each slurry and the time per measuring point was 10 s.

3.5 Solid sample processing

3.5.1 Freeze casting

After mixing, the prepared slurry was poured into a PTFE mold (10 mm diameter) fitted with a copper base, and placed in a vacuum desiccator connected to a vacuum pump (Buchi V-700). The slurry was degassed under partial vacuum ($\sim$ 20 mbar) for approximately 20

minutes to remove any air bubbles introduced during mixing. Thereafter, the mold was transported to an in-house made one-sided cooling setup, shown in Figure 3.5.1, and cooled with liquid nitrogen. The cooling rate was controlled by a ring heater, thermocouple and temperature controller. A cooling rate of 5 °C/min was used for all samples made during the optimization of the slurry, meaning all freeze castings listed in Table 3.3.1. In addition, a set of samples with different cooling rates of 1, 5 and 10 °C/min were frozen, to investigate the affect of freezing rate on the resulting porous structure. All of these samples were made with the optimized slurry composition and mixing routine listed as freeze casting #5 in Table 3.3.1. The sample was left in the cooling setup until completely frozen, which was between 20-60 minutes depending on slurry composition and cooling rate. Once frozen, the sample was removed from the mold and placed overnight in a freeze dryer (Labconco FreeZone), at a temperature < -50 °C and pressure < 5 mbar.
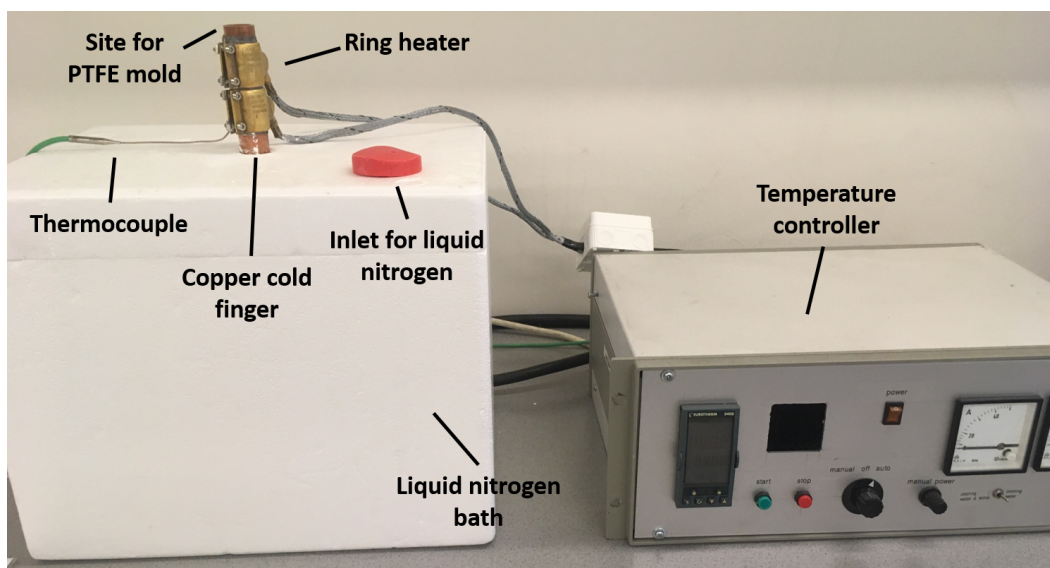
Figure 3.5.1: In-house made freezing setup, labelled with important components.

3.5.2   Preparation of dense reference samples

Dense samples were processed by uniaxial pressing (Compac hydraulic C-frame press) of the calcined powder into cylindrical disks (10 mm diameter), at a pressure of 100 MPa. Each pellet consisted of on average 0.510 ±0.008 g of powder and had a height of 2.16±0.03 mm. The dense samples were used as a reference point for the piezoelectric measurements, to determine the effect of the lamellar pores

3.5.3 Sintering

The freeze dried samples were placed in an alumina crucible, over a layer of sacrificial powder. The PVA was burnt out (Super kanthal) by heating to 500 °C for 8 hours, with a heating rate of 100 °C/h. Samples were thereafter sintered (Super kanthal) at 1450 °C for 3 hours, with a heating and cooling rate of 350 °C/h and 400 °C/h, respectively. Dense samples were sintered in the same way, but did not undergo the burn-out step as no organic binder was present. The full temperature program is given in Figure 3.5.2.
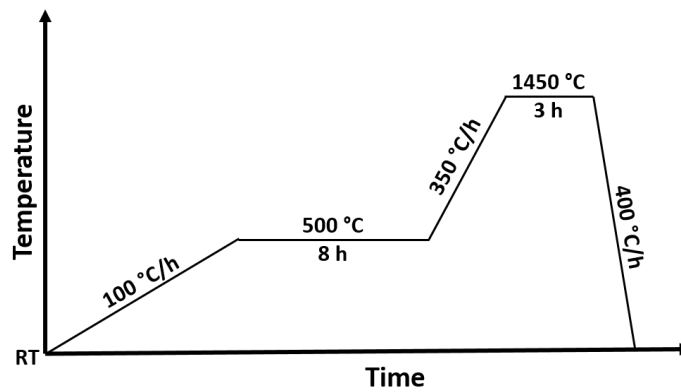
Figure 3.5.2: The PVA burn-out and sintering program used for the freeze dried samples. Dense samples were only sintered, as no PVA was present.

3.6 Sample characterization

3.6.1 Phase purity

The phase composition of a crushed, sintered, freeze cast sample and sintered, dense sample was measured in the same way as for the calcined powders, described in Section 3.2.1. The dense sample was ground to 1200 grid with SiC-paper prior to the analysis to avoid any anomalous surface features.

3.6.2 Microstructure

The porous structures of the freeze cast samples were examined with a SEM (Zeiss Supra 55 VP LVFESEM). Both the cross sections and top surfaces perpendicular and parallel, respectively, to the freezing direction were investigated. The directions relative to the freezing direction are illustrated in Figure 3.6.1. To reveal the cross sections, samples were first cut using a low speed diamond wheel saw (South Bay Technology Model 650) with a diamond

metal bonded wafering blade (Allied high tech products Inc., thickness 150 μm), as illustrated in Figure 3.6.2. Prior to analysis, all samples were also ground to 1200 grid with SiC-paper to ensure an even and smooth surface. The samples were thereafter cleaned with ethanol in an ultrasonic bath (VWR USC-TH) for 10 min, to remove any impurities from the grinding process. Finally, the samples were coated with carbon (Cressington 208).

The grain microstructure of the freeze cast samples with the optimized slurry composition and a dense pressed sample were also investigated using a SEM. In preparation for imaging, the samples were polished to a 3 μm finish with DiaPro Dac-3, a diamond suspension, and thereafter thermally etched (Super kanthal) for 5 min at 1350 °C, with a heating and cooling rate of 200 °C/min, in order to expose the grain boundaries. A carbon coating (Cressington 208) was subsequently applied before analysis. The grain size was qualitatively investigated both parallel and perpendicular to the freezing direction.
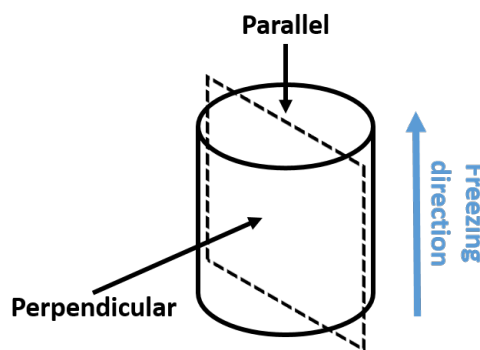
Figure 3.6.1: Indication of the parallel and perpendicular directions, relative to the freezing direction, used for SEM analysis.

3.6.3   Porosity

Samples for piezoelectric characterization were cut from the freeze cast structures with a low speed diamond wheel saw (South Bay Technology Model 650). A total of 3 pieces were cut from each freeze cast structure made with the optimized slurry composition, illustrated by the grey regions in Figure 3.6.2. Samples were not taken from the bottom portion of the structure, shown in red in Figure 3.6.2, as it does not display the lamellar porous structure of interest (see Section 4.2.5). The density of these pieces and also the dense pressed samples was measured using Archimedes method, with isopropanol as the immersion liquid. The total-, open- and closed porosity of the samples were calculated according to the equations given in Appendix C. As the size of the samples cut from the freeze cast structures were smaller than that recommended, 50 cm^3, to achieve reliable values with Archimedes method, a level of uncertainty is expected. The same density measurement and porosity calculation was therefore preformed 3 times for each sample, to achieve a more representative statistical value. The density and porosities of each sample is therefore given as the average of all single

measurements, and the error is the minimum and maximum value recorded. For the dense samples, only one measurement was conducted for each piece, and the reported density- and porosity value is the average over all dense samples, with the error given as the minimum and maximum value observed out of all the dense samples.
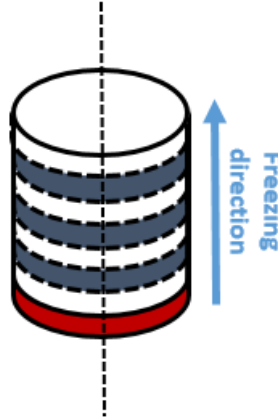

Figure 3.6.2: Schematic of the cutting routine used to produce samples for piezoelectric characterization from the freeze cast structures (the grey sections). Samples were not taken from the portion of the structure that was frozen first during freeze casting, because it does not exhibit the lamellar porous structure (red zone). The dashed line shows how the samples were cut in order to examine the cross section perpendicular to the freezing direction with a SEM. The freezing direction is as indicated.

3.6.4 Piezoelectric properties

In preparation for piezoelectric characterization, the samples were ground with 1200 grit SiC-paper to ensure a flat surface and even thickness of the piece. Impurities from the grinding process were removed by cleaning the samples with ethanol in an ultrasonic bath (VWR USC-TH) for 10 min. Gold electrodes were applied by sputtering for 60 sec (Edwards S150B), so that the samples became conductive. The samples were first poled (aixACCT TF Analyzer 2000) in air at an electric field of 5 kV/cm. Polarization and strain loops were taken by applying a bipolar triangular waveform with a frequency of 1 Hz. The remnant piezoelectric coefficient, d_{33}^0, was measured (aixACCT TF Analyzer 2000) using a small signal frequency and amplitude of 1 kHz and 3 V, respectively. A total of 100 data points were taken in each cycle and a long integration time was employed in order to give a more accurate reading. Only the d_{33}^0 was measured as this is the value that would be relevant upon implantation of the material, where no electric field is applied. All piezoelectric measurements were conducted parallel to the freezing direction, as this should give the best properties.

Chapter 4

Results

4.1 Powder characterization

4.1.1 Phase purity

A total of 3 batches of BCZT powder were prepared and their phase purity was analyzed through x-ray diffraction. The x-ray diffractogram for the first batch is given in Figure 4.1.1, together with the characteristics peaks for the BCZT composition with 10 mol% calcium and 10 mol% zirconium, marked with black squares. As no secondary phases were present, the calcined powder was phase pure. The small peak located at a 2Θ of approximately 28°, marked with an asterisk, is background noise from Cu Kβ1 radiation from the XRD measurement. Corresponding XRD patterns for the other powder batches can be found in Appendix A.
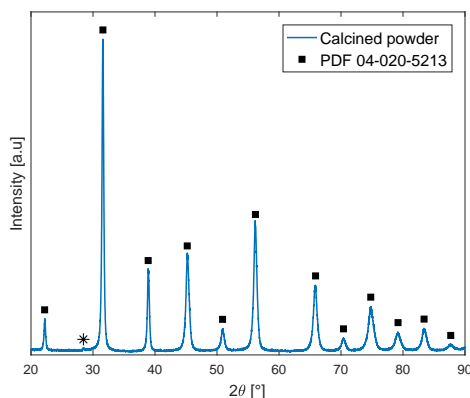
Figure 4.1.1: The XRD pattern of the first batch of calcined powder. Peaks are matched to the reference diffractogram, PDF 04-020-5213, marked with black squares, revealing phase pure BCZT. The asterisk marks background noise from the XRD measurements.

41

4.1.2   Particle size

The particle size distributions of the calcined BCZT powders were measured using a laser scattering particle size analyzer. The resulting distribution for Batch 1 and 3 are shown in Figure 4.1.2. All powder batches displayed a unimodal size distribution as desired. Powder Batch 3 was milled twice after calcining, as the size distribution was different than that for Batch 1 and 2 after only a single milling step. Figure 4.1.2 shows the distributions after both milling cycles, and although the final distribution was still unlike that for the other batches, it was deemed acceptable and no new milling steps were preformed. The particle size distributions for all batches are shown in Appendix B. The median particle size for each batch, calculated from the distributions, is given in Table 4.1.1.
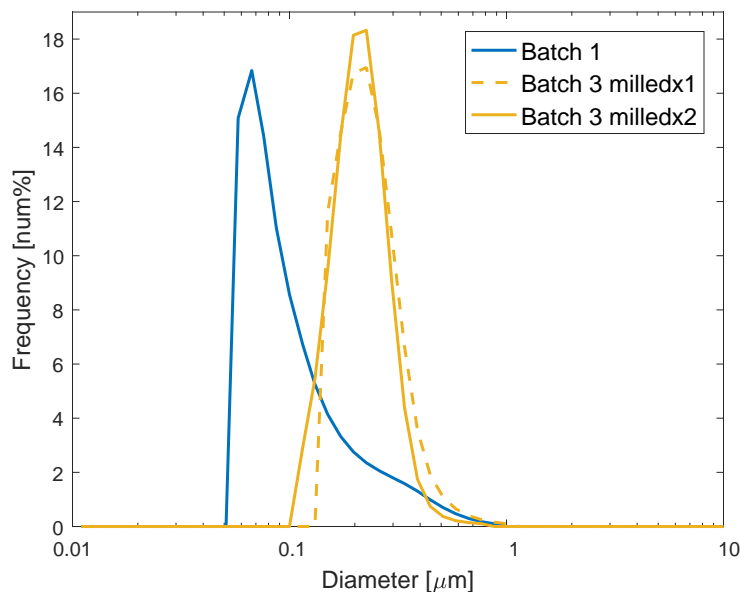
Figure 4.1.2: The particle size distribution for Batch 1 and 3, after 1 and 2 milling steps. Both powders showed a unimodal size distribution.

Table 4.1.1: The median particle size for each batch of calcined BCZT. The value given for Batch 3 is after the second milling step.

Powder batch	Median particle size [nm]
1	80
2	83
3	197

The powders were also examined with a SEM. Figure 4.1.3 shows an image for Batch 1, which clearly indicates that the particles have a size below 1 μm, in agreement with the particle size distribution. SEM images for the remaining powders can be found in Appendix B.

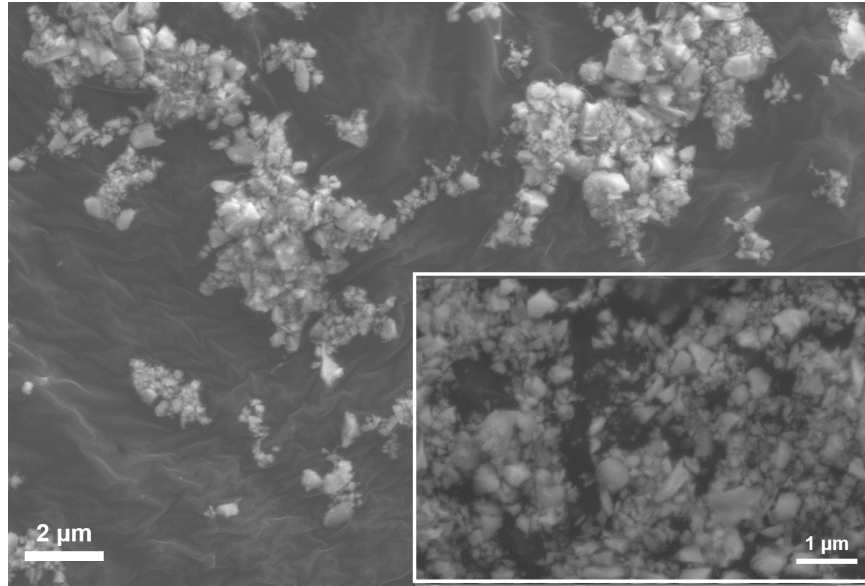**Figure 4.1.3:** SEM image of Batch 1 of the calcined BCZT powder, which verifies a particle size below 1 μm.

4.2 Slurry optimization

Several freeze casting trials, characterized in Table 3.3.1, were performed before reaching the optimized slurry composition and mixing routine. In the following sections, the entire optimization process will be outlined step by step, including explanations for the modifications made from one slurry to the next, and the characteristics of the structures achieved from freeze casting of each slurry.

4.2.1 Step 1: Sedimentation test

Before any freeze casting slurries were prepared, a sedimentation test was conducted to determine the behavior of the prepared BCZT powder in water. A combination of simply BCZT and water resulted in instantaneous sedimentation of the powder, as a thin layer of sediment, 2% of the suspension height, was visible after just 1 minute. The same test was, therefore, conducted with the addition of an ammonium polymethacrylate dispersant (Darvan C-N). 1.5 wt% of dispersant, based on the mass of BCZT powder, was added, and as Darvan C-N is a water-based suspension with 25 wt% active solids, this corresponds to approximately 0.4 wt% of ammonium polymethacrylate. The suspension with dispersant, shown in Figure 4.2.1, appeared stable and did not sediment for the prescribed 4 hours. The quantity of dispersant trialed in the sedimentation test served as a starting point for the amount required in the slurries for freeze casting.

Figure 4.2.1: Image of the stable BCZT aqueous suspension from the sedimentation test, 5 hours after mixing, achieved by the addition of an ammonium polymethacrylate dispersant.

4.2.2   Step 2: The first freeze casting attempt

An initial freeze casting, denoted as freeze casting #1 in Table 3.3.1, was conducted for a slurry consisting of 25 vol% powder, 75 vol% deionized water and, based on the results from the sedimentation test, 1.5 wt% Darvan C-N. The slurry was frozen with a cooling rate of 5 °C/min. The resulting green body, after sublimation of the ice, was overly fragile, as it was difficult to handle without breaking. The green body also cracked during the drying stage, as shown in Figure 4.2.2, and it was for these reasons clear that a binder was required to stabilize the structure. The effect of an organic binder on the mechanical strength of the green body was tested, and the results are presented in Section 4.2.3.

Figure 4.2.2: Image of the partially broken green body after sublimation of the ice in the initial freeze casting.

The target lamellar structure was furthermore not visible in the first freeze cast sample after sintering. SEM images taken perpendicular to the freezing direction revealed that the structure consisted of relatively dense regions at the top and bottom of the piece and irregular shaped pores at the center, as shown in Figures 4.2.3a and 4.2.3b, respectively. The microstructure given in Figure 4.2.3a is classified as dense here, as it has a relatively low amount of porosity compared to the other parts, although it should be made clear that these regions are evidently not completely dense.

(a)   (b)
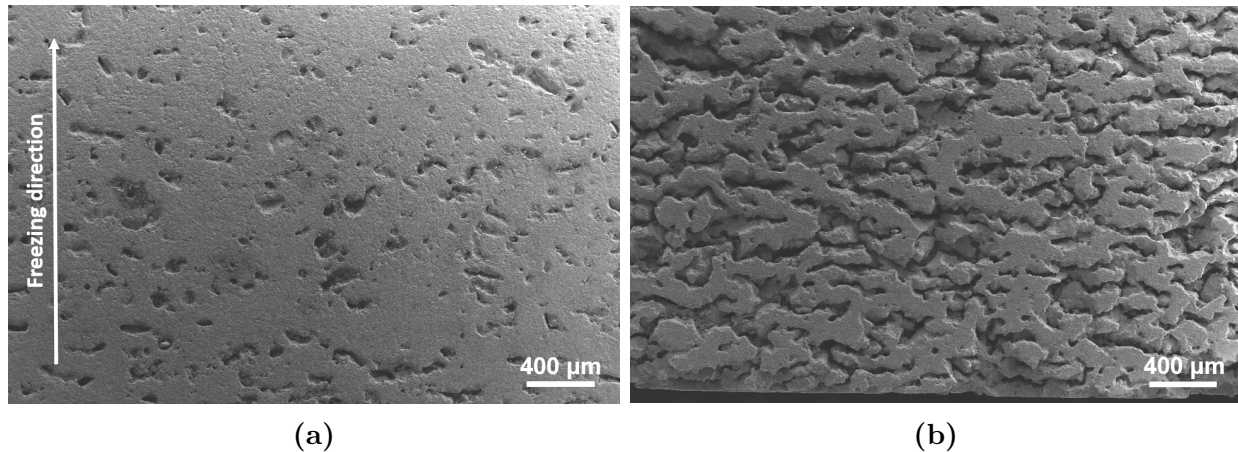
Figure 4.2.3: SEM images of the first freeze cast sample, displaying relatively dense areas (a) and regions with irregular and unoriented pores (b), but no lamellar structure.

4.2.3   Step 3: The use of an organic binder

The effect of the organic binder PVA on the stability of the dry green bodies made from freeze casting of barium titanate slurries was tested. As indicated in Figure 4.2.4a, the sample without PVA was very brittle and broke upon careful handling. Figure 4.2.4b on the other hand shows that including 1 wt% PVA in the slurry made it possible to handle the sample, and the green body was also stable and did not collapse during the drying stage. Since these were the requirements of the stability of the green body, the addition of 1 wt% PVA was therefore a sufficient amount of binder. Based on this result, 1 wt% PVA was added to every following freeze casting slurry.
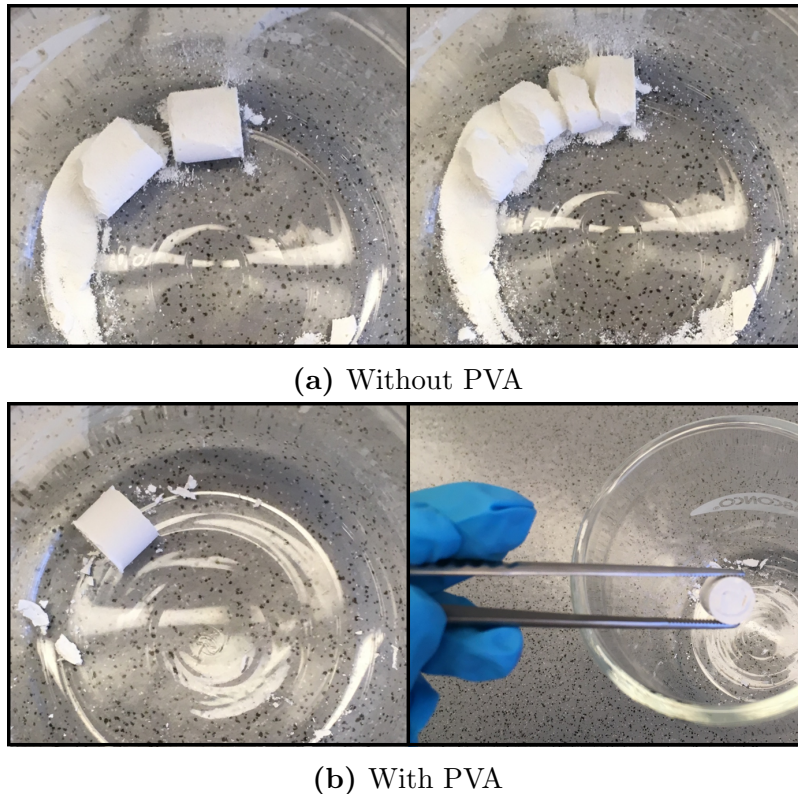
(a) Without PVA

(b) With PVA

Figure 4.2.4: Images of the resulting dry green bodies from the organic binder test. The sample without PVA (a) exhibited a brittle structure, making it difficult to handle and avoid breakage during sublimation. The addition of 1 wt% PVA gave a sufficiently stable green body (b).

4.2.4 Step 4: Avoiding sedimentation

In the next two freeze castings, labelled #2 and #3 in Table 3.3.1, 1 wt% PVA was added to the slurries and the solid load was reduced to 15 vol% and 20 vol%, respectively. It was of interest to try different solid loads, to assess whether this would affect the final microstructure, compared to the initial freeze cast sample. The amount of dispersant was unchanged. The resulting sample made with 15 vol% BCZT after sintering is shown in Figure 4.2.5a. The structure displayed an inconsistent diameter, being thinner at the top (the portion that is frozen last) and wider at the bottom. It was presumed that the irregular shape indicated significant sedimentation of the slurry during preparation and freezing, which will be described in more detail in Section 5.1.2. As marked in Figure 4.2.5a, the sample displayed a microstructural gradient, consisting of relatively dense regions and regions with irregular pores, imaged perpendicular to the freezing direction in Figure 4.2.5b. This was similar to that observed for the first freeze cast structure. However, unlike the first freeze cast sample, a section with the characteristic lamellar pores was present at the top of the sample, shown in the SEM image taken perpendicular to the freezing direction in Figure 4.2.5c. This demonstrated that the ice-templating process was indeed occurring for the slurry, in the sense that the segregation of the ice and the powder particles during freezing

lead to the formation of lamellar macropores. It was thereby expected that if sedimentation were avoided, the whole structure would adopt the lamellar architecture. Sedimentation also occurred for the sample with 20 vol% of powder, which can be seen in Appendix D. As the slurry made with 15 vol% powder resulted in a sufficiently strong green body after freezing and sublimation, it was determined that this solid load should be applied in all the following freeze castings, considering that a lower solid load should result in a higher porosity. Nevertheless, it is important to keep in mind that the amount of porosity, and therefore the solid load, will also have an impact on the mechanical properties of the freeze cast structure. Further experimentation is therefore required to determine what solid load would strike the most favorable balance between these parameters.
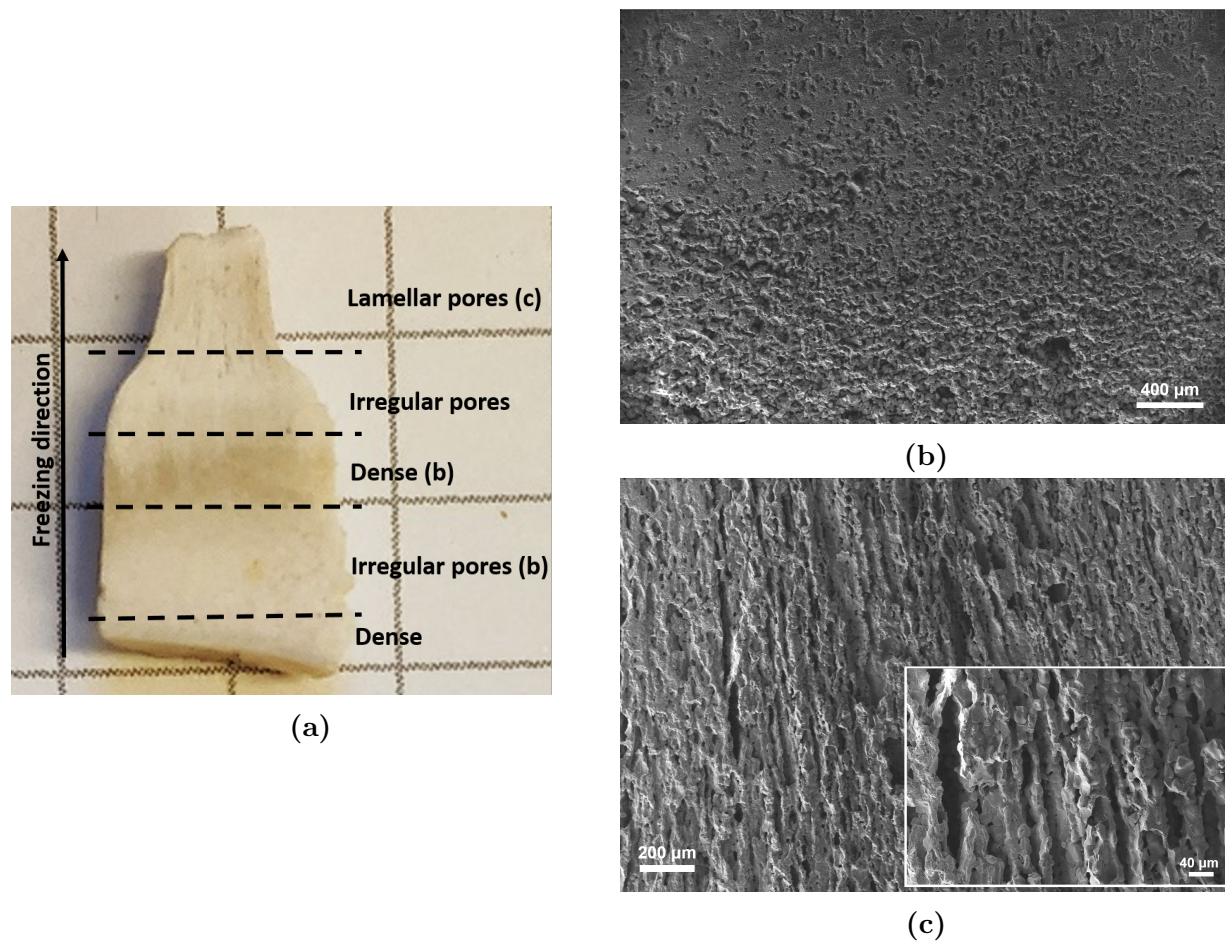
Figure 4.2.5: (a) The resulting structure after sintering from freeze casting #2 (see Table 3.3.1), of a slurry with 15 vol% BCZT powder, labelled according to the microstructure found in each portion of the sample. (b) A SEM image of the dense and irregular porous regions. (c) A SEM image of the lamellar porous structure located at the top of the sample, with an insert showing the porous channels at a higher magnification. The labels in figure (a) indicate what portion of the sample the SEM images were taken of. All SEM images were taken perpendicular to the freezing direction.

In light of these results, the amount of dispersant was increased to 3 wt% in freeze casting #4 (see Table 3.3.1), with the aim of avoiding sedimentation. Freezing of this slurry produced a structure that was similar in shape to that of freeze casting #3, with a corresponding microstructural gradient. SEM images of the different structural regions taken perpendicular to the freezing direction are shown in Appendix D. A SEM image of the top surface of the sample, taken parallel to the freezing direction, is shown in Figure 4.2.6, revealing a large amount of open lamellar pores.
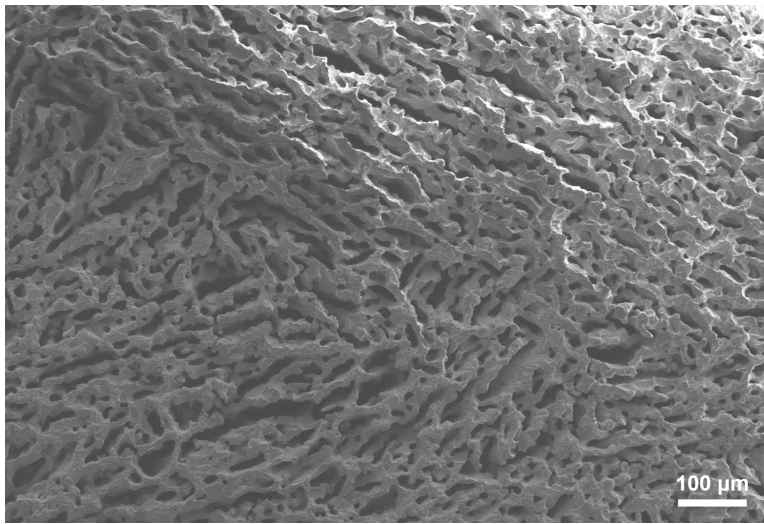
Figure 4.2.6: SEM image of the top surface, taken parallel to the freezing direction, of the sample made with 3 wt% dispersant, labelled as freeze casting #4 in Table 3.3.1, displaying an open porous structure.

As sedimentation still occurred at a considerable rate for the slurry containing 3 wt% Darvan C-N, the amount of dispersant was further increased to 5 wt% in freeze casting #5, see Table 3.3.1. The resulting structure after sintering had an even diameter throughout the full length of the sample, signifying that the sedimentation velocity was low enough that significant sedimentation did not occur within the slurry preparation and freezing time. This indicated that an increase in the concentration of Darvan C-N gave increased slurry stability. Such a result is somewhat expected, as 5 wt% of Darvan C-N contains 1.25 wt% of active ammonium polymethacrylate dispersant, which according to the literature lies within the quantity range commonly applied to stabilize ceramic slurries for freeze casting [8, 19, 20, 48, 62]. However, due to the fact that this sample was quite difficult to remove from the PTFE mold after freezing, the ice partially melted before the sample was put in the freeze dryer. Because melting will have an effect on the final structure, it was consequently presumed that this sample did not display a representative microstructure. SEM images from this freeze casting can be found in Appendix D. The same slurry composition was therefore prepared and freeze cast again, and the results are described below.

4.2.5 Step 5: The optimized slurry composition

A second slurry consisting of 15 vol% BCZT powder, 85 vol% deionized water, 5 wt% Darvan C-N and 1 wt% PVA, the composition of freeze casting #5 in Table 3.3.1, was prepared and freeze cast. The resulting structure had an even diameter, indicating that sedimentation did not occur to a considerable degree, as expected from the results of the previous freeze casting. The sample also exhibited the desired lamellar microstructure, and a successful freeze casting had thus been achieved. Examination of the cross section of the sample perpendicular to the freezing direction uncovered a microstructural gradient at the bottom of the sample, as shown in Figure 4.2.7a. Three distinct zones can be distinguished, a dense bottom layer, a portion with unoriented and poorly interconnected pores and finally the lamellar structure, which stretched throughout the remaining length of the sample. The length of the gradient was relatively small, compared to the length of the sample, at 0.8 mm. Such a transition region is a common feature of freeze cast structures [19, 49, 62]. Figure 4.2.7b shows a SEM image of the cross section at a higher magnification, which demonstrates the lamellar shape of the pores in more detail. The lamellar organization is not always easy to ascertain perpendicular to the freezing direction, as the orientation of the pores where the cut is made is arbitrary.
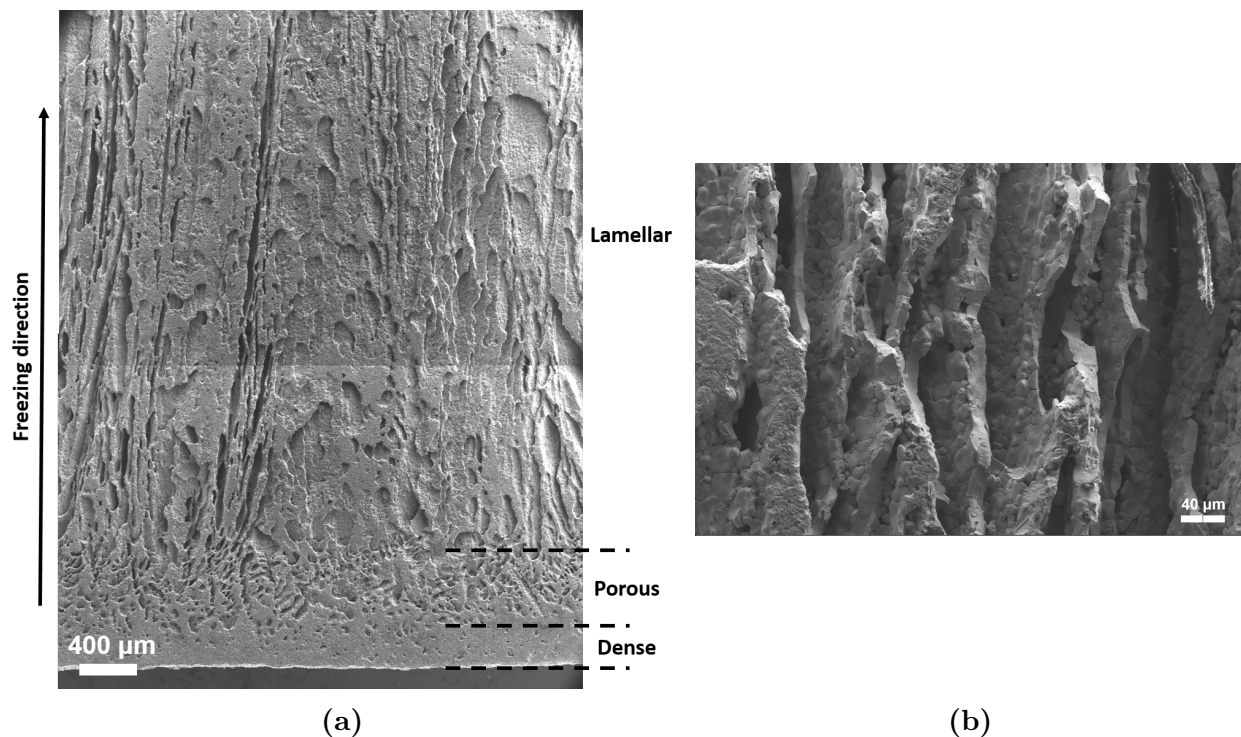

(a)   (b)

Figure 4.2.7: (a) A SEM image of the cross section of the freeze cast sample made with the optimized slurry composition, marked with three microstructural zones. (b) A SEM image with a close-up view of the lamellar pores. Both images were taken perpendicular to the freezing direction.

Figure 4.2.8 shows SEM images of the freeze cast sample taken parallel to the freezing direction, displaying open and interconnected pores with a lamellar shape. Qualitative

analysis determined that the length of the pores were on average around 200 μm, but pores as small as 100 μm and as large as 780 μm could also be seen. The width of the pores lied between approximately 30-50 μm. The lamellar pores also exhibited a surface roughness, which is a common feature of freeze cast structures **??**.
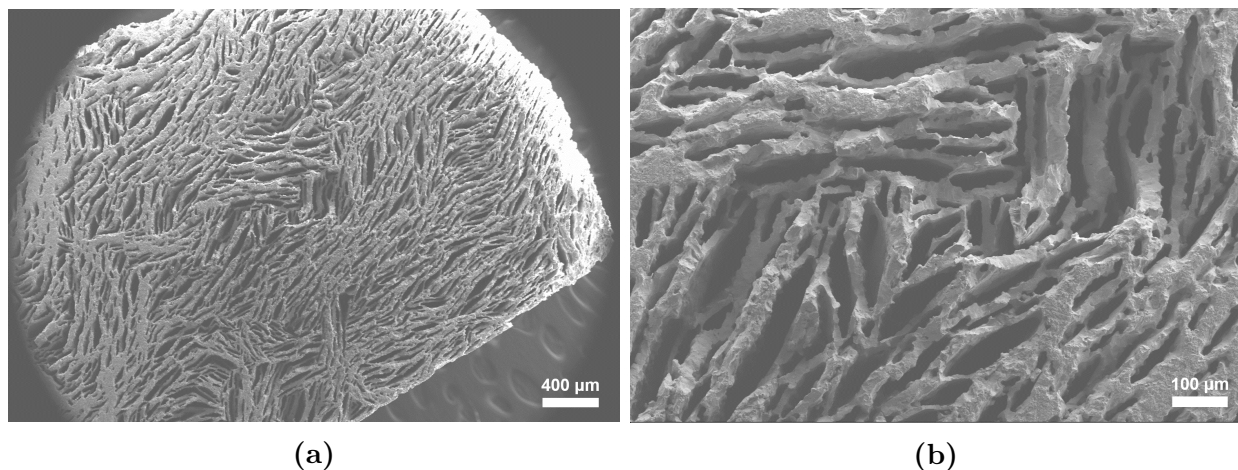

| (a) | (b) |

Figure 4.2.8: SEM images of the top surface of the freeze cast sample made with the optimized slurry composition, taken parallel to the freezing direction, displaying open and interconnected lamellar pores.

As this slurry composition produced a freeze cast sample with an overall lamellar microstructure, it was determined that no further optimization should be conducted. The slurry consisting of 15 vol% BCZT powder, 85 vol% deionized water, 5 wt% Darvan C-N and 1 wt% PVA was therefore the optimized composition achieved in this study, and was applied in all the following freeze castings.

4.2.6   Zeta potential

As a start to gaining an understanding of the stabilizing effect of the ammonium polymethacrylate dispersant in the BCZT suspensions, the zeta potential of suspensions containing every amount of Darvan C-N trialed in the freeze casting slurries was measured. The zeta potential of a suspension without dispersant, meaning only BCZT powder and water, was also tested. The results are given in Table 4.2.1. Three consecutive measurements were conducted for each suspension and the reported value is the average of these, with the standard deviation given as the error. The zeta potential of the suspensions with dispersant is higher at all concentrations than the suspension without dispersant, indicating that ammonium polymethacrylate performs a stabilizing function in the suspension. The zeta potential is highest for the suspension with 1.5 wt% Darvan C-N.

Table 4.2.1: The zeta potential of suspensions containing every trialed amount of Darvan C-N, 1.5, 3 and 5 wt%, in the freeze casting slurries during the optimization process, in addition to a suspension with no Darvan C-N.

Darvan C-N [wt%]	Zeta potentail [mV]
0	-35.8±0.3
1.5	-52.9±0.2
3	-44.7±0.6
5	-49.1±0.5

4.2.7   Viscosity

The viscosity of two different slurry compositions was measured and the results are displayed in Figure 4.2.9. Both slurries demonstrated a shear thinning behavior, as the viscosity decreases with increasing shear rate. The viscosity of the slurry with 1.5 wt% Darvan C-N was higher than that of the slurry with 5 wt% Darvan C-N for all shear rates. The slurry with 1.5 wt% also demonstrated a relatively large hysteresis between the shear rate up and shear rate down modes, indicated by the arrows in Figure 4.2.9.
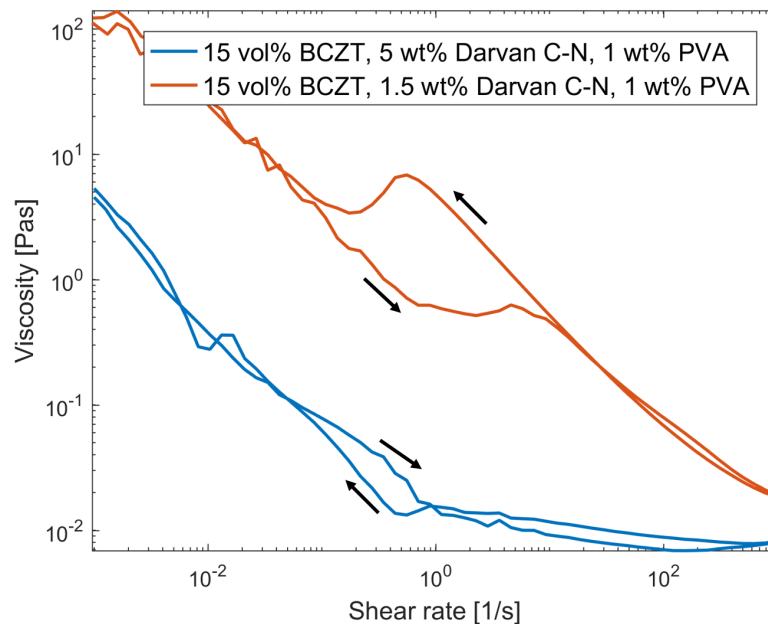
Figure 4.2.9: The viscosity of two different slurry compositions as a function of shear rate. The arrows mark the curves corresponding to the shear rate being ramped up and down.

4.3 Sample characterization

4.3.1 Phase purity

The phase purity of a crushed, freeze cast sample and polished, dense sample was examined using x-ray diffraction. The resulting XRD patterns, shown in Figure 4.3.1, were fitted to the reference peaks of BCZT with 10 mol% Ca and 10 mol% Zr, marked with black squares, revealing that both samples were phase pure. The asterisk in Figure 4.3.1 marks the contribution from Cu Kβ1 from the XRD measurement. The diffraction peaks of the sintered samples are sharper than that of the calcined powder, shown in Figure 4.1.1, due to the increase in crystallinity with sintering. The shape of the psuedocubic (200), (220) and (222) peaks at a 2Θ of about 45°, 65° and 83°, respectively, shown in more detail in Figures 4.3.1b and 4.3.1c, indicate a rhombohedral phase, according to the work of *Zhou et al.* [80]. This is also in agreement with the phase diagram shown in Figure 2.3.1.
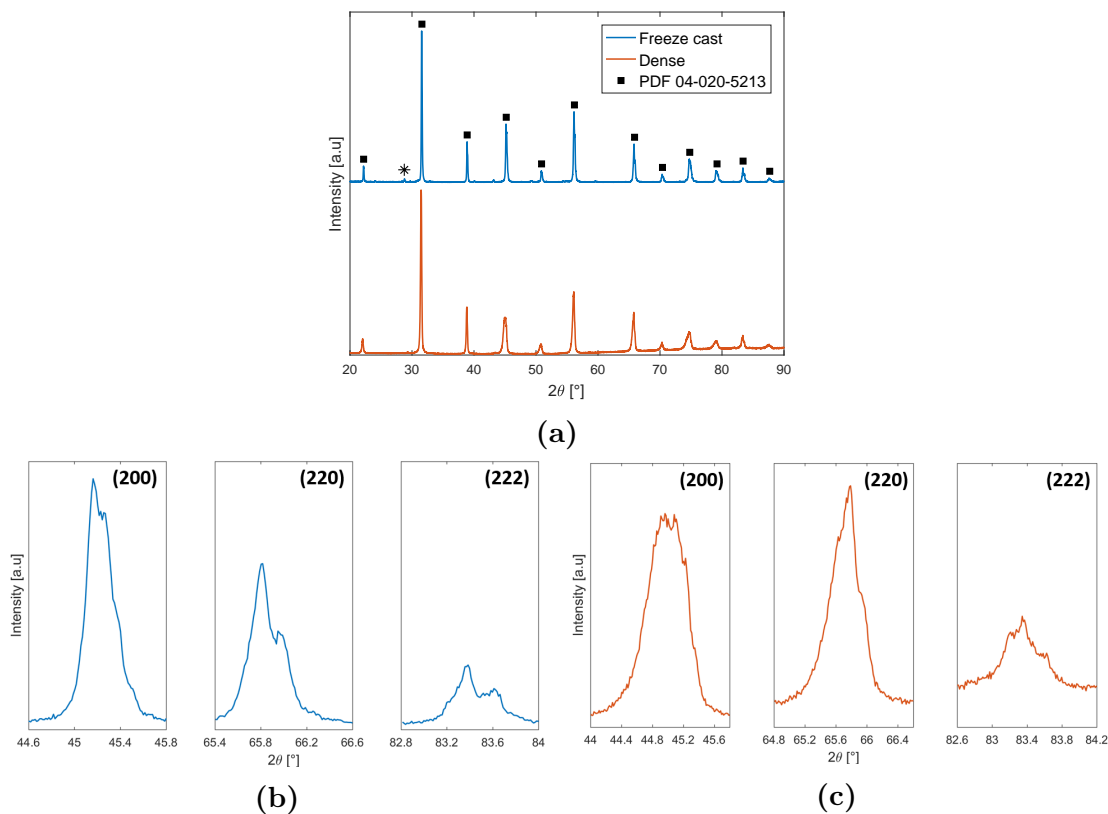

Figure 4.3.1: The x-ray diffractogram for a sintered freeze cast sample and sintered dense sample, matched to the reference pattern of BCZT, PDF 04-020-5213, used for the phase purity analysis. The asterisk marks background noise from the XRD measurements (a). A magnified view of the pseudocubic (200), (220) and (222) peaks, marked accordingly, for the freeze cast (b) and dense (c) sample.

4.3.2 The effect of cooling rate

In order to test the effect of the applied cooling rate during freeze casting on the resulting lamellar structure, and specifically the size of the porous channels, different freezing rates were trialed. Three slurries were prepared with the same optimized slurry composition and preparation route, achieved through the optimization process described in Section 4.2, and frozen with a cooling rate of 1, 5 and 10 °C/min. Figures 4.3.2a, 4.3.2b and 4.3.2c show SEM images of the cross sections of the resulting samples, taken perpendicular to the freezing direction, with corresponding images at higher magnification given in Figures 4.3.2d, 4.3.2e and 4.3.2f. Every sample displayed the initial microstructural gradient described in Section 4.2.5. However, the transition regions had a length of approximately 1.5 mm, compared to 0.8 mm observed for the sample shown in Figure 4.2.7a, the final structure achieved in the slurry optimization process. The slurry preparation method and composition was identical for all of these samples, but the BCZT powder used in the slurries was taken from different calcination batches. The samples shown in Figure 4.3.2 were made from slurries consisting of calcined BCZT from Batch 3, whereas the sample shown in Figure 4.2.7a was made with powder from Batch 2. As presented in Table 4.1.1, Batch 2 and 3 had different median particle sizes of 83 nm and 197 nm, respectively, thus indicating that the particle size of the solid load will have an impact on the size of the transition region. The lamellar structure is most apparent in the sample frozen at 1 °C/min, shown in Figures 4.3.2a and 4.3.2d. The lamellar shape of the pores begins to dissipate for the structure cooled at 5 °C/min, shown in Figures 4.3.2b and 4.3.2e. Up to a cooling rate of 10 °C/min, the lamellar shape is also not visible, and porosity appears to decrease. Although frozen with the same cooling rate of 5 °C/min, the porosity of the structures given in Figures 4.2.7a and 4.3.2b are markedly different, suggesting that the change in powder particle size of the solid load between the freeze castings was great enough that the freezing process and therefore resulting structure was significantly altered.
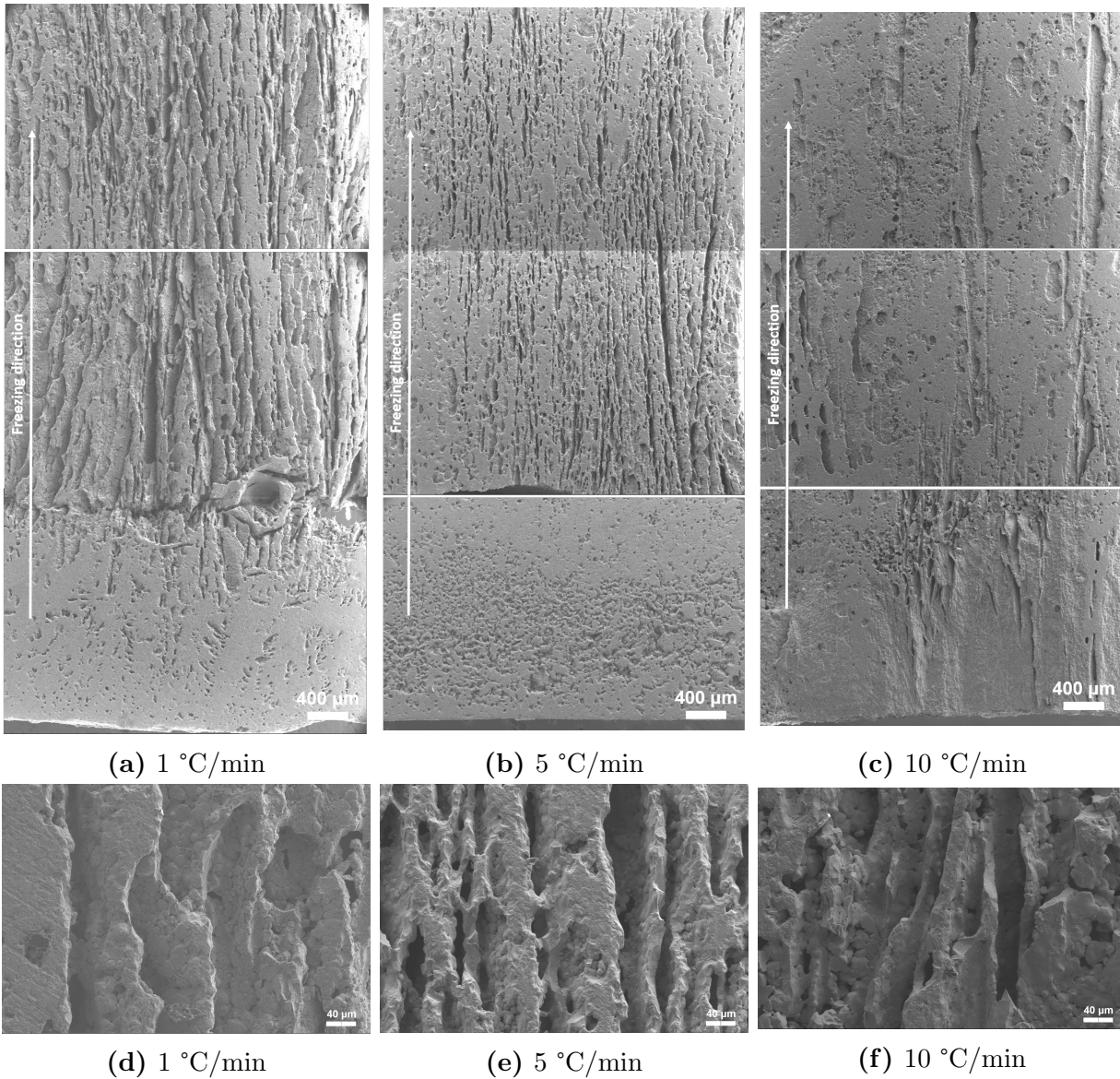
(a) 1 °C/min   **(b)** 5 °C/min   **(c)** 10 °C/min

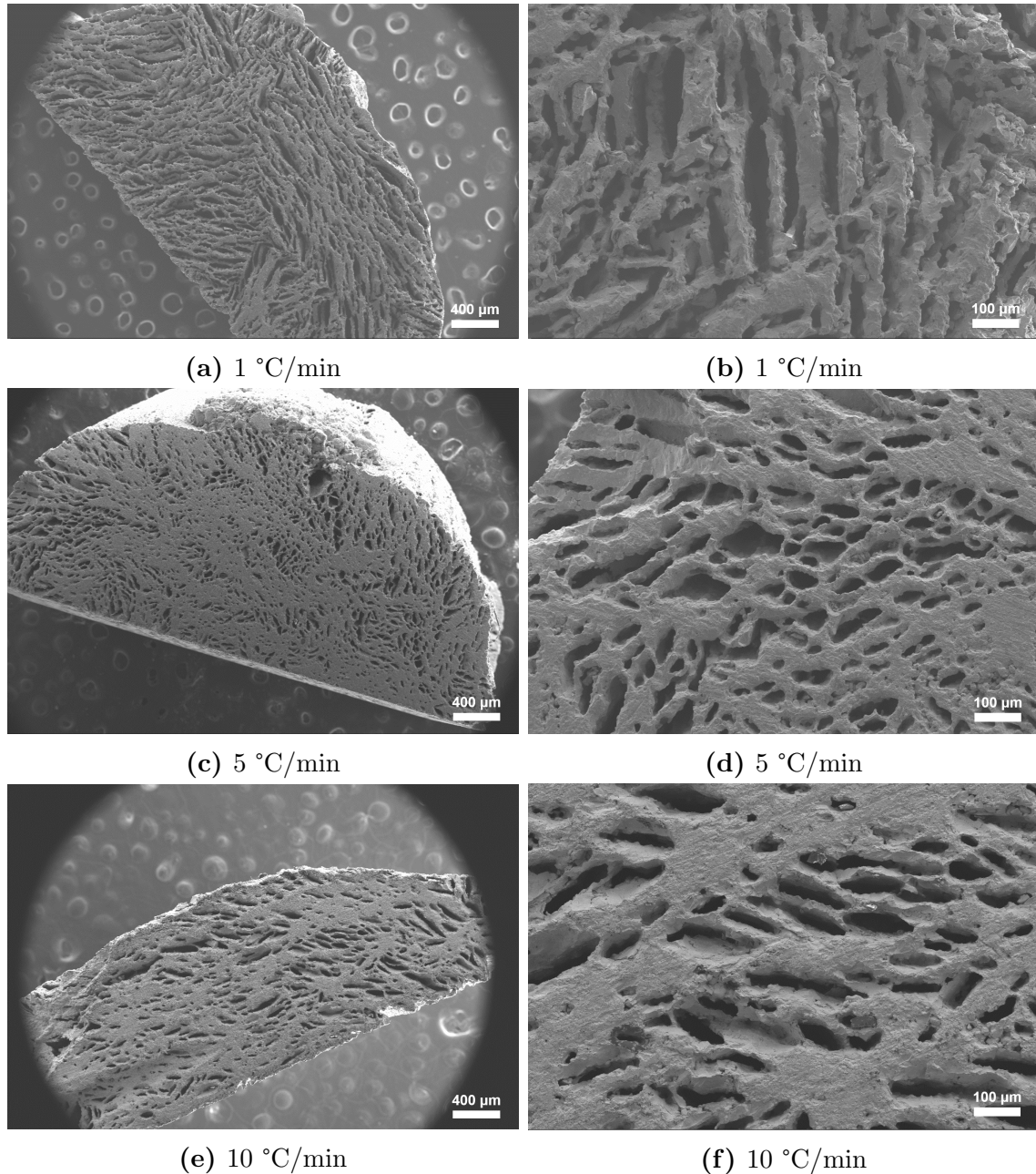**(d)** 1 °C/min   **(e)** 5 °C/min   **(f)** 10 °C/min

Figure 4.3.2: SEM images of the freeze cast samples frozen with different cooling rates of 1, 5 and 10 °C/min, all made with powder from Batch 3. Figures (a)-(c) give an overview of the structure, while figures (d)-(f) are close-up views of the pores. All images were taken perpendicular to the freezing direction.

The same trend is reflected in the SEM images taken parallel to the freezing direction, shown in Figures 4.3.3a-4.3.3f.

(a) 1 °C/min

(b) 1 °C/min

(c) 5 °C/min

(d) 5 °C/min

(e) 10 °C/min

(f) 10 °C/min

Figure 4.3.3: SEM images of the freeze cast samples frozen with different cooling rates of 1, 5 and 10 °C/min, all made with powder from Batch 3 Figures (a), (c), and (e) show the overall structure, while Figures (b), (d) and (f) gives a more detailed view of the pores. All images were taken parallel to the freezing direction.

Open and interconnected lamellar pores were achieved for the sample cooled at 1 °C/min, shown in Figures 4.3.3a and 4.3.3b. By examination of the structure, a pore length of on average 100-200 μm and pore width of about 20-50 μm was established, although pores as long as 500 μm and as short as 50 μm were also visible. Freezing with an increased cooling rate of 5 and 10 °C/min also produced open pores, however the density of pores was lower and the lamellar shape was no longer present, as shown in Figures 4.3.3c-4.3.3f. The pores

were also smaller in size, with lengths of 50-100 μm and 100 μm and widths of 15-50 μm and 25 μm for cooling rates of 5 °C/min and 10 °C/min, respectively. In addition, the dendritic surface roughness, commonly observed for freeze cast ceramics, was more pronounced in the structure cooled at 1 °C/min. Again it should be noted that the sample frozen at 5 °C/min, shown in Figures 4.3.3c and 4.3.3d, exhibited a dissimilar porous structure to that freeze cast during the slurry optimization process, shown in Figure 4.2.8. The sample made with Batch 3 of the BCZT powder was less porous and did not exhibit the lamellar structure like the sample made from Batch 2.

A total of three pieces, used for piezoelectric characterization, were cut from each freeze cast structure made with the optimized slurry composition and preparation method (four in total). The porosities of the cut-out samples were calculated from the measurements obtained from Archimedes method, according to the equations given in Appendix C. As the samples were smaller than that recommended for the method, the same measurements and calculations were conducted three times for each piece, in order to obtain a more reliable final value. Further, to get an indication of the porosity achieved with each cooling rate, the average porosity of all pieces taken from the corresponding freeze cast structure was calculated. A slight range of porosity values is expected throughout the length of the structure, as the freeze front velocity decreases with time when a constant cooling rate is applied [49]. Samples were not taken from the transition region, as it does not possess the lamellar structure of interest. Figures 4.3.4a and 4.3.4b show the respective average total and open porosity calculated for the structures frozen at each trialed cooling rate. The error bars show the maximum and minimum porosity value calculated out of all the pieces cut from the freeze cast structure. Both the samples made with Batch 3, see Section 4.3.2, and 2, see Section 4.2.5, of the calcined powder are shown.
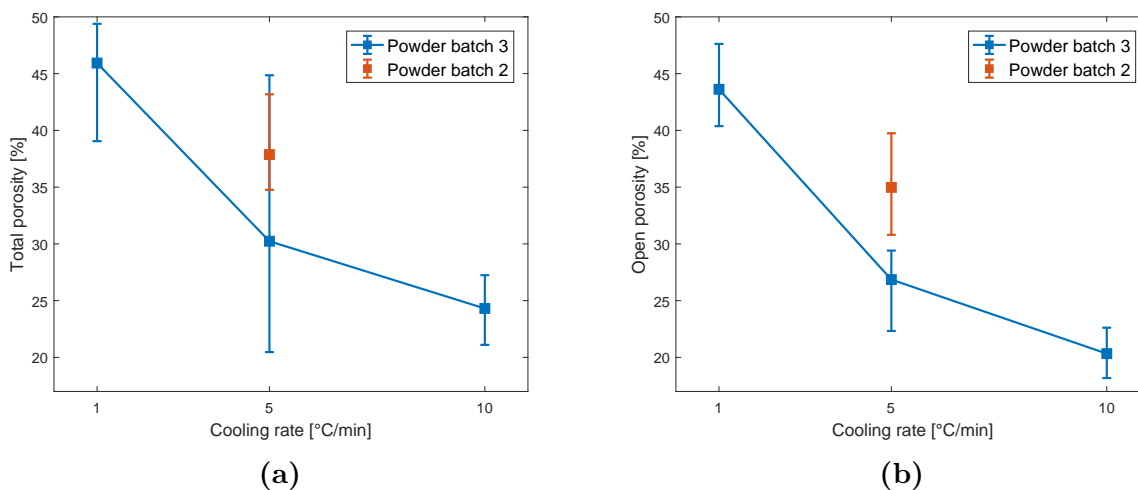

Figure 4.3.4: The average total (a) and open (b) porosity of the samples made with the optimized slurry composition, plotted again the applied cooling rate during freeze casting. The error bars give the maximum and minimum porosity calculated.

Figure 4.3.4 shows that the total and open porosity decreases with increasing cooling rate. Most of the porosity for all the samples was in the form of open pores. The highest total and open porosity achieved was 45% and 44%, respectively, for the sample cooled at 1 °C/min. As the water content of the slurries was 85 vol%, the porosity decreased by at least 40 vol% with sintering. The total porosity for the sample cooled at 5 °C/min and made with powder from Batch 3 has a relatively large error. This is due to the fact that there was a large discrepancy between the amount of total and closed porosity calculated from consecutive measurements for a single piece. The calculated open porosity was however more consistent and therefore displays a smaller error. The total and open porosity for the sample made with powder from Batch 2 is also higher than that for the sample made with Batch 3 powder and frozen with the same cooling rate, again indicating that the particle size of the solid load influenced the characteristics of the final structure.

4.3.3 Grain size

The grain size of all the freeze cast samples made with the optimized slurry composition and preparation routine were examined with a SEM. Both the lamellar- and transition regions were investigated, perpendicular and parallel to the freezing direction. The resulting SEM micrographs for the sample cooled at 5 °C/min and made with Batch 2 of the calcined BCZT powder are shown in Figure 4.3.5. The transition region displayed a larger particle size of 20-40 μm than the lamellar region, which consisted of particles with an average size of 10-30 μm. This is probably because the diffusion distance for the grains in the lamellar zone is larger, due to fewer neighboring grains, meaning growth will occur at a slower rate. The size of the grains appears to be equivalent in the perpendicular and parallel directions, and thus the grains grow isotropically. Corresponding SEM images for the other freeze cast samples can be found in Appendix D, showing similar grain sizes.
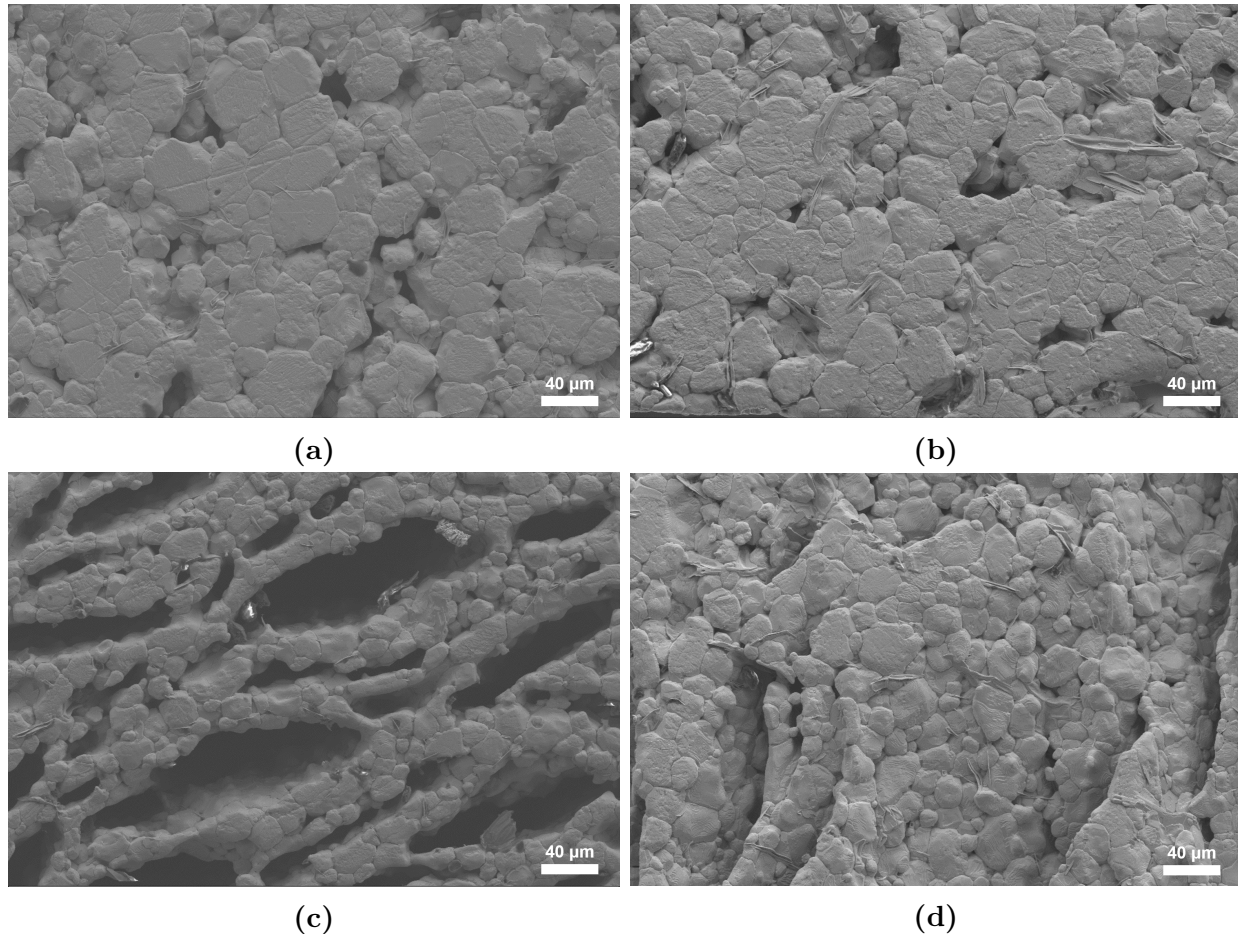
Figure 4.3.5: SEM micrographs displaying the grain structure in the freeze cast sample made with Batch 2 powder and cooled at 5 °C/min. Images are taken parallel (a,c) and perpendicular (b,d) to the freezing direction, and show grains in the transition- (a,b) and lamellar (c,d) region.

4.3.4   Piezoelectric properties

Piezoelectric characterization was conducted for the individual pieces cut from the freeze cast structures made with the optimized slurry composition, as well as the dense reference samples. As mentioned above, a total of three samples were taken from each freeze cast structure and their porosity was measured using Archimedes method. The reported porosity of the samples is the average of three consecutive measurements carried out for each piece. The samples were poled in air at an electric field of 5 kV/cm and the resulting polarization and strain loops for a selection of the samples are shown in Figure 4.3.6. Corresponding loops for all the analyzed samples can be found in Appendix E. All loops display the characteristic shape of a ferroelectric and the hysteresis is symmetric for positive and negative applied fields, signifying that the samples were poled properly. The remnant polarization and strain decrease upon the introduction of porosity in the material, as anticipated based on existing literature [20, 21, 28]. The polarization does not show a steady decrease with increasing porosity, as the hysteresis loops look similar for all porosities. The strain shows more

variation between samples, but there is no correlation between strain and pore content. The sample with 40% porosity, for example, exhibits a larger strain than the sample with 25% porosity.
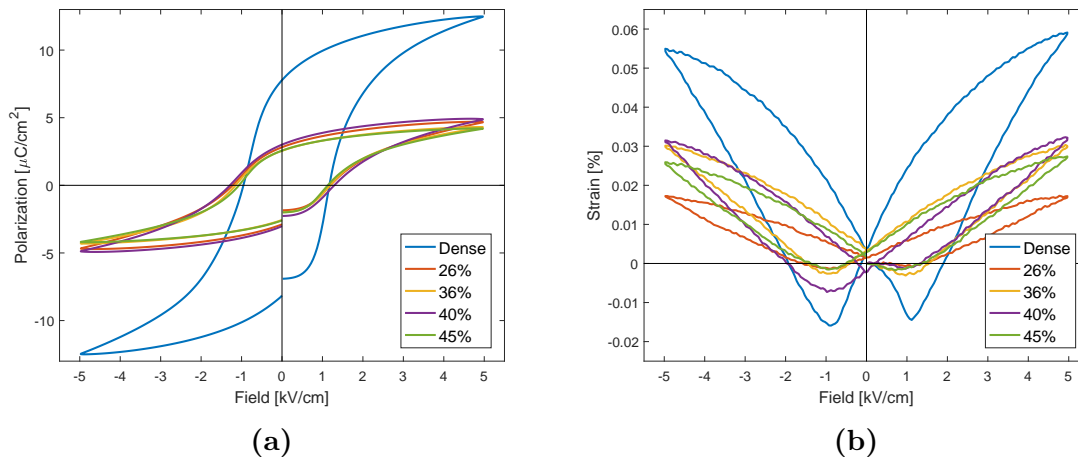

Figure 4.3.6: Polarization and strain loops for a selection of the freeze cast samples, compared to a dense reference sample.

The remnant (E = 0 kV/cm) piezoelectric coefficient, d_{33}^0, of all the analyzed samples is plotted against the total porosity in Figure 4.3.7. The presented d_{33}^0 value is the average of the 100 data points taken in each measuring cycle. As stated above, the displayed porosity is the average of the values measured for that piece. The errorbars gives the minimum and maximum porosity measured out of the three consecutive measurements conducted. The piezoelectric coefficient at a total porosity of about 5%, is the average d_{33}^0 for all the dense samples (three in total), while the errorbars give the minimum and maximum value recorded. The error in porosity, likewise, gives the minimum and maximum value measured out of all the dense samples. Piezoelectric characterization could not be conducted for two of three samples cut from the freeze cast structure frozen at 1 °C/min, as they were relatively small and therefore difficult to polish and apply electrodes to. Archimedes method was only carried out twice for one of the samples cut from the freeze cast structure cooled at 5 °C/min, and made with powder from Batch 3, shown with a respective porosity and d_{33}^0 of about 36% and 30 pm/V, and the errorbars therefore only show the range between two measurements. The same sample displays a relatively large error, as there was a large discrepancy in the total and closed porosity calculated between different measurements.

The average d_{33}^0 for the dense samples was approximately 130 pm/V. The piezoelectric coefficient decreased upon the introduction of porosity, but there is no correlation between increasing porosity and lowering of the d_{33}^0. In fact, the higher d_{33}^0 values of the freeze cast samples were indeed achieved for the samples with a higher total porosity. The largest piezoelectric coefficient of the freeze cast samples was about 100 pm/V, for a sample with 36% porosity.
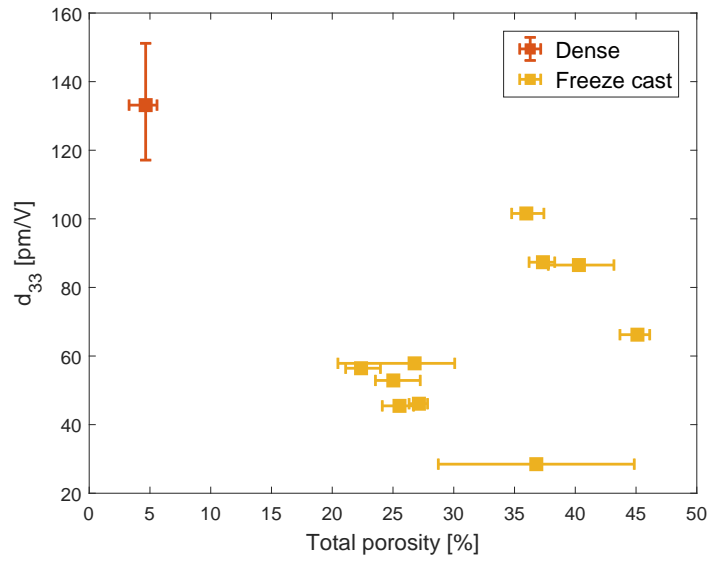
Figure 4.3.7: The remnant piezoelectric coefficient of all the freeze cast samples, plotted against porosity, compared to the average d_{33}^0 of the dense reference samples.

Chapter 5

Discussion

The aim of this thesis was to study the freeze casting process as a method of producing macroporous ceramic structures of the ferroelectric BCZT material system, appropriate for biomedical applications. The work consisted of three key points: the formation of a suitable slurry for freeze casting, testing of different freezing rates, and determination of the piezoelectric properties of the porous freeze cast structures compared to a dense reference, all of which will be discussed in the following sections.

5.1 The optimal slurry composition

As presented in Section 4.2.5, the combination of 15 vol% BCZT powder, 85 vol% deionized water, 1.5 wt% Darvan C-N and 1 wt% PVA was the most optimal slurry composition achieved in this study. The composition is designated as the most optimal, as sedimentation of the slurry did not occur, it produced a mechanically stable green body and resulted in structures with the desired lamellar porosity.

5.1.1 The use of an organic binder

The addition of 1 wt% of the organic binder PVA to the freeze casting slurries resulted in stable green bodies after sublimation of the ice. Without PVA, the green bodies both broke during the drying stage, as shown for the first freeze casting in Figure 4.2.2, and were difficult to handle without fracturing further, as shown for a barium titanate sample in Figure 4.2.4a. The PVA therefore presumably worked by its intended mechanism, of bridging the ceramic particle together through the formation of hydrogen bonds, introduced in Section 2.2.1.1. The determination of the necessary amount of binder was achieved through a simple qualitative test, where only one quantity was trialed. More thorough study is required to

determine the optimal amount of PVA that should be added. Nevertheless, the amount of binder utilized in this work is in agreement with similar studies [8, 20]. Both methods of incorporating the PVA into the slurry, either by grinding with the powder in a pestle and mortar or dissolving in heated water (described in more detail in Section 3.3), gave stable green bodies after sublimation of the ice. However, dissolving in water should give a more homogeneous distribution of PVA in the slurry and, therefore, more consistent and reliable results. It is worth pointing out that the addition of PVA to an aqueous freeze casting slurry has been shown to refine the resulting pore size and alter the ice crystal morphology from lamellar to dendritic [72], as previously mentioned. This would not be advantageous in the application of piezoelectric ceramics for bone replacement, first because large pores of above 100-150 μm in size are essential to the ingrowth of viable bone tissue [1]. Secondly, dendritic features at the pores are detrimental to the poling ability of the ceramic matrix, due to the fact that they are nonparallel with respect to the applied field, see Section 2.1.2. Nevertheless, since the level of PVA was kept relatively low, it is not expected that it significantly affected the pore morphology. If more binder was required, it could be beneficial to employ something other than PVA, such as polyethylene glycol or polyvinyl butyral.

5.1.2 Avoiding sedimentation

5.1.2.1 Sedimentation rate

As described in Section 4.2.1, the simple combination of BCZT powder and water resulted in instantaneous sedimentation of the ceramic powder. Because the density of the synthesized BCZT was approximately five times higher (see Table **??**) than the density of water, sedimentation is clearly expected. According to Equation 2.3, presented in Section 2.2.1.1, the sedimenta- tion velocity of a single BCZT particle from Batch 1 in water is approximately 0.06 μm/s, using the following data for the calculation: $\rho_p = 5.497$ g/cm^3 (taken from Table **??**), $\rho_l = 0.988$ g/cm^3 [82], r = 80 nm (the median particle size, taken from Table 4.1.1) and $\eta = 1$ mPas [83], and assuming a temperature of 20 °C. This relatively low rate indicates that significant sedimentation should not occur within the slurry preparation and freezing time. However, the equation only describes the simplified situation of a single particle in water, and does not take into account the interactions between multiple particles. Due to the rapid sedimentation of the BCZT powder, significant particle interaction and agglomeration due to attractive van der Waals forces is probable.

5.1.2.2 The effect of sedimentation on microstructure

According to the sedimentation test, the addition of 1.5 wt% Darvan C-N was adequate to achieve a stable BCZT dispersion, that remained well dispersed for at least 4 hours, as shown in Figure 4.2.1. The same amount was, however, not sufficient to avoid sedimentation of the slurries during freeze casting. This is not necessarily surprising, as the large increase

in powder content from the sedimentation test, which was only 0.5 wt%, implies that the distance between the particles in the slurries was significantly smaller. The probability for particle interaction and agglomeration was thereby likely even higher, resulting in increased sedimentation. Sedimentation of the freeze casting slurries was first suspected after sintering, due to the inconsistent diameter of the structure made with 15 vol% powder, shown in Figure 4.2.5a. The reasoning behind this assumption was that with settling of the powder particles, the water content, and therefore porosity after freeze casting and sublimation, would be higher towards the top of the sample. A greater amount of porosity at the top of the structure might lead to increased shrinkage, compared to the bottom portion, during sintering. Secondly, the same sample did not display the lamellar structure throughout its entire length, but demonstrated a microstructural gradient consisting of regions with dense ceramic and irregular pores (Figure 4.2.5b) in the lower part of the sample, and the desired lamellar porosity (Figure 4.2.5c) at the top of the sample. Due to settling of the particles, the concentration of powder in the bottom portion of the sample may have been too high for particle redistribution to occur. As mentioned in Section 2.2.2, above a concentration of about 55-60 vol%, templating by the ice crystals can no longer take place and the lamellar structure is lost. On the other hand, at the top of the sample, the powder content was within a range that the particles were repelled by the ice front, resulting in the formation of lamellar pores. The same explanation applies to the sample with 15 vol% powder and 3 wt% Darvan C-N, shown in Appendix D.

The lamellar portion was only visible for the freeze cast samples made with 15 vol% powder, not for the samples with 20 and 25 vol% powder. This may be due to the higher concentration of BCZT powder, which as explained above presumable increases the sedimentation rate. A higher degree of sedimentation in these samples might have resulted in a larger portion containing a particle concentration that is too high for redistribution, whereas the top of the sample might primarily have consisted of ice that was removed upon drying, and therefore no lamellar structure. In addition, the slurry made with 20 vol% powder was prepared together with and frozen after the sample with 15 vol% powder, giving the particles more time to settle. In the case of the sample with 25 vol% (65 wt%) BCZT, it is possible that the powder content was actually too high to form the lamellar structure, regardless of sedimentation. *Deville et al.*, for instance, reported that the lamellar structure of freeze cast hydroxyapatite was lost at a solid load above 65 wt% [19]. This was attributed to the interaction between the ceramic particles, so that they could no longer be repelled by the ice front.

5.1.2.3 Viscosity and the stability of the slurries

Increasing the amount of Darvan C-N to 5 wt% produced a stable freeze casting slurry, without significant sedimentation during preparation and freezing. Greater stability, compared to the previous samples, was first and foremost apparent due to the constant diameter and lamellar structure throughout the length of the sample, as shown in Figure 4.2.7a. The viscosity data, given in Figure 4.2.9, also indicates a better stability for the sample with 5

wt% dispersant, as the viscosity was lower for all shear rates [59] and the slurry demonstrates less hysteresis between shear up and shear down modes, compared to the slurry with 1.5 wt% dispersant. This thus suggests that the ammonium polymethacrylate in the Darvan C-N exhibited a stabilizing effect in the BCZT slurry. As detailed in Section 2.2.1.2, there is a critical freezing front velocity, at which the ceramic particles are encapsulated by the ice and the lamellar structure will not be formed. The critical velocity is inversely proportional to the slurry viscosity, as indicated by Equation 2.6. Due to its higher viscosity, the slurry with 1.5 wt% Darvan C-N should therefore have a lower critical velocity for encapsulation, than the slurry with 5 wt% dispersant. Consequently, it is conceivable that the freezing front velocity for the slurry with 1.5 wt% Darvan C-N was sufficiently high that encapsulation occurred, yielding a portion with dense ceramic and irregular pores in the resulting structure, as shown in Figure 4.2.5b. Furthermore, the solidification front velocity will decrease with time, when a constant cooling rate is applied [49], and could thus have been low enough towards the top of the sample that encapsulation did not occur. This would explain why the top of the same sample displayed the lamellar porous structure, shown in Figure 4.2.5c. Both sedimentation and slurry viscosity can, therefore, serve as reasons for the abnormal sample shape, achieved from freeze casting #3, given in Table 3.3.1.

5.1.2.4 The stabilization mechanism of ammonium polymethacrylate

The absolute value of the zeta potential, given in Table 4.2.1, was higher at all concentrations of Darvan C-N, than for the suspension without Darvan C-N, again demonstrating that the ammonium polymethacrylate performs a stabilizing function in the BCZT freeze casting slurries. As stated in Section 2.2.1.1, a zeta potential above ±30 mV usually signifies a stable dispersion [54]. Although the suspension without dispersant fulfilled this requirement, having a zeta potential of -35.8 mV, the combination of solely powder in water was not stable, since sedimentation occurred instantly. Nevertheless, it is important to note that the zeta potential does not give any indication on the level of attractive van der Waals forces between the particles, which in this case appear to be significant. As briefly mentioned in Section 2.2.1.1, ammonium polymethacrylate stabilizes ceramic powder suspensions by binding to the positive surface sites of the particles with its negatively charged acetate group. BCZT particles in water are, however, negatively charged, due to the preferential leaching of, primarily Ba^{2+} ions and, to an extent, Ca^{2+} ions. Leaching is more severe for the Ba and Ca ions, rather than the Ti and Zr ions, as they have a lower ionic field strength [84]. Despite this, *Jean & Wang* proposed that stabilization of aqueous barium titanate with ammonium polymethacrylate could occur by a binding of the polymeric dispersant to minority positive Ba-sites, as illustrated in Figure 5.1.1 [55]. Figure 5.1.1 shows that the Ti-sites and Ba-sites on the surface of the barium titanate particles are negatively and positively charged, respectively. This is related to the interaction of the surface of the particles with protons and hydroxide ions in the water, as briefly introduced in Section 2.2.1.1. It is important to note that the charge of the surface depends on the pH of the suspension. *Jean & Wang* demonstrated that at a relatively neutral pH, the surface should resemble that shown in Figure 5.1.1. Stabilization is thus achieved both by the electrostatic

repulsion between the negatively charged acetate groups (those that do not bind to the particle surface), and steric repulsion from the presence of polymer chains. The same mechanism might indeed take place for the aqueous BCZT suspension, and would explain why the absolute value of the zeta potential increased upon the addition of Darvan C-N.
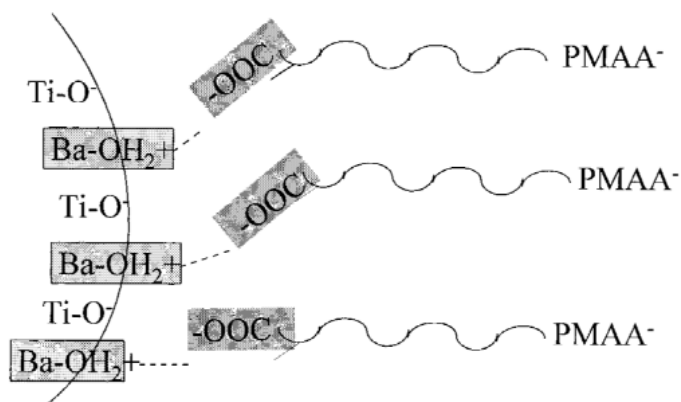

Figure 5.1.1: Schematic of the binding of polymethacrylate on the surface of barium titanate particles in water, proposed by *Jean & Wang*. The stabilization mechanism is electrosteric, due to the presence of negatively charged acetate groups and polymer species [55].

The zeta potential did not increase with increasing amount of added Darvan C-N (see Table 4.2.1), although it is clear from the results presented above that the slurry with 5 wt% dispersant indeed was the most stable. This indicates that greater stabilization, with 5 wt% Darvan C-N, was not achieved due to a higher level of electrostatic repulsion between the particles. Consequently, stabilization of the BCZT slurries may not only be accounted to the mechanism shown in Figure 5.1.1. It is possible that increased stabilization was achieved by a depletion mechanism, meaning from free polyelectrolyte species that did not attach to the particle. Figure 5.1.2 illustrates the proposed method, demonstrating that the steric, and possibly electrostatic, repulsion induced from the unattached dispersant prevents interaction between the BCZT particles. Increasing the amount of Darvan C-N to 5 wt% may have resulted in a higher amount of free electrolyte, and in this way given greater stabilization. Excess polyelectrolye would not be registered in the zeta potential measurements, and explains why the zeta potential was not highest for the suspension with 5 wt% Darvan C-N. To test if this is a plausible explanation, the powder could be separated out of the dispersant solution by centrifugation, and then redispersed before mixing of the slurry for freeze casting. In this way, any potential excess dispersant would be washed away. It is important to note that free dispersant in the freeze casting slurry can affect the freezing process, although a general mechanism has not been identified.

The charge of the polymethacrylate depends on the degree of dissociation. As polymethacrylate is an anionic dispersant, ionization increases with increasing pH [50]. It is thereby possible that employing a higher pH in the freeze casting slurries could give increased stabilization, at a lower concentration of Darvan C-N, as the charge on each polymer chain
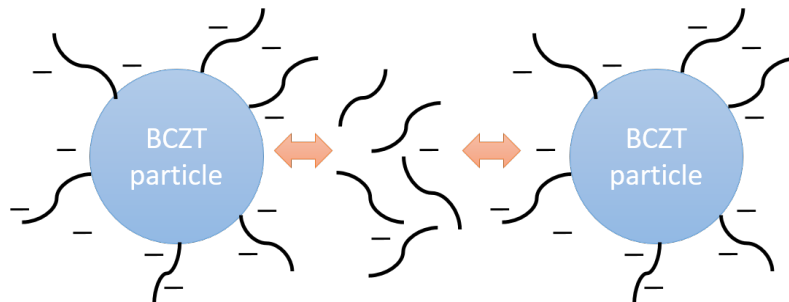
Figure 5.1.2: Illustration of a potential depletion mechanism, yielding increased stabilization of the BCZT slurries due to repulsion from the polyelectrolye dipsersant that is not attached to the particles. The conformation of the polyelectrolyte does not necessarily represent what is occurring in the slurry, but is simply used for illustration purposes.

would be higher. In addition, a higher charge on the polymer chain results in a more open coil configuration of the polyelectrolye, due to repulsion between neighboring acetate groups. Thus, both the electrostatic and steric repulsion increase at a higher pH. Increasing the pH could, on the other hand, decrease adsorption of the polymethacrylate on the BCZT particles, due to increased repulsion between the negative acetate groups and Ti surface sites. It is, therefore, recommended to test the effect of pH on the stability of the slurries in further studies.

The difference in the stability of the slurries with 1.5, 3 and 5 wt% Darvan C-N, despite similar zeta potentials, could also be related to a potential interaction between the powder, PVA and Darvan C-N. *Iwata & Mori* demonstrated that the addition of PVA to a barium titanate suspension, stabilized with polycarboxylic acid, resulted in destabilization of the dispersion [85]. This was attributed to an interaction between the dispersant and binder, which decreased the particle distance and gave aggregation of the particles. *Iwata & Mori* also show that by increasing the amount of dispersant, the particle aggregation decreased. The reason for this was suggested to be that the PVA would interact with the free excess polyelectrolye, rather than the polyelectrolye bound to the particle. Based on this, it is conceivable that the addition of 1.5 wt% Darvan C-N was sufficient to achieve a stable dispersion, without the presence of PVA. This might explain why the suspension from the sedimentation test appeared stable, and that the zeta potential was similar for different concentrations of Darvan C-N, as none of these suspensions contained PVA. In the freeze casting slurries, on the other hand, the presence of PVA may have destabilized the suspension, so that more dispersant was required. Another possibility is that the PVA may have affected the adsorption of polymethacrylate on the particle [86]. This would depend on the number of available surface sites and the maximum adsorption of the dispersant on the particle. It is in any case clear that much more study is required to determine the stabilizing effect of the ammonium polymethacrylate, and the optimal amount required for stabilization of the freeze casting slurries.

5.2   Characteristics of the freeze cast structures

5.2.1   The transition region

All of the freeze cast samples made with the optimized slurry composition displayed a microstructural gradient at the bottom of the structure, shown in Figures 4.2.7a and 4.3.2a-4.3.2c. As described in Section 2.2.2, such a transition region has also been reported in other freeze casting studies [19, 62], and is due to the initially fast growth of the ice at the onset of freezing, leading to encapsulation of the ceramic particles. It is important to point out that this is not related to sedimentation, characterized in the previous section, although the resulting microstructures may look the same. The length of the transition zone was different depending on the particle size of the BCZT powder utilized in the slurry. Samples made with powder taken from calcination Batch 3, with a median particle size of 197 nm, formed a 1.5 mm high transition zone, while for the sample made with powder from Batch 2, median size 80 nm, it only reached 0.8 mm. This is in agreement with the theory proposed by *Deville et al.*, that the length of the transition zone is controlled by the particle size. Specifically, smaller particles offer a larger number of possible ice nucleation sites, and hence, solidification can proceed at higher temperatures, meaning the system is in a less supercooled state. A smaller degree of supercooling corresponds to a shorter transition region, as it will take less time for the system to reach equilibrium and a steady state growth regime where encapsulation no longer occurs [69].

5.2.2   The effect of cooling rate and particle size

As described in Section 4.3.2, for the samples made with powder from calcination Batch 3, the lamellar structure was mostly visible for the sample frozen at 1 °C/min, and began to dissipate at cooling rates of 5 and 10 °C/min, although the structures still displayed open pores. In addition, the sample frozen at 5 °C/min exhibited a very different microstructure than the sample frozen with the same cooling rate, but made with powder from Batch 2. The change in structure was clearly indicated by the SEM images taken parallel to the freezing direction, given in Figure 4.2.8 and Figures 4.3.3, which show that the pores both decreased in size and did not have the characteristic lamellar shape. A decrease in pore width with increasing cooling rate is in accordance with the literature, as the more rapid growth of the ice produces a smaller ice tip radius, as explained in Section 2.2.2 [8, 19, 62]. The length and shape of the pores should, however, have been retained.

As the same optimal slurry composition was used for all the freeze castings, the change in porosity is considered to be related to the change in particle size between the two powder batches. Figure 5.2.1 shows the diagram introduced in Figure 2.2.9 in Section 2.2.2, which gives the dependency of the resulting freeze cast structure on the freezing front velocity and particle size of the solid load, marked with the median particle size of BCZT powder

Batch 2 and 3. It is proposed that the solidification front velocity during freezing of the BCZT samples was within the blue hatched region, in close vicinity to the boundary between encapsulation and the formation of lamellar pores. For freeze casting of the sample made with powder from Batch 2, it is assumed that the interface velocity is such that the structure lies in the green region of the diagram, point A, where lamellar pores are formed. This is presumed to be reasonable, because the sample exhibited the lamellar microstructure, as shown in Figures 4.2.7 and 4.2.8. If the interface velocity is kept constant, meaning the cooling rate is unchanged, and the particle size is increased to that of Batch 3, point B is reached. It is suggested that within this region, the system is at a balance between encapsulation and the formation of lamellar pores, which would explain why the sample frozen at 5 °C/min and made with powder from Batch 3 displayed open and partially aligned pores, but without the lamellar shape, as shown in Figures 4.3.2b and 4.3.3c. Encapsulation becomes more severe when the cooling rate is increased to 10 °C/min at point C. Increased particle encapsulation is in agreement with the fact that the lamellar structure was not present for the sample cooled at 10 °C/min and that the porosity appeared to be even lower, as shown in Figures 4.3.2c and 4.3.3e. Finally, when the cooling rate was decreased to 1 °C/min, the structure might have again been within the green region, point D, since lamellar pores were also formed for this sample, as shown in Figures 4.3.2a and 4.3.3a. Like it was mentioned in Section 5.1.2, the interface velocity was not recorded in this study, and the points A-D given in Figure 5.2.1 are therefore not measured data points, but used to illustrate the proposed argument for the change in porosity with particle size.
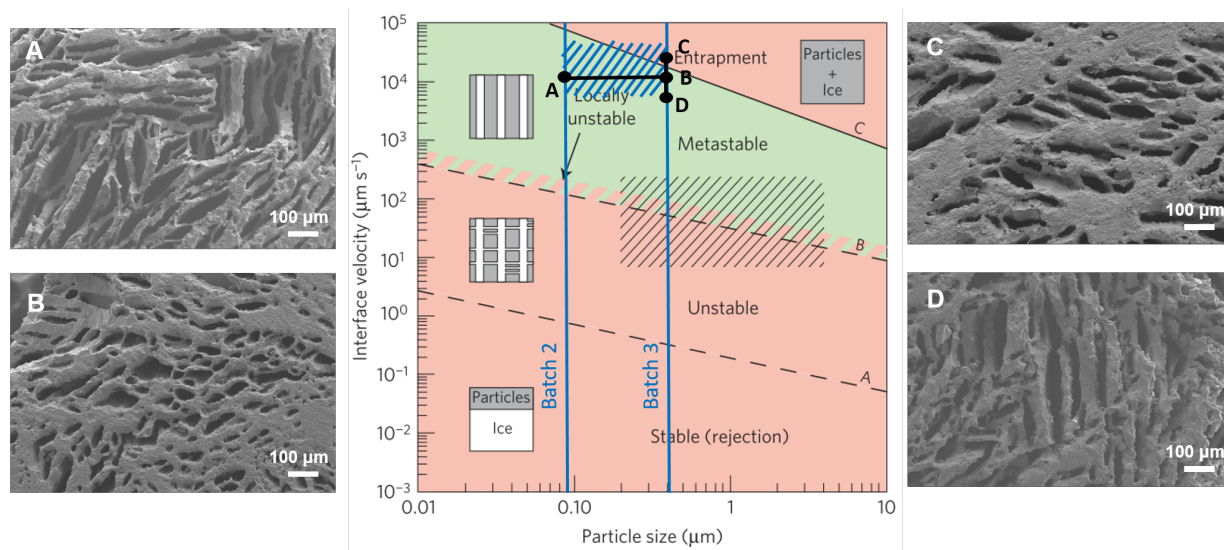

Figure 5.2.1: Diagram showing the dependency of the freeze cast structure on the interface velocity and particle size, marked with the median particle sizes of BCZT Batch 2 and 3. The points A-D indicate the position in the diagram for each freeze casting, and the corresponding SEM images of the resulting structures are also shown. The applied cooling rate at each point is 5 (A), 5 (B), 10 (C) and 1 (D) °C/min.

According to the diagram given in Figure 5.2.1, and the theory presented above, there were thus two possible methods of moving the system away from the boundary region between

encapsulation and the formation of lamellar pores: employing a smaller particle size in the solid load or decreasing the freezing front velocity by dropping the cooling rate. Utilizing BCZT powder with a particle size close to that of Batch 2 is, however, considered to be a better solution, as otherwise the system would be relatively limited with regards to the applied cooling rate. The interface velocity is also dependant on the thermal conductivity of the solidified phase [61], however, if the slurry composition it to remain unchanged, this can not be altered.

5.2.3   Total porosity

The difference in the microstructures formed during freeze casting was also reflected in the total porosity obtained for each structure, plotted against freezing rate in Figure 4.3.4. As the amount of water was the same in all the slurries, it might be expected that the total porosity should not significantly change with freezing rate. However, due to the change in structure from partial encapsulation of the powder particles (for samples frozen at 5 and 10 °C/min and made with powder from Batch 3), the shirnkage during sintering was perhaps altered. Even without the difference in microstructure, it is somewhat expected that the total porosity should decrease with increasing freezing rate, as it has been demonstrated in other studies [8, 41]. This may be because a higher density of thin pores will increase the surface energy of the system and thereby also the driving force for sintering, resulting in increased shrinkage [65]. Alternatively, *Li et al.* state that a higher freezing velocity results in increased shrinkage during sintering due to the fact that the particles are more loosely packed in the walls [41]. The shrinkage was, in general, relatively high for the structures processed in this study, as the porosity decreased by at least 40% with sintering. As noted in Section 2.2.1.4, *Deville* states that the porosity usually only reduces by about 10-25%. Considerable shrinkage during sintering can make it more difficult to achieve the large pore size required for bone replacement materials, and is in this sense not beneficial. The degree of shrinkage can be reduced by lowering the sintering temperature and/or time, however, this would have to be weighed up against the potential decrease in the ceramic matrix density, which would also affect the mechanical and piezoelectric properties of the final material.

5.2.4   Pore size

It has previously been stated that a pore size of 100-150 μm is required to ensure ingrowth of viable bone tissue into an implant. The largest pore width achieved in this study was only 50 μm, for the samples frozen at 5 and 1 °C/min and made with powder from Batch 2 and 3, respectively, shown in Figures 4.2.8, 4.3.3a and 4.3.3b. Although the pore size should increase when the cooling rate is reduced, it remained unaffected due to the increase in particle size between the two powder batches. Decreased pore width with increasing particle size can be understood by the effects of supercooling introduced above. As the degree of supercooling becomes larger with increasing ceramic particle size in the slurry, the ice growth

will consequently be more rapid, resulting in the formation of thinner pores. This has also been demonstrated in the work by *Miller et al.* on freeze casting of alumina [87]. It is thereby expected that if the particle dimension was kept at that of Batch 2, reducing the cooling rate would have resulted in the formation of larger pores.

5.3   Piezoelectric characterization

5.3.1   The degree of poling in the freeze cast samples

Figure 4.3.6a shows that the freeze cast samples were successfully poled, in the sense that partial discharge did not occur within the pores, upon the application of an electric field of 5 kV/cm. To get a better sense of how well the samples were poled, the remnant polarization (E = 0) of all the measured samples was analyzed against the porosity of the pieces, and the data is presented in Figure 5.3.1. The displayed P_R value is the average of the absolute value of the positive and negative P_R. The porosity, and its corresponding error, of all the samples were calculated in the same way as for Figure 4.3.7, described in Section 4.3.4. Only one data point is shown for the sample frozen at 1 °C/min, as, like it was mentioned in Section 4.3.4, the other two pieces were too difficult to work with. The error in the remnant polarization of the dense samples gives the minimum and maximum value measured out of all the pellets. Included in Figure 5.3.1 is the remnant polarization calculated according to Equation 2.2, where the decrease in the P_R is described only by the increase in the volume fraction of pores in the material, and the effect of the pores on the electric field is not taken into account. In other words, it is the remnant polarization that would be achieved if the ceramic matrix in the porous structure were perfectly poled. The reference polarization P_R^0, meaning that of the completely dense ceramic, was calculated from the average measured P_R of the dense pellets, corrected for their average amount of porosity, which was about 4%. This calculation is not absolutely correct, as it requires the assumption that the electric field was completely homogeneous across the dense samples, despite the fact that there were a small amount of pores present. The true P_R^0 would therefore be slightly higher than the one calculated here. Equation 2.2 will nevertheless give an indication as to what degree the pores affected the poling ability of the ceramic matrix in the freeze cast samples.
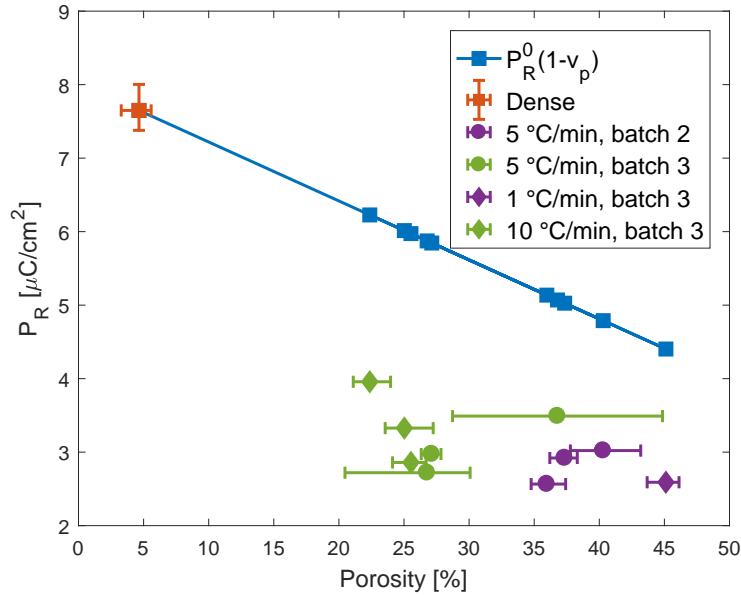
Figure 5.3.1: The remnant polarization of the freeze cast samples and dense pellets, plotted with the remnant polarization calculated according to the volume fraction of pores present. The cooling rate during freezing and employed powder batch for the slurry is indicated for all the freeze cast samples.

The average remnant polarization of the dense samples was 7.6 $\mu C/cm^2$, which is comparable to P_R values for BCZT presented in other works, for instance 6.27 and 7.7 $\mu C/cm^2$ reported by *Yap et al.* and *Zhang et al*, respectively [21, 28]. The remnant polarization of the experimentally measured freeze cast samples, as expected, lie below the value calculated based on the volume fraction of pores. As explained in Section 2.1.2, an ideal lamellar porous structure should allow for the formation of a homogeneous electric field and therefore complete poling of the ferroelectric matrix. A freeze cast structure will, however, inevitably contain structural defects that result in the formation of an inhomogeneous electric field across the material, and consequently incomplete poling of parts of the ceramic. The specific types of defects will be discussed further below.

As pointed out in Section 4.3.4, the remnant polarization of all the freeze cast samples were relatively similar. In other words, made clear from Figure 5.3.1, the remnant polarization of the samples frozen at 5 °C/min and 10 °C/min (marked in green in Figure 5.3.1), and made with Batch 3 powder, were further from the corresponding calculated values than the other samples. According to the study by *Zhang et al.* on freeze casting of $BC_{0.15}Z_{0.1}T$, the remnant polarization is expected to show an approximately linear decrease with increasing porosity [21]. The reason behind the seemingly arbitrary trend observed here is presumed to be related to the difference in microstructure achieved for the different freeze cast samples, depending on the applied cooling rate and BCZT powder batch, as discussed in Section 5.2. The samples frozen with a cooling rate of 5 °C/min and 1 °C/min (marked in purple in Figure 5.3.1), and made with powder from, respectively Batch 2 and 3, displayed a more

ideal lamellar structure, and therefore probably contained less defects. Partial encapsulation of the powder particles during freezing of the structures cooled at 5 °C/min and 10 °C/min, containing Batch 3 powder, on the other hand, likely resulted in the formation of a higher number of structural imperfections. It is evident that a larger amount of defects leads to a greater distortion of the applied electric field, and therefore more regions of insufficiently poled ceramic matrix. The data given in Figure 5.3.1 can thereby be understood quite clearly. The samples displaying a more ideal lamellar structure contained less defects, resulting in a less distorted field across the ceramic and more complete poling, whereas the samples that experienced encapsulation during freezing had a larger amount of defects, resulting in a more inhomogeneous electric field and less poled ceramic. Together, the effect of the volume fraction of pores and the effect of the pores on the applied electric field during poling, resulted in relatively similar hysteresis loops for all the freeze cast samples. The samples with the more ideal lamellar structure display P_R values that are similar to that reported by *Zhang et al.* for the same porosity [21].

In Section 2.1.2 it was stated that if the electric field across a material is inhomogeneous, ferroelectric switching will occur over a broader electric field distribution during poling [21]. Therefore, to further investigate the arguments proposed above, the current density during poling of the samples was analyzed. Figure 5.3.2 shows the current density of a dense sample and one sample from each freeze casting. The current density was normalized with respect to the maximum current measured for each piece, as this gave a more clear view of the difference in the width of the electric field distribution. Current density hysteresis loops for all the samples are given in Appendix E. The electric field distribution for the dense sample is the most sharp, as the peak in the current occurs across a more narrow range of electric fields. This is expected, as the electric field across a dense material should be fairly homogeneous. For the freeze cast samples, the field distribution is slightly more narrow for the samples that displayed a more ideal lamellar structure than for the samples that experienced significant particle encapsulation during freezing, thus indicating that the electric field was more homogeneous in these samples. The explanation given above, on the degree of poling achieved for the different structures, therefore seems probable. The coercive field of the dense BCZT samples, at a positive applied electric field, was about 1.1 kV/cm, which is comparable to values reported in the literature [28,76]. The current density hysteresis loop is, however, slightly asymmetric, with a different E_C for positive and negative electric fields. This could for example be due to a different level of polishing achieved on the two surfaces of the sample, which might have affected the application of the gold electrodes and, therefore, the poling process. The hysteresis is more symmetric for the porous samples, and the E_C does not change significantly by the introduction of pores. As outlined in Section 2.1.2, varying results have been reported with regards to the effect of pores on the coercive field.
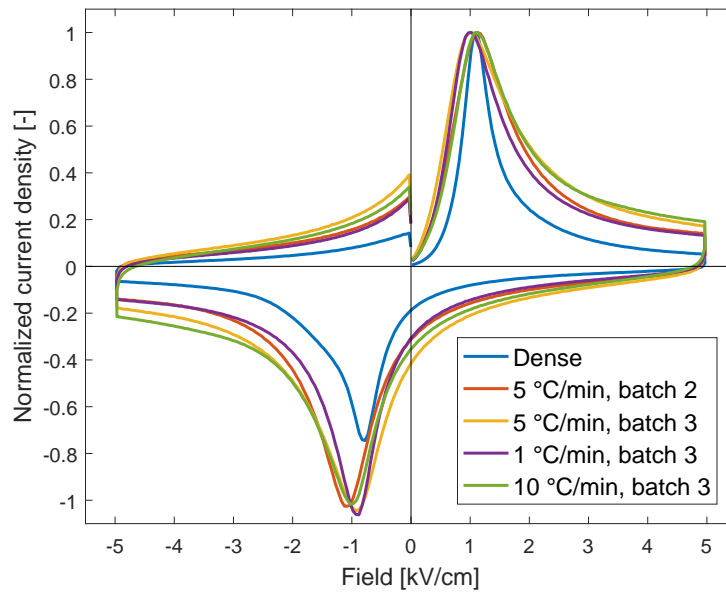
Figure 5.3.2: The current density of a representative dense sample and one sample from each freeze casting, normalized with respect to the maximum current density measured for each sample.

The measured remnant piezoelectric coefficients, shown in Figure 4.3.7, reflect the principles presented above. As described in Section 2.2.3, in an ideal lamellar porous structure, the d_{33}^0 is independent of porosity, because the structure should support the formation of a homogeneous poling field and thereby full poling of the ceramic [20]. However, in a freeze cast material, it might be expected that the d_{33}^0 will decrease with increasing porosity, as a higher porosity increases the chances for the presence of defects. However, for the samples processed in this work, the d_{33}^0 generally increased with increasing porosity. This is, as proposed above, due to the difference in the microstructure of the samples. Figure 5.3.3 displays the same d_{33}^0 data, but distinguishes between what freeze casting each sample was taken from. The samples with the highest d_{33}^0 values are also the samples that displayed the most lamellar structure, contained less defects and therefore achieved better poling of the ceramic matrix.
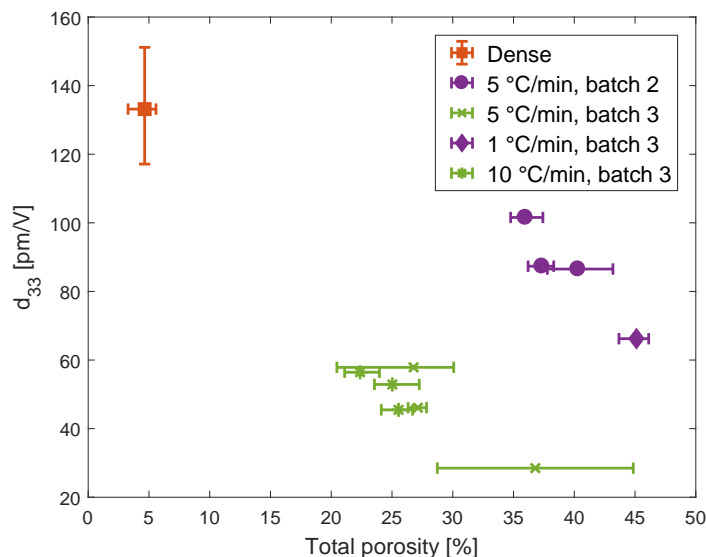
Figure 5.3.3: The remnant piezoelectric coefficient of the dense and freeze cast samples, with the cooling rate and applied BCZT powder batch indicated for each sample.

The average remnant piezoelectric coefficient of the dense samples was about 130 pm/V. This is lower than expected, compared to what has been reported in the literature [11, 75, 76]. However, as mentioned in Section 2.3, there is also much variation in the d_{33}^0 reported in different publications in the literature, which may be due to differences in processing conditions, microstructure, measuring technique and poling conditions [75]. The reduction in the d_{33}^0 upon the introduction of pores into the BCZT ceramic is, as stated above, presumably due to the presence of defects in the porous structure. In Section 2.2.3, two different types of defects were mentioned, namely the presence of pores, either open or closed, in the ceramic walls, and ceramic bridges within the porous channels [20], which are illustrated in Figures 5.3.4a and 5.3.4b, respectively. In addition, the lamella may not be perfectly aligned throughout the structure, as shown in Figure 5.3.4c.

(a)　　　　　　　　　　(b)　　　　　　　　　　(c)
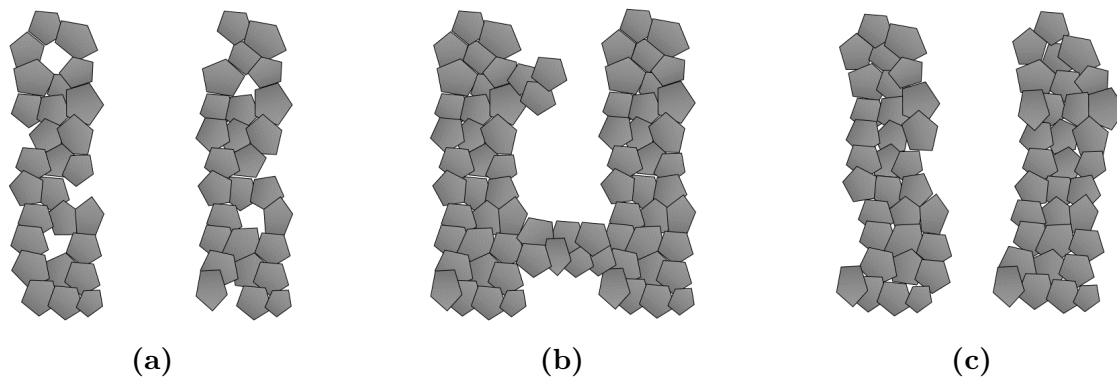
Figure 5.3.4: Illustration of the typical defects in a freeze cast structure: (a) Pores in the ceramic walls (b) Ceramic bridges in the porous channels (c) Tilted lamella.

To check how much the closed porosity affected the d_{33}^0, it was plotted for all the samples in Figure 5.3.5. The data points and their corresponding errors were found in the same way as for Figure 4.3.7. As shown in Figure 5.3.5, the calculated closed porosities were negative for some samples. This is of course not technically possibly, and was likely due to the relatively high uncertainty of the measurements, which was, as mentioned in Section 3.6.3, expected due to the small sample size. The dry- and suspended mass were presumably relatively accurate, and the error therefore probably comes from the wet mass measurement, as the small sample size and large amount of open pores made it difficult to control how much isopropanol was removed from the sample before the mass was recorded. The high level of uncertainty in the measurements also explains why the error in some of the values were relatively large, compared to the error for the dense samples. Despite the high uncertainty, there does not appear to be any correlation between an increase in the closed porosity and a reduction in the remnant piezoelectric coefficient. The decrease in the d_{33}^0 was, therefore, presumably caused by the presence of a combination of open porosity in the ceramic layers, ceramic bridges and tilted lamella. It is, at this stage, difficult to say how much of these defects were present in the structures. To get a more clear picture of the structure, more detailed SEM analysis could be conducted. An even more clear overview could also be achieved by X-ray microtomography. *Roscow et al.* reported that the piezoelectric coefficient of freeze cast barium titanate, with a porosity of 45%, reached 93% of the dense value [20]. A high piezoelectric coefficient for porous freeze cast PZT has also been reported by *Zhang et al.*, where values were between 65-84% of the dense reference, for porosities at 20-60% [88]. The highest remnant piezoelectric coefficient measured for the freeze cast samples in this study was 77% of the dense value, for a porosity of 36%, and is therefore comparable to what has been reported in the literature.
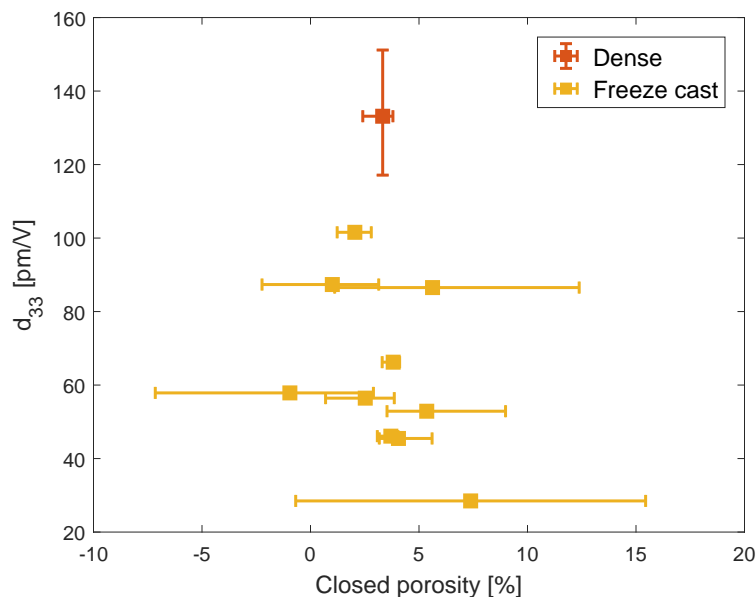

Figure 5.3.5: The remnant piezoelectric coefficient of the dense and freeze cast samples plotted against closed porosity.

Chapter 6

Conclusion

In this study, lamellar porous BCZT structures were successfully prepared using the freeze casting method. An optimal slurry composition consisting of 15 vol% BCZT powder, 85 vol% deionized water, 5 wt% Darvan C-N and 1 wt% PVA, which functioned as, respectively, the solid load, freezing liquid, dispersant and binder, was achieved. The addition of 1 wt% binder resulted in a mechanically stable green body after sublimation of the ice. A concentration of 5 wt% of dispersant was required to prevent sedimentation of the slurries during preparation and freezing. Zeta potential measurements indicated that the ammonium polymethacrylate dispersant stabilized the BCZT particles by binding to the positive surface sites of the particles. However, as the zeta potential measurements did not reflect the increase in stability with increasing Darvan C-N content, other mechanisms were likely also taking place. Depletion stabilization and interactions with PVA might explain these results. Further study is required to fully establish the effect of ammonium polymethacrylate in the BCZT suspensions.

Lamellar porous structures with a porosity of up to 45% were achieved, by freeze casting with a cooling rate of 1 °C/min and 5 °C/min. Pores were on average 100-200 μm long and 20-50 μm wide. As the width of the pores does not meet the requirement for bone replacement applications, further study is required to determine the optimal processing conditions. The effect of the applied cooling rate on the size of the pores could not be properly investigated due to the influence of particle size. It is proposed that a particle size of about 100 nm should be employed in order to avoid encapsulation of the powder particles during freezing.

The piezoelectric properties of the freeze cast structures reflected the different microstructures of the samples. Samples that experienced particle encapsulation during freezing presumably contained more defects. This resulted in less complete poling of the ceramic matrix, and, consequently, a reduced piezoelectric response. The samples that displayed the lamellar porous structure of interest were, on the other hand, more sufficiently poled, and displayed piezoelectric coefficients of up to 77% of the dense value, for a porosity of 36%. This study showed that lamellar porous BCZT structures processed by freeze casting could be poled by

the application of a high electric field, without the occurrence of dielectric breakdown, to exhibit a piezoelectric response.

This study demonstrates the potential of freeze casting as a method to producing porous piezoelectric ceramics for biomedical applications. It is the intention that this work can serve as a starting point for further optimization of the slurry composition and freezing parameters.

Chapter 7

Further work

A stable slurry for freeze casting was achieved in this work, however, further study on the stabilization mechanism of ammonium polymethacrylate is required. As a simple test to determine if depletion stabilization is a possible mechanism, the powder should be re-dispersed after the addition of Darvan C-N. In this way, any potential excess dispersant would be removed before the formation of the freeze casting slurry. Freeze casting should thereafter be conducted to check if there is any change in the resulting structure. A better understanding of the adsorption of polymethacrylate on the surface of BCZT particles would be achieved by analyzing the residual concentration of dispersant, after coating of the powder particles. The effect of pH on stabilization of the slurry should also be tested. Furthermore, it is suggested that UV-Vis spectroscopy be performed to determine the sedimentation rate of the slurries. This should give a more accurate representation of the sedimentation behaviour of the system than what was achieved in this study. Measurements could be taken both with and without PVA, to provide more information on the potential interaction between polymethacrylate and PVA, and its destabilizing effect.

Due to the large influence of particle size on the formation of the freeze cast structure, it would be beneficial to systematically investigate the effect of particle size. A range of particle sizes should be trialed, in order to determine the critical size for encapsulation of the particles by the ice front during freezing. As the effect of freezing rate could not be concluded in this work, different freezing rates should be tested, employing an appropriate particle size, where encapsulation does not occur. This would provide a greater overview of the range of pore sizes that could be achieved with the freeze casting method.

Bibliography

[1] L. L. Hench, "Bioceramics," *Journal of the American Ceramic Society*, vol. 81, no. 7, pp. 1705–1728, 1998.

[2] L. L. Hench, "Biomaterials: a forecast for the future," *Biomaterials*, vol. 19, no. 16, pp. 1419–1423, 1998.

[3] L. Polo-Corrales, M. Latorre-Esteves, and J. E. Ramirez-Vick, "Scaffold Design for Bone Regeneration," *Journal of Nanoscience and Nanotechnology*, vol. 14, no. 1, pp. 15–56, 2014.

[4] M. Sundfeldt, L. V Carlsson, C. B Johansson, P. Thomsen, and C. Gretzer, "Aseptic loosening, not only a question of wear: A review of different theories," *Acta Orthopaedica*, vol. 77, no. 2, pp. 177–197, 2006.

[5] J. M. Anderson, "Biological Responses to Materials," *Annual Review of Materials Research*, vol. 31, no. 1, pp. 81–110, 2001.

[6] A. H. Rajabi, M. Jaffe, and T. L. Arinzeh, "Piezoelectric materials for tissue regeneration: A review," *Acta Biomaterialia*, vol. 24, pp. 12–23, 2015.

[7] H. Jaffe, "Piezoelectric Ceramics," *Journal of the American Ceramic Society*, vol. 41, no. 11, pp. 494–498, 1958.

[8] Y. Zhang, L. Chen, J. Zeng, K. Zhou, and D. Zhang, "Aligned porous barium titanate/hydroxyapatite composites with high piezoelectric coefficients for bone tissue engineering," *Materials Science & Engineering C*, vol. 39, no. 1, pp. 143–149, 2014.

[9] F. Jianqing, Y. Huipin, and Z. Xingdong, "Promotion of osteogenesis by a piezoelectric biological ceramic," *Biomaterials*, vol. 18, no. 23, pp. 1531–1534, 1997.

[10] W. Liu and X. Ren, "Large piezoelectric effect in Pb-free ceramics," *Physical Review Letters*, vol. 103, no. 25, p. 257602, 2009.

[11] K. K. Poon, M. C. Wurm, D. M. Evans, M.-A. Einarsrud, R. Lutz, and J. Glaum, "Biocompatibility of (Ba,Ca)(Zr,Ti)O3 piezoelectric ceramics for bone replacement materials," *Journal of Biomedical Materials Research Part B: Applied Biomaterials*, pp. 1–9, 2019.

[12] Y. Oshida, "Requirements for Successful Implant Systems," in *Surface Engineering and Technology for Biomedical Implants*, ch. 4, p. 95, New York, New York: Momentum Press, 2014.

[13] N. Scarisoreanu, F. Craciun, V. Ion, R. Birjega, A. Bercea, V. Dinca, M. Dinescu, L. Sima, M. Icriverz, A. Roseanu, L. Gruionu, and G. Graionu, "Lead-Free Piezoelectric (Ba,Ca)(Zr,Ti)O3 Thin Films for Biocompatible and Flexible Devices," *Acs Applied Materials & Interfaces*, vol. 9, no. 1, pp. 266–278, 2017.

[14] N. Pisitpipathsin, P. Kantha, S. Eitsayeam, G. Rujijanakul, R. Guo, A. S. Bhalla, and K. Pengpat, "Effect of BCZT on Electrical Properties and Bioactivity of 45S5 Bioglass," *Integrated Ferroelectrics*, vol. 142, no. 1, pp. 144–153, 2013.

[15] R. Brånemark, L. Emanuelsson, A. Palmquist, and P. Thomsen, "Bone response to laser-induced micro- and nano-size titanium surface features," *Nanomedicine: Nanotechnology, Biology, and Medicine*, vol. 7, no. 2, pp. 220–227, 2011.

[16] A. R. Studart, U. T. Gonzenbach, E. Tervoort, and L. J. Gauckler, "Processing Routes to Macroporous Ceramics: A Review," *Journal of the American Ceramic Society*, vol. 89, no. 6, pp. 1771–1789, 2006.

[17] S. Deville, E. Saiz, R. K. Nalla, and A. P. Tomsia, "Freezing as a path to build complex composites," *Science*, vol. 311, no. 5760, pp. 515–518, 2006.

[18] S. Deville, "Freeze-Casting of Porous Biomaterials: Structure, Properties and Opportunities," *Materials*, vol. 3, no. 3, pp. 1913–1927, 2010.

[19] S. Deville, E. Saiz, and A. P. Tomsia, "Freeze casting of hydroxyapatite scaffolds for bone tissue engineering," *Biomaterials*, vol. 27, no. 32, pp. 5480–5489, 2006.

[20] J. I. Roscow, Y. Zhang, M. J. Kraśny, R. W. C. Lewis, J. Taylor, and C. R. Bowen, "Freeze cast porous barium titanate for enhanced piezoelectric energy harvesting," *Journal of Physics D: Applied Physics*, vol. 51, no. 22, p. 225301, 2018.

[21] Y. Zhang, J. Roscow, R. Lewis, H. Khanbareh, V. Y. Topolov, M. Xie, and C. R. Bowen, "Understanding the effect of porosity on the polarisation-field response of ferroelectric materials," *Acta Materialia*, vol. 154, pp. 100–112, 2018.

[22] R. J. D. Tilley, "Insulating solids," in *Understanding Solids: The Science of Materials*, ch. 11, pp. 333–344, Chichester: John Wiley & Sons, 2nd ed., 2013.

[23] A. L. Kholkin, N. A. Pertsev, and A. V. Goltsev, "Piezoelectricity and Crystal Symmetry," in *Piezoelectric and Acoustic Materials for Transducer Applications*, ch. 2, pp. 17–38, Boston, MA: Springer US, 2008.

[24] F. R. Baxter, C. R. Bowen, I. G. Turner, and A. C. E. Dent, "Electrically Active Bioceramics: A Review of Interfacial Responses," *Annals of Biomedical Engineering*, vol. 38, no. 6, pp. 2079–2092, 2010.

[25] A. R. West, "Electrical properties," in *Solid State Chemistry and its Applications*, ch. 8, p. 438, Chichester: John Wiley & Sons, 2nd ed., 2014.

[26] L. Jin, F. Li, and S. Zhang, "Decoding the Fingerprint of Ferroelectric Loops: Comprehension of the Material Properties and Structures," *Journal of the American Ceramic Society*, vol. 97, no. 1, pp. 1–27, 2014.

[27] R. A. Dorey, "Microstructure–property relationships How the microstructure of the film affects its properties," in *Ceramic Thick Films for MEMS and Microdevices*, p. 105, Waltham, MA: William Andrew ; Elsevier Science, 2012.

[28] E. W. Yap, J. Glaum, J. Oddershede, and J. E. Daniels, "Effect of porosity on the ferroelectric and piezoelectric properties of (Ba0.85Ca0.15)(Zr0.1Ti0.9)O3 piezoelectric ceramics," *Scripta Materialia*, vol. 145, pp. 122–125, 2018.

[29] R. Gerson and T. C. Marshall, "Dielectric Breakdown of Porous Ceramics," *Journal of Applied Physics*, vol. 30, no. 11, pp. 1650–1653, 1959.

[30] T. Zeng, Q. Lou, Y. Bai, X. Dong, and Y. Wang, "The Dielectric Breakdown Properties of Porous PZT95/5 Ferroelectric Ceramics," *Ferroelectrics*, vol. 478, no. 1, pp. 118–126, 2015.

[31] T. Hang, J. Glaum, Y. A. Genenko, T. Phung, and M. Hoffman, "Investigation of partial discharge in piezoelectric ceramics," *Acta Materialia*, vol. 102, pp. 284–291, 2016.

[32] T. Zeng, X. Dong, C. Mao, Z. Zhou, and H. Yang, "Effects of pore shape and porosity on the properties of porous PZT 95/5 ceramics," *Journal of the European Ceramic Society*, vol. 27, no. 4, pp. 2025–2029, 2007.

[33] Y. Zhang, M. Xie, J. Roscow, and C. Bowen, "Dielectric and piezoelectric properties of porous lead-free 0.5Ba(Ca0.8Zr0.2)O3-0.5(Ba0.7Ca 0.3)TiO3 ceramics," *Materials Research Bulletin*, vol. 112, pp. 426–431, 2019.

[34] R. Khachaturyan, S. Zhukov, J. Schultheiß, C. Galassi, C. Reimuth, J. Koruza, H. von Seggern, and Y. A. Genenko, "Polarization-switching dynamics in bulk ferroelectrics with isometric and oriented anisometric pores," *Journal of Physics D: Applied Physics*, vol. 50, no. 4, p. 045303, 2017.

[35] H. L. Zhang, J.-F. Li, and B.-P. Zhang, "Microstructure and electrical properties of porous PZT ceramics derived from different pore-forming agents," *Acta Materialia*, vol. 55, no. 1, pp. 171–181, 2007.

[36] V. A. Lukacs, R. Stanculescu, L. Curecheriu, C. E. Ciomaga, N. Horchidan, C. Cioclea, and L. Mitoseriu, "Structural and functional properties of BaTiO3 porous ceramics produced by using pollen as sacrificial template," *Ceramics International*, vol. 46, no. 1, pp. 523–530, 2020.

[37] J. Schultheiß, J. I. Roscow, and J. Koruza, "Orienting anisometric pores in ferroelectrics: Piezoelectric property engineering through local electric field distributions," *Physical Review Materials*, vol. 3, no. 8, p. 084408, 2019.

[38] S. Deville, "The lure of ice-templating: Recent trends and opportunities for porous materials," *Scripta Materialia*, vol. 147, pp. 119–124, 2018.

[39] S. Deville, "Freeze-Casting of Porous Ceramics: A Review of Current Achievements and Issues," *Advanced Engineering Materials*, vol. 10, no. 3, pp. 155–169, 2008.

[40] Y. Zhang, C. R. Bowen, and S. Deville, "Ice-templated poly(vinylidene fluoride) ferroelectrets," *Soft Matter*, vol. 15, no. 5, pp. 825–832, 2019.

[41] F. Li, X. Xue, T. Jia, W. Dang, K. Zhao, and Y. Tang, "Lamellar structure/processing relationships and compressive properties of porous Ti6Al4V alloys fabricated by freeze casting," *Journal of the Mechanical Behavior of Biomedical Materials*, vol. 101, p. 103424, 2020.

[42] J. Wang, W. Zhang, and C. Zhang, "Versatile fabrication of anisotropic and superhydrophobic aerogels for highly selective oil absorption," *Carbon*, vol. 155, pp. 16–24, 2019.

[43] K. L. Scotti and D. C. Dunand, "Freeze casting – A review of processing, microstructure and properties via the open data repository, FreezeCasting.net," *Progress in Materials Science*, vol. 94, pp. 243–305, 2018.

[44] S. Deville, "Ice-Templating: Processing Routes, Architectures, and Microstructures," in *Freezing Colloids: Observations, Principles, Control, and Use: Applications in Materials Science, Life Science, Earth Science, Food Science, and Engineering*, Engineering Materials and Processes, ch. 4, p. 182, Cham: Springer International Publishing, 2017.

[45] S. W. Sofie and F. Dogan, "Freeze Casting of Aqueous Alumina Slurries with Glycerol," *Journal of the American Ceramic Society*, vol. 84, no. 7, pp. 1459–1464, 2001.

[46] R. Liu, T. Xu, and C.-a. Wang, "A review of fabrication strategies and applications of porous ceramics prepared by freeze-casting method," *Ceramics International*, vol. 42, no. 2, pp. 2907–2925, 2016.

[47] S. Deville, S. Meille, and J. Seuba, "A meta-analysis of the mechanical properties of ice-templated ceramics and metals," *Science and Technology of Advanced Materials*, vol. 16, no. 4, pp. 1–15, 2015.

[48] D. S. Kim, C. Baek, H. J. Ma, and D. K. Kim, "Enhanced dielectric permittivity of BaTiO3/epoxy resin composites by particle alignment," *Ceramics International*, vol. 42, no. 6, pp. 7141–7147, 2016.

[49] S. Deville, "Understanding the Freezing of Colloidal Suspensions: Crystal Growth and Particle Redistribution," in *Freezing Colloids: Observations, Principles, Control, and Use: Applications in Materials Science, Life Science, Earth Science, Food Science, and Engineering*, ch. 3, pp. 98, 99, 104, 107, 109, 124, 132, 133, Cham: Springer International Publishing, 2017.

[50] J. Lewis, "Colloidal processing of ceramics," *Journal of the American Ceramic Society*, vol. 83, no. 10, pp. 2341–2359, 2000.

[51] G. Cao and Y. Wang, "Physical Chemistry of Solid Surfaces," in *Nanostructures and nanomaterials: synthesis, properties, and applications*, ch. 2, pp. 39, 54, Singapore: World Scientific, 2nd ed., 2011.

[52] T. F. Tadros, "Origin of charge at interfaces and structure of the electrical double layer," in *Basic Principles of Interface Science and Colloid Stability*, ch. 2, p. 19, Berlin: De Gruyter, 2017.

[53] V. S. Kulkarni, "Emulsions and Microemulsions for Topical and Transdermal Drug Delivery," in *Handbook of non-invasive drug delivery systems*, Personal Care and Cosmetic Technology, ch. 3, p. 66, William Andrew ; Elsevier Science, 2009.

[54] A. Schierz and H. Zänker, "Aqueous suspensions of carbon nanotubes: Surface oxidation, colloidal stability and uranium sorption," *Environmental Pollution*, vol. 157, no. 4, pp. 1088–1094, 2009.

[55] J. Jean and H. Wang, "Dispersion of Aqueous Barium Titanate Suspensions with Ammonium Salt of Poly(methacrylic acid)," *Journal of the American Ceramic Society*, vol. 81, no. 6, pp. 1589–1599, 1998.

[56] S. Deville, "Ice-Templating, Freeze-Casting: A Practical Guide to Get Started," in *Freezing Colloids: Observations, Principles, Control, and Use: Applications in Materials Science, Life Science, Earth Science, Food Science, and Engineering*, ch. 8, pp. 552, 554, 555, 557, 558, 560, 561, 562, 582, Cham: Springer International Publishing, 2017.

[57] S. Deville, "Ice-Templating and Freeze-Casting: Control of the Processes, Microstructures, and Architectures," in *Freezing Colloids: Observations, Principles, Control, and Use: Applications in Materials Science, Life Science, Earth Science, Food Science, and Engineering*, ch. 6, pp. 361, 372, 415, 423, Cham: Springer International Publishing, 2017.

[58] J. S. Reed, "Flocculants, Binders and Bonds," in *Principles of ceramics processing*, ch. 11, p. 176, New York, New York: John Wiley & Sons, Inc., 2nd ed., 1995.

[59] S. Deville, "Ice-Templated Materials: Polymers, Ceramics, Metals and Their Composites Abstract," in *Freezing Colloids: Observations, Principles, Control, and Use: Applications in Materials Science, Life Science, Earth Science, Food Science, and Engineering*, ch. 5, p. 274, Cham: Springer International Publishing, 2017.

[60] D. W. Richerson, "Shape-Forming Processes," in *Modern ceramic engineering : properties, processing, and use in design*, vol. 29 of *Materials engineering*, ch. 13, p. 423, Boca Raton, Fla: CRC Press, 3rd ed., 2006.

[61] U. G. K. Wegst, M. Schecter, A. E. Donius, and P. M. Hunger, "Biomaterials by freeze casting," *Philosophical Transactions of the Royal Society A*, vol. 368, no. 1917, pp. 2099–2121, 2010.

[62] S. Deville, E. Saiz, and A. P. Tomsia, "Ice-templated porous alumina structures," *Acta Materialia*, vol. 55, no. 6, pp. 1965–1974, 2007.

[63] S. Deville, E. Maire, A. Lasalle, A. Bogner, C. Gauthier, J. Leloup, and C. Guizard, "In Situ X-Ray Radiography and Tomography Observations of the Solidification of Aqueous Alumina Particle Suspensions—Part I: Initial Instants," *Journal of the American Ceramic Society*, vol. 92, no. 11, pp. 2489–2496, 2009.

[64] R. J. D. Tilley, "Phase diagrams," in *Understanding Solids: The Science of Materials*, ch. 4, p. 78, Chichester: John Wiley & Sons, 2nd ed., 2013.

[65] D. W. Richerson, "Densification," in *Modern ceramic engineering : properties, processing, and use in design*, ch. 14, pp. 477–479, Boca Raton, Fla: CRC Press, 3rd ed., 2006.

[66] S. Farhangdoust, A. Zamanian, M. Yasaei, and M. Khorami, "The effect of processing parameters and solid concentration on the mechanical and microstructural properties of freeze-casted macroporous hydroxyapatite scaffolds," *Materials Science & Engineering C*, vol. 33, no. 1, pp. 453–460, 2013.

[67] S. Sadeghpour, A. Amirjani, M. Hafezi, and A. Zamanian, "Fabrication of a novel nanostructured calcium zirconium silicate scaffolds prepared by a freeze-casting method for bone tissue engineering," *Ceramics International*, vol. 40, no. 10, pp. 16107–16114, 2014.

[68] J. H. Kim, J. H. Lee, T. Y. Yang, S. Y. Yoon, B. K. Kim, and H. C. Park, "TBA-based freeze/gel casting of porous hydroxyapatite scaffolds," *Ceramics International*, vol. 37, no. 7, pp. 2317–2322, 2011.

[69] S. Deville, E. Maire, A. Lasalle, A. Bogner, C. Gauthier, J. Leloup, and C. Guizard, "Influence of Particle Size on Ice Nucleation and Growth During the Ice-Templating Process," *Journal of the American Ceramic Society*, vol. 93, no. 9, pp. 2507–2510, 2010.

[70] Y. Zhang, K. Zhou, Y. Bao, and D. Zhang, "Effects of rheological properties on ice-templated porous hydroxyapatite ceramics," *Materials Science & Engineering C*, vol. 33, no. 1, pp. 340–346, 2013.

[71] S. Deville, E. Maire, G. Bernard-Granger, A. Lasalle, A. Bogner, C. Gauthier, J. Leloup, and C. Guizard, "Metastable and unstable cellular solidification of colloidal suspensions," *Nature Materials*, vol. 8, no. 12, pp. 966–972, 2009.

[72] C. Peko, B. Groth, and I. Nettleship, "The Effect of Polyvinyl Alcohol on the Microstructure and Permeability of Freeze-Cast Alumina," *Journal of the American Ceramic Society*, vol. 93, no. 1, pp. 115–120, 2010.

[73] Q. Fu, M. N. Rahaman, B. S. Bal, and R. F. Brown, "In vitro cellular response to hydroxyapatite scaffolds with oriented pore architectures," *Materials Science & Engineering C*, vol. 29, no. 7, pp. 2147–2153, 2009.

[74] S. Deville, "Properties and Applications of Ice-Templated Materials," in *Freezing Colloids: Observations, Principles, Control, and Use: Applications in Materials Science, Life Science, Earth Science, Food Science, and Engineering*, ch. 7, p. 468, Cham: Springer International Publishing, 2017.

[75] M. Acosta, N. Novak, V. Rojas, S. Patel, R. Vaish, J. Koruza, G. A. Rossetti Jr, and J. Rödel, "BaTiO3-based piezoelectrics: Fundamentals, current status, and perspectives," *Applied Physics Reviews*, vol. 4, p. 041305, 2017.

[76] Y. Zhang, J. Glaum, C. Groh, M. C. Ehmke, J. E. Blendell, K. J. Bowman, M. J. Hoffman, and S. Trolier-McKins, "Correlation Between Piezoelectric Properties and Phase Coexistence in (Ba,Ca)(Ti,Zr)O3 Ceramics," *Journal of the American Ceramic Society*, vol. 97, no. 9, pp. 2885–2891, 2014.

[77] D. Keeble, F. Benabdallah, P. A. Thomas, M. Maglione, and J. Kreisel, "Revised structural phase diagram of (Ba0.7Ca0.3TiO3)-(BaZr0.2Ti0.8O3)," *Applied Physics Letters*, vol. 102, no. 092903, pp. 1–5, 2013.

[78] M. Ehmke, S. Ehrlich, J. Blendell, and K. J. Bowman, "Phase coexistence and ferroelastic texture in high strain(1-x)Ba(Zr0.2Ti0.8)O3–x(Ba0.7Ca0.3)TiO3 piezoceramics," *Journal of Applied Physics*, vol. 111, no. 124110, pp. 1–7, 2012.

[79] Y. Tian, L. Wei, X. Chao, Z. Liu, and Z. Yang, "Phase Transition Behavior and Large Piezoelectricity Near the Morphotropic Phase Boundary of Lead-free (Ba0.85Ca0.15)(Zr0.1Ti0.9)O3 Ceramics," *Journal of the American Ceramic Society*, vol. 96, no. 2, pp. 496–502, 2013.

[80] C. Zhou, X. Ke, Y. Yao, S. Yang, Y. Ji, W. Liu, Y. Yang, L. X. Zhang, Y. Hao, S. Ren, L. Zhang, and X. Ren, "Evolution from successive phase transitions to "morphotropic phase boundary" in BaTiO3-based ferroelectrics," *Applied Physics Letters*, vol. 112, no. 182903, 2018.

[81] K. S. Fedje, "Study of Piezoelectric and Mechanical Properties of Porous Barium Titanate Ceramics for Biomedical Applications (Masters Thesis)," tech. rep., Norwegian University of Science and Technology, 2017.

[82] P. H. Bigg, "Density of water in SI units over the range 0-40°C," *British Journal of Applied Physics*, vol. 18, no. 11, pp. 521–525, 1967.

[83] S. W. Sofie, "Fabrication of Functionally Graded and Aligned Porosity in Thin Ceramic Substrates With the Novel Freeze–Tape-Casting Process," *Journal of the American Ceramic Society*, vol. 90, no. 7, pp. 2024–2031, 2007.

[84] A. Kaushal, S. Olhero, and J. Ferreira, "Lead-free 0.5Ba(Zr0.2Ti0.8)O3 - 0.5(Ba0.7Ca0.3)TiO3 powder surface treated against hydrolysis - a key for a successful aqueous processing," *Journal of materials chemistry C*, vol. 1, pp. 4846–4853, 2013.

[85] N. Iwata and T. Mori, "Effect of binder addition on optimum additive amount of dispersant for aqueous BaTiO3 slurry," *Ceramics International*, vol. 45, no. 16, pp. 19644–19649, 2019.

[86] A. W. M. de Laat and G. L. T. van den Heuvel, "Competitive and displacement adsorption of polyvinyl alcohol and the ammonium salt of a polyacrylic acid on BaTiO3," *Colloids and Surfaces A: Physicochemical and Engineering Aspects*, vol. 70, no. 2, pp. 179–187, 1993.

[87] S. M. Miller, X. Xiao, J. A. Setlock, and K. T. Faber, "Freeze-cast alumina pore networks: Effects of processing parameters in steady-state solidification regimes of aqueous slurries," *Journal of the European Ceramic Society*, vol. 38, no. 15, pp. 5134–5143, 2018.

[88] Y. Zhang, M. Xie, J. Roscow, Y. Bao, K. Zhou, D. Zhang, and C. Bowen, "Enhanced pyroelectric and piezoelectric properties of PZT with aligned porosity for energy harvesting applications," *arXiv.org*, vol. 5, no. 14, 2019.

Appendix A

X-ray diffractograms

To check for the phase purity of the calcined powders, x-ray diffraction was utilized. Figure A.0.1 shows the resulting XRD patterns for all the calcined powder batches. The peaks are fitted to the BCZT composition with 10 mol% calcium and 10 mol% zirconium, marked with black squares, showing that all powder batches were phase pure. The small peak at a 2Θ of around 28°, marked with an asterisk, is the contribution from Cu Kβ1 radiation from the XRD measurement.
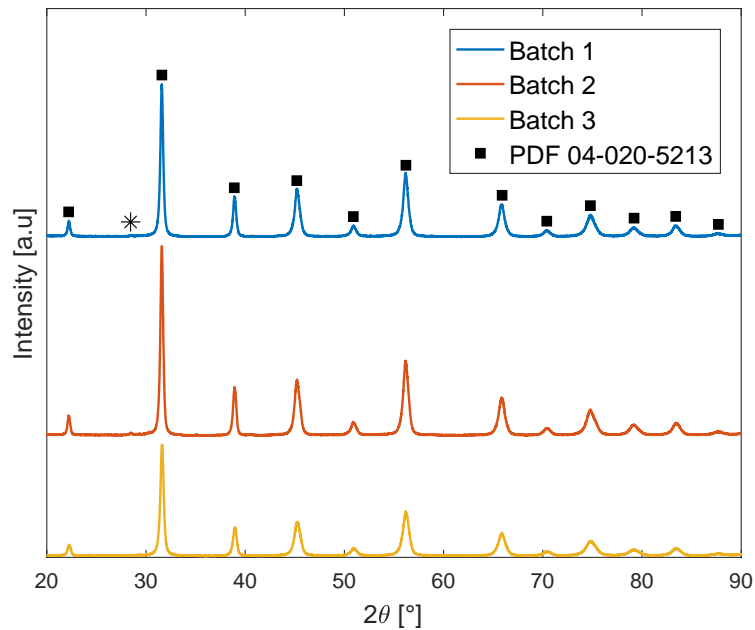
Figure A.0.1: The XRD patterns for all the calcined powder batches, matched to the PDF card 04-020-5213 with the Diffrac.EVA V5.1 software. The asterisk marks background noise from the XRD measurements.

Appendix B

Particle size measurements

Laser scattering particle size analysis was used to measure the particle size distributions of the calcined BCZT powders. Figure B.0.1 demonstrates that all batches achieved a unimodal size distribution, as intended, although the median size of Batch 3 was higher than that of Batch 1 and 2.
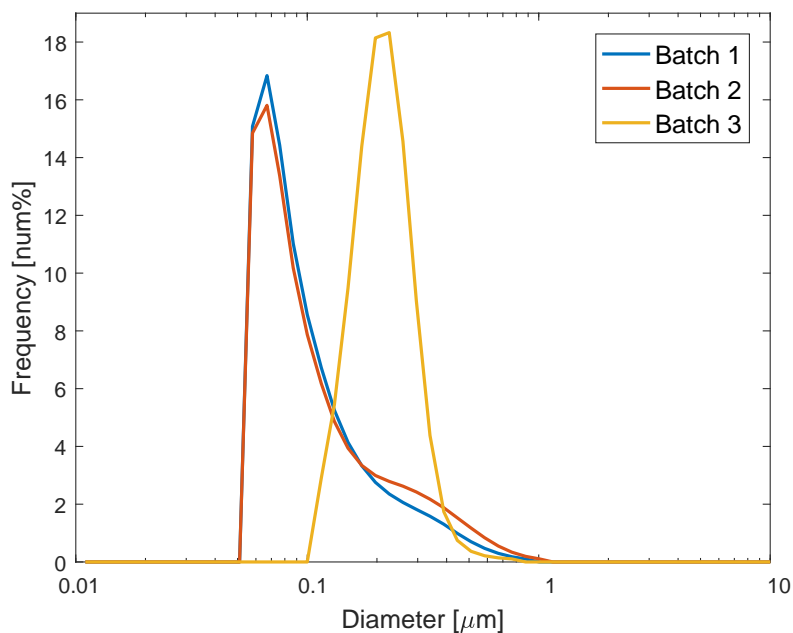
Figure B.0.1: The particle size distributions for the three batches of calcined BCZT powder, all displaying a unimodal size distribution, but with different median particle sizes.

The calcined powders were also analyzed with a SEM, which confirmed the particle size of below approximately 1 μm, as indicated by the images in Figure B.0.2.
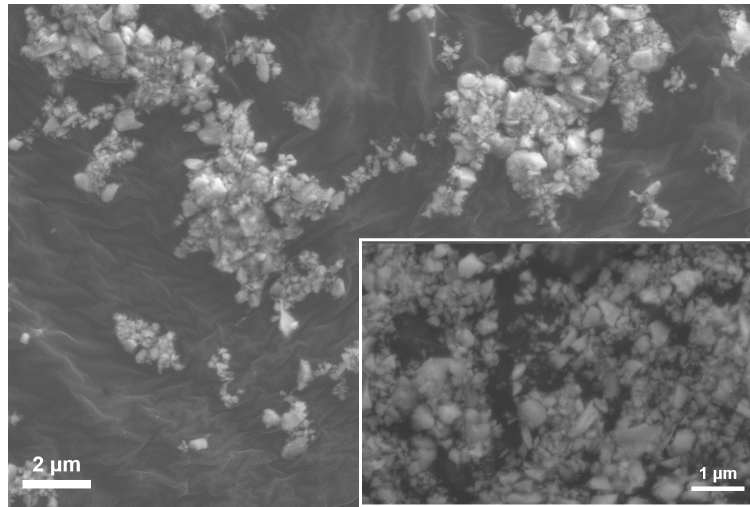
(a) Batch 1
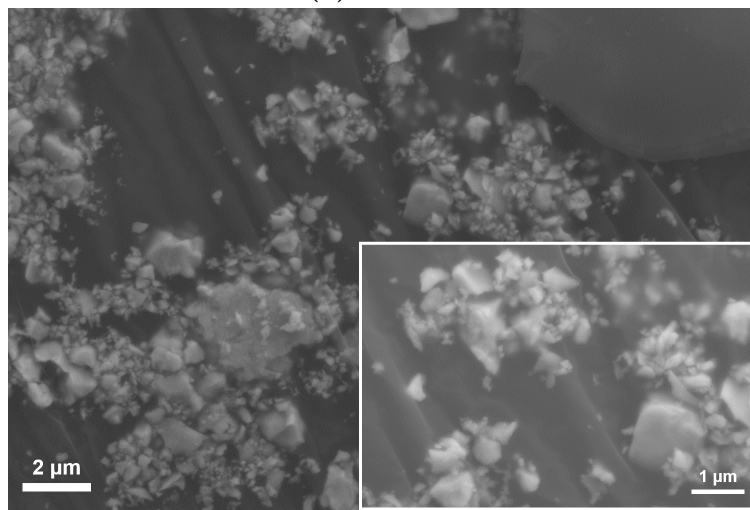
(b) Batch 2
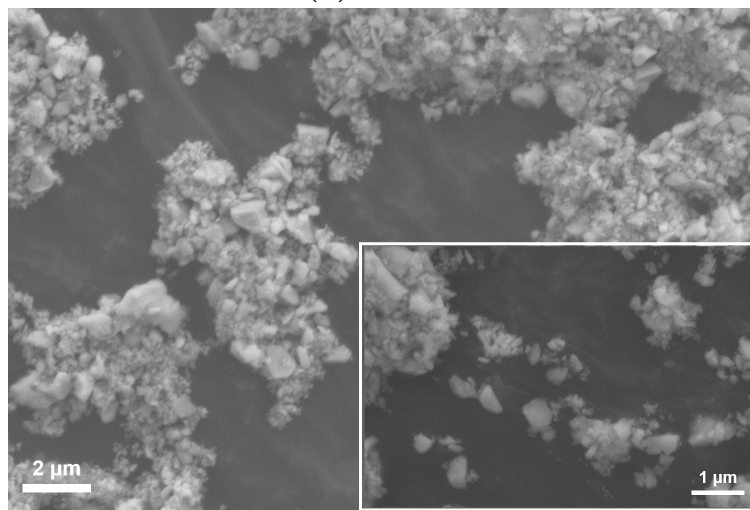
(c) Batch 3

Figure B.0.2: SEM images of the calcined powders from Batches 1-3.

Appendix C

Density measurements

The densities of the calcined powders was measured using a gas pycnometer. The data was used to determine the mass of powder needed to achieve the desired vol% solid load in the slurries for freeze casting. Table C.0.1 shows the calculated density value for each powder batch.

Table C.0.1: The powder density for all the calcined BCZT batches.

Powder batch	Density [g/cm^3]
1	5.497±0.006
2	5.463±0.005
3	5.293±0.006

The bulk density and porosity of the samples used for piezoelectric characterization were determined by Archimedes method. The bulk density, total porosity, open porosity and closed porosity were calculated according to Equations C.1, C.2, C.3, C.4, respectively,

$$\rho_b = \frac{m_1}{m_3 - m_2}\rho_{liq} \tag{C.1}$$

$$\pi_t = \frac{\rho_t - \rho_b}{\rho_t} * 100 \tag{C.2}$$

$$\pi_a = \frac{m_3 - m_1}{m_3 - m_2} * 100 \tag{C.3}$$

$$\pi_f = \pi_t - \pi_a \tag{C.4}$$

where ρ_b is the bulk density, ρ_{liq} is the density of the immersion liquid (isoproponal in this study), ρ_t is the theoretical density of the material, π_t is the total porosity, π_a is the apparent

or open porosity, π_f is the closed porosity, m_1 is the dry mass, m_2 is the suspended wet mass and m_3 is the wet mass in air.

Appendix D

Microstructure

D.1 Slurry optimization

Figure D.1.1 shows a SEM image of the sample made with 20 vol% powder, 1.5 wt% Darvan C-N and 1 wt% PVA, labelled as freeze casting #3 in Table **??**. Some relatively large pores are visible in Figure D.1.1, which may indicate that the degassing step was not sufficient to remove the bubbles introduced during mixing of the slurry.
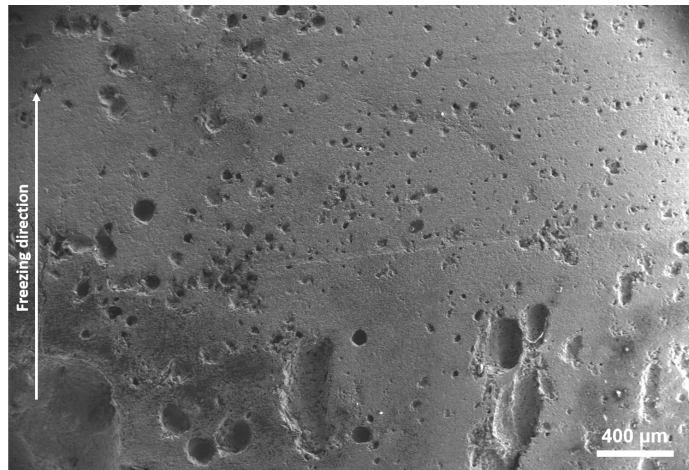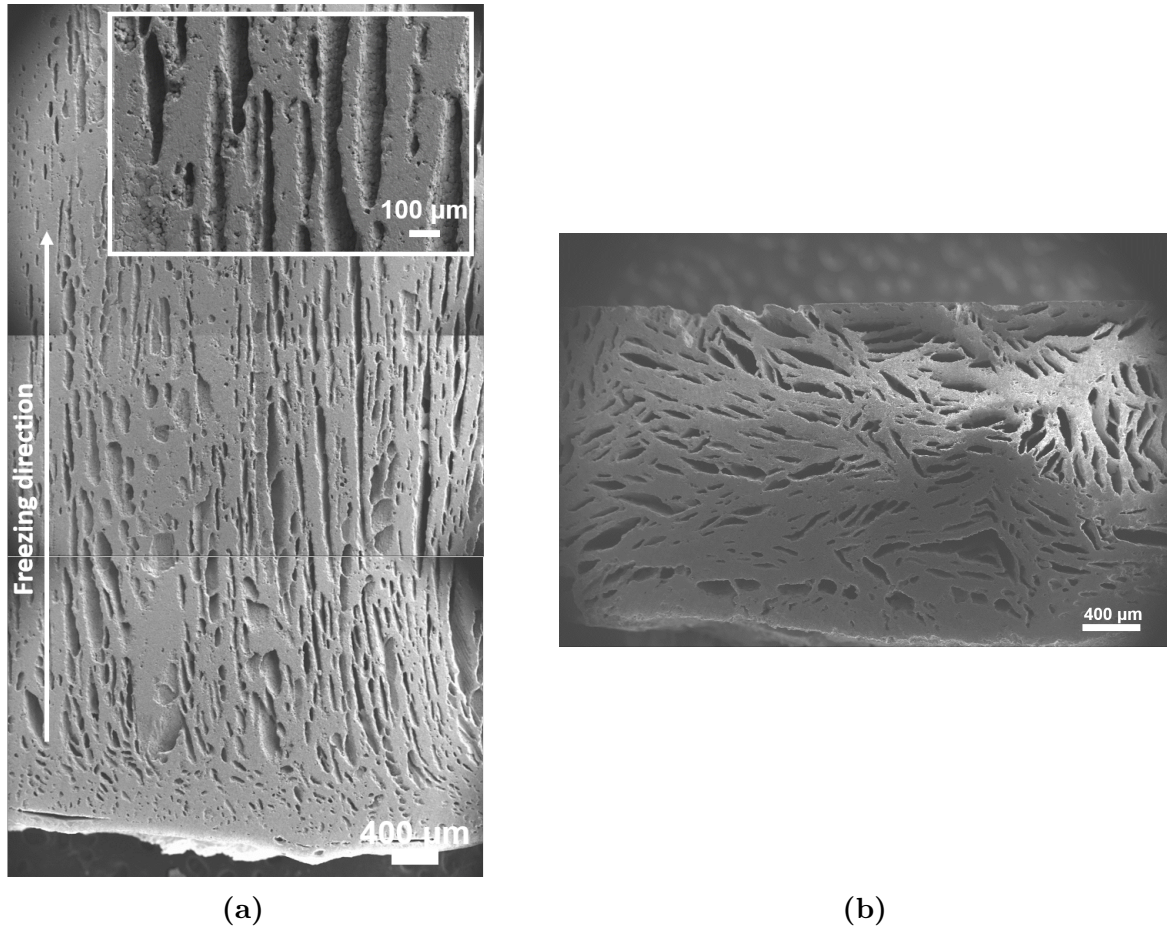

Figure D.1.1: SEM image of the freeze cast sample made with 20 vol% BCZT powder, 15 wt% Darvan C-N and 1 wt% PVA, taken perpendicular to the freezing direction.

Figure D.1.2 shows SEM images of the different microstructural zones obtained for the sample made with 15 vol% powder, 3 wt% Darvan C-N and 1 wt% PVA (freeze casting #4 in Table **??**). Figure D.1.2a shows the dense region and region with irregular pores, found at the bottom of the sample. The lamellar microstructure at the top of the sample is given in Figure D.1.2b, with an insert showing the lamella at higher magnification.

(a)   (b)
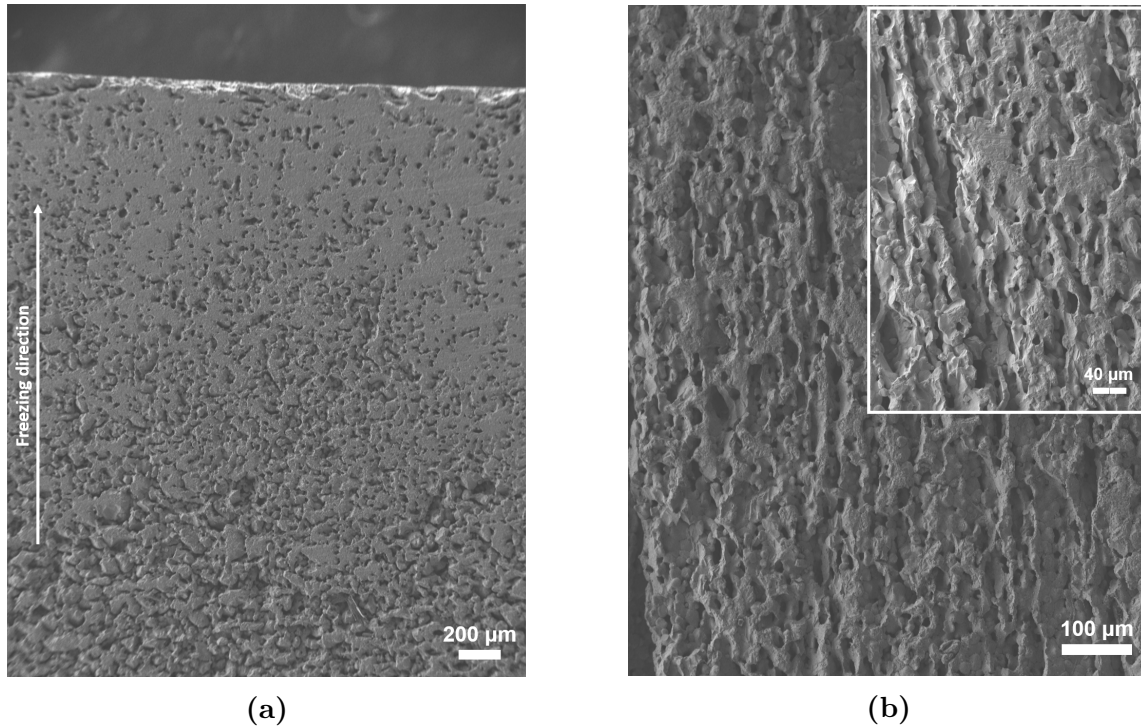
Figure D.1.2: SEM images of the different microstructures achieved for the freeze cast structure made with 15 vol% powder, 3 wt% Darvan C-N and 1 wt% PVA, taken perpendicular to the freezing direction. (a) The dense and irregular porous region, located at the bottom of the sample. (b) The lamellar porous zone found at the top of the sample. The insert shows the lamella at higher magnification.

Figure D.1.3 shows the first freeze cast samples made with 15 vol% powder, 5 wt% Darvan C-N and 1 wt% PVA (freeze casting #5 in Table **??**). Due to partial melting of the water before the sample was put in the freeze dryer, the sample did not display a representative microstructure. Figure D.1.3a shows the cross section of the sample, taken perpendicular to the freezing direction, with an insert containing a close-up view of the pores. Figure D.1.3b shows the top surface of the structure, taken parallel to the freezing direction.

Figure D.1.3: SEM images of the freeze cast sample made with 15 vol% powder, 5 wt% Darvan C-N and 1 wt% PVA. (a) Cross section taken perpendicular to the freezing direction, with an insert showing the pores at higher magnification. (b) Top surface of the samples taken parallel to the freezing direction.

D.2 Grain size

A SEM micrograph of the grain microstructure in a dense sample is shown in Figure D.2.1. The grain size was 30-40 μm. Corresponding images for the freeze cast samples made with the optimized slurry composition are given in Figures D.2.2-D.2.4. The grain size in the transition region was about 30-50 μm, while grains in the aligned porous regions were approximately 10-30 μm. The grain size is slightly larger in the transition region, as the diffusion distance for the grains is smaller than in the lamellar region. The grain size was only analyzed in the porous region of the sample frozen at 10 °C/min and made with powder from Batch 3, as it was difficult to distinguish where the transition region ended.
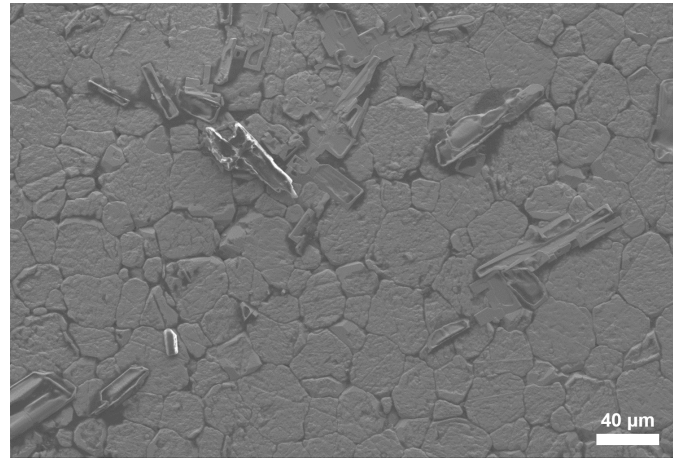
Figure D.2.1: SEM micrograph of the grain microstructure in a dense sample.

(a)

(b)

(c)

(d)
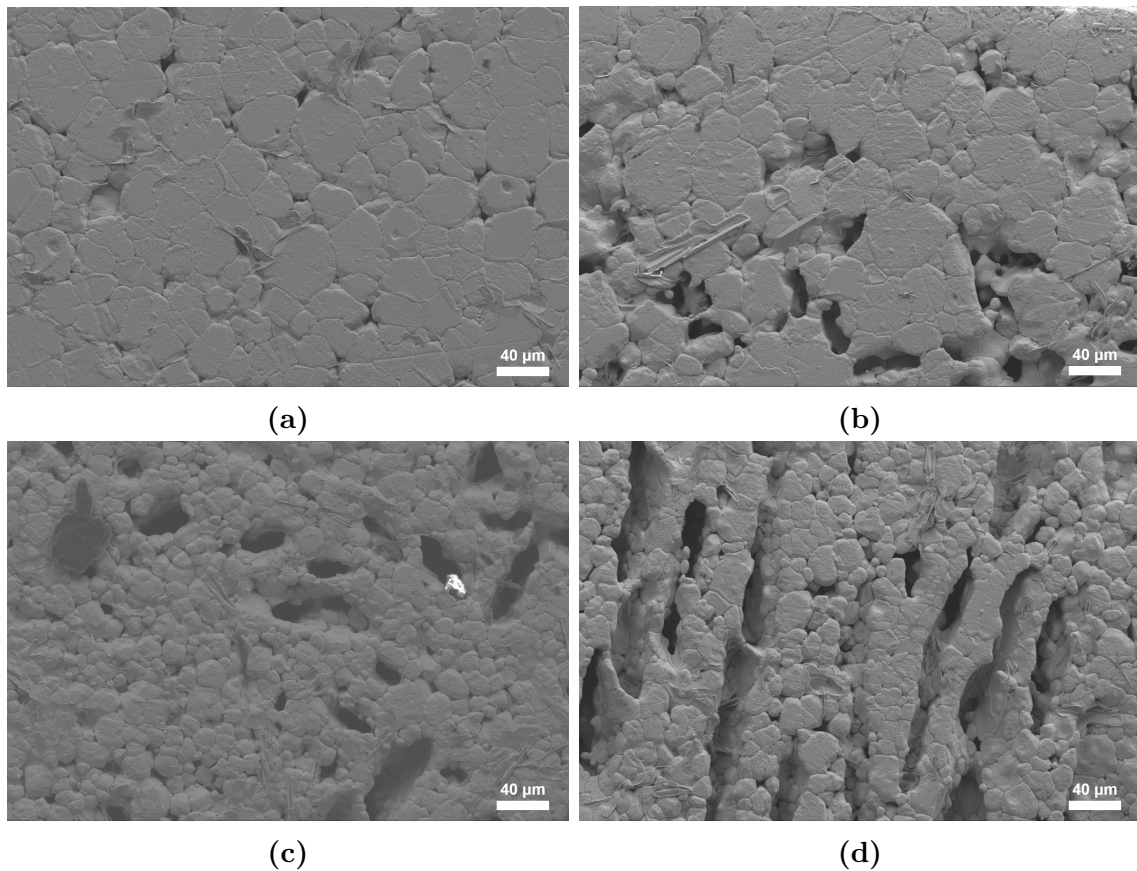
Figure D.2.2: SEM micrographs displaying the grain structure in the freeze cast sample made with Batch 3 powder and cooled at 5 °C/min. Images are taken parallel (a,c) and perpendicular (b,d) to the freezing direction, and show grains in the transition- (a,b) and aligned porous (c,d) region.
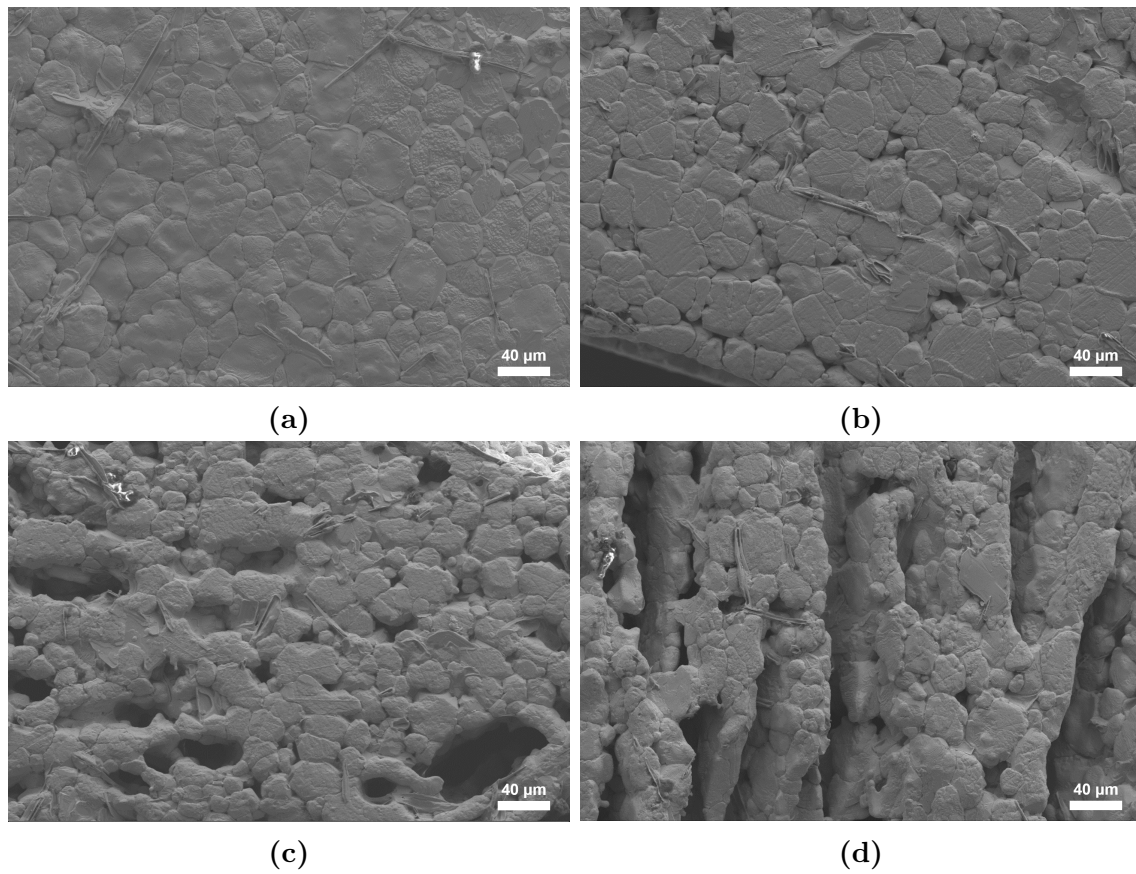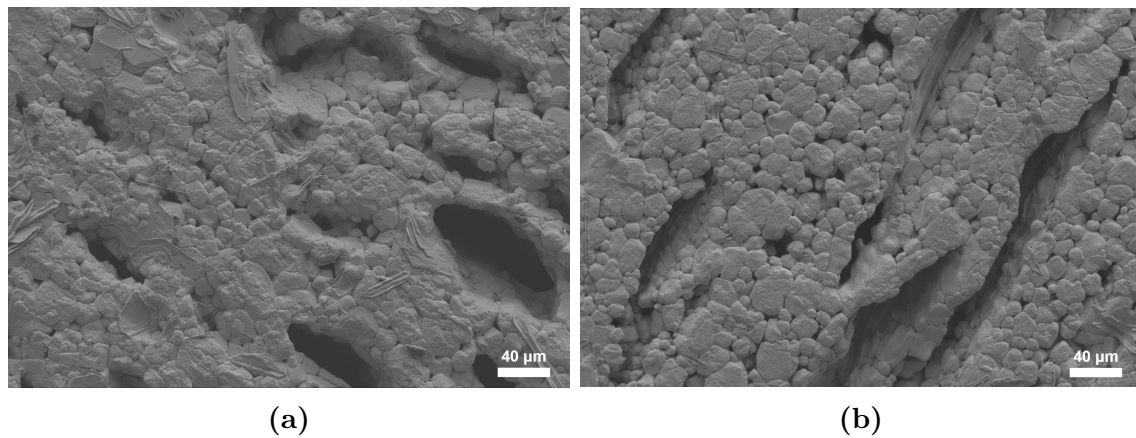
Figure D.2.3: SEM micrographs displaying the grain structure in the freeze cast sample made with Batch 3 powder and cooled at 1 °C/min. Images are taken parallel (a,c) and perpendicular (b,d) to the freezing direction, and show grains in the transition- (a,b) and lamellar (c,d) region.

Figure D.2.4: SEM micrographs displaying the grain structure in the freeze cast sample made with Batch 3 powder and cooled at 10 °C/min. Images are taken parallel (a) and perpendicular (b) to the freezing direction, and show grains in the aligned porous region of the sample.

Appendix E

Piezoelectric measurements

The polarization, strain and current hysteresis loops for all the measured samples are shown in Figures E.0.1, E.0.2 and E.0.3, respectively. The slightly rounded polarization and current loops for Sample 3, frozen with a cooling rate of 10 °C/min (Figures E.0.1e and E.0.3e) indicates a leakage current. The strain loop for Sample 1, cooled at 5 °C/min and made with Batch 3 powder, indicates that the resolution in the measurement perhaps should have been higher. Only one current hysteresis loop is shown for the dense samples, in Figure E.0.3a, as the loops were indistinguishable.
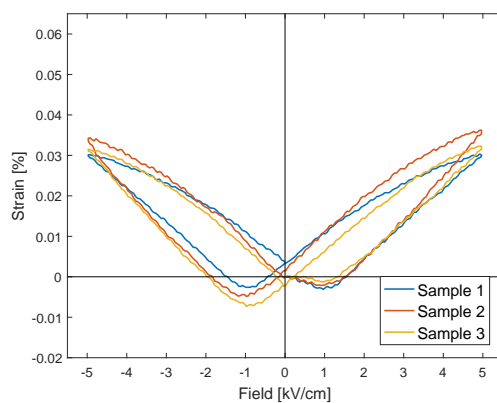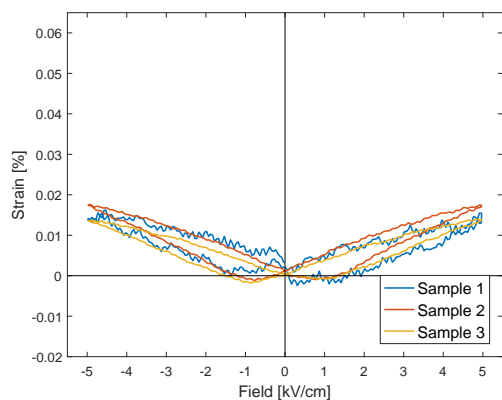
(a) Dense

(b) 5 °C/min, Batch 2

(c) 5 °C/min, Batch 3

(d) 1 °C/min, Batch 3
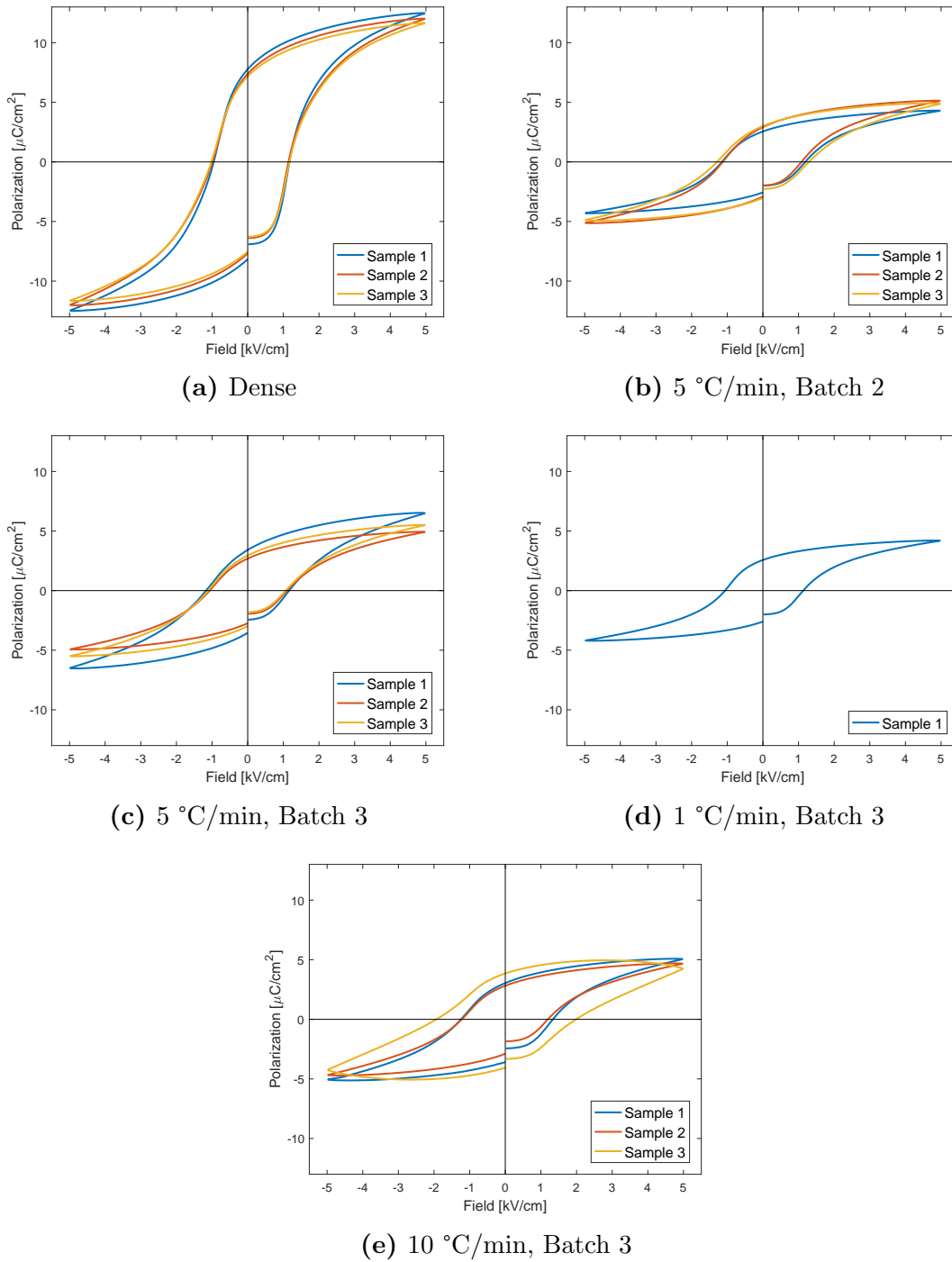
(e) 10 °C/min, Batch 3

Figure E.0.1: The polarization hysteresis loops for all the measured samples. The applied cooling rate and powder batch for each freeze cast sample is indicated.
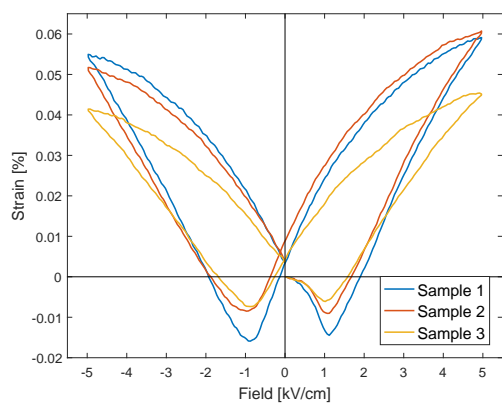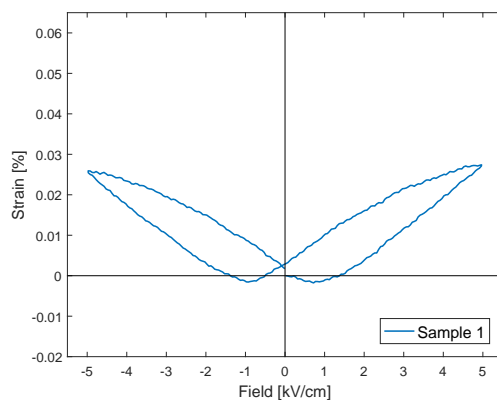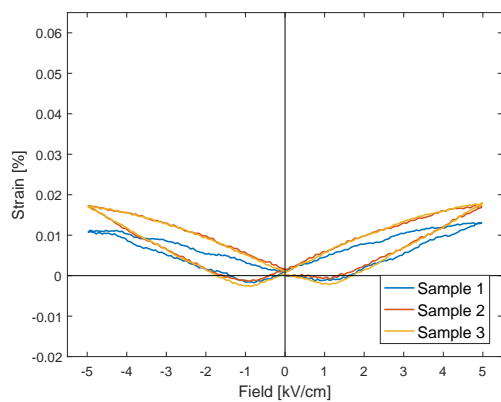
(a) Dense

(b) 5 °C/min, Batch 2

(c) 5 °C/min, Batch 3

(d) 1 °C/min, Batch 3

(e) 10 °C/min, Batch 3

Figure E.0.2: The strain hysteresis loops for all the measured samples. The applied cooling rate and powder batch for each freeze cast sample is indicated.

(a) Dense

(b) 5 °C/min, Batch 2

(c) 5 °C/min, Batch 3

(d) 1 °C/min, Batch 3

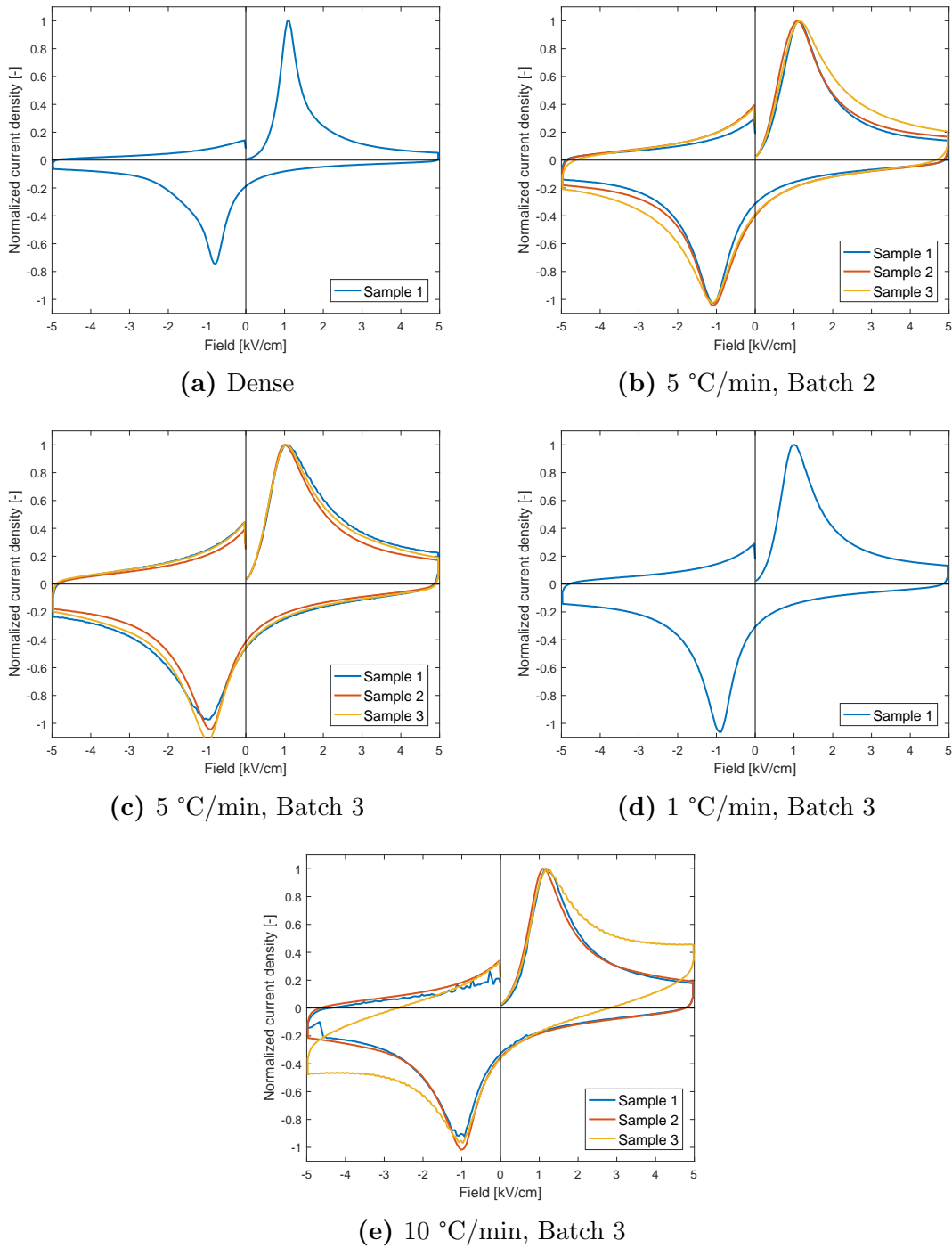**(e)** 10 °C/min, Batch 3

Figure E.0.3: The current hysteresis loops for all the measured samples. The applied cooling rate and powder batch for each freeze cast sample is indicated.